

UNCLASSIFIED

AD NUMBER

AD803212

LIMITATION CHANGES

TO:

Approved for public release; distribution is unlimited. Document partially illegible.

FROM:

Distribution authorized to U.S. Gov't. agencies and their contractors;
Administrative/Operational Use; AUG 1966. Other requests shall be referred to Air Force Rome Air Development Center, Griffiss AFB, NY.
Document partially illegible.

AUTHORITY

radc, usaf ltr, 17 sep

THIS PAGE IS UNCLASSIFIED

Technical Report...

803212

**CONTINUED STUDIES ON ADVANCED FERRIMAGNETIC
MATERIALS APPLIED TO DIGITAL PHASE SHIFTERS**

FIRST SEMIANNUAL REPORT

28 February 1966 to 28 August 1966

ARPA ORDER No. 570 - PROGRAM CODE No. 6E30

RADC Contract No. AF30(602)4122

**Air Force Systems Command
Research and Technology Division
Rome Air Development Center
Griffiss Air Force Base, New York**

**Project Defender
Advanced Research Projects Agency (ARPA)
Department of Defense
Washington, D.C.**

SPERRY

MICROWAVE ELECTRONICS COMPANY

CLEARWATER, FLORIDA

3
23

**BEST
AVAILABLE COPY**

TECHNICAL REPORT

CONTINUED STUDIES ON ADVANCED FERRIMAGNETIC MATERIALS APPLIED TO DIGITAL PHASE SHIFTERS

FIRST SEMIANNUAL REPORT

28 February 1966 to 28 August 1966

ARPA ORDER No. 550 - PROGRAM CODE No. 6E30
RADC CONTRACT No. AF30(602) 4122

Air Force Systems Command
Research and Technology Division
Rome Air Development Center
Griffiss Air Force Base, New York

Project Defender
Advanced Research Projects Agency (ARPA)
Department of Defense
Washington, D.C.

Title of Work:

Continued investigations directed toward the improvement and evaluation of ferrimagnetic materials for use in microwave digital phase shifters at L-, S-, C-, and X-bands.

October 1966

SPERRY MICROWAVE ELECTRONICS COMPANY
DIVISION OF SPERRY RAND CORPORATION
CLEARWATER, FLORIDA

SJ-220-4002-3

Copy No _____

TABLE OF CONTENTS

<u>Section</u>	<u>Page</u>
1 SYNOPSIS	1 - 1
2 INTRODUCTION	2 - 1
2.1 Background of Program	2 - 1
2.2 Program Objectives	2 - 2
3 OPERATING DYNAMICS OF FERRITE DIGITAL PHASE SHIFTERS	3 - 1
3.1 Basic Concept of Ferrite Digital Phase Shifters (FDPS)	3 - 1
3.2 Analytical Models of Ferrite Digital Phase Shifters	3 - 4
3.2.1 Microwave Magnetic Properties of Partially Magnetized Ferrites	3 - 5
3.2.2 High Power Characteristics of Partially Magnetized Ferrites	3 - 18
3.3 Analysis Techniques	3 - 26
3.4 Influence of Intrinsic and Ceramic Properties on Square Loop Characteristics	3 - 33
3.4.1 Remanence Ratio	3 - 33
3.4.2 Coercive Force	3 - 36
3.4.3 Switching Time	3 - 36
4 SUMMARY AND DISCUSSION OF RESULTS	4 - 1
4.1 Introduction	4 - 1
4.2 Measurement Equipment and Techniques	4 - 1
4.2.1 Measurement of Material Properties	4 - 2
4.2.2 Preparation Procedure	4 - 10
4.2.3 Measurement of Device Characteristics	4 - 11
4.3 Materials for Evaluation (Compositions and Reasons for Selection)	4 - 17
4.4 Material Properties	4 - 19

TABLE OF CONTENTS (Cont'd)

<u>Section</u>	<u>Page</u>
4.5 Evaluation of Materials by Analysis and Measurement	4 - 40
4.5.1 Low Power Characteristics of Waveguide FDPS	4 - 40
4.5.1.1 Effects of Internal Field and Magnetization on Phase Shifter Performance	4 - 46
4.5.1.2 Effects of Thickness on Loss	4 - 64
4.5.1.3 Effects of Dimensional Changes and Dielectric Loading	4 - 70
4.5.2 Below Resonance Operation of FDPS	4 - 78
4.5.3 High Power Characteristics of FDPS	4 - 82
5 PRINCIPAL CONCLUSIONS	5 - 1

LIST OF ILLUSTRATIONS

<u>Figure</u>		<u>Page</u>
1	Cutaway View of a Waveguide Latching Phase Shifter	3 - 3
2	Hysteresis Loop of a High Remanence (i. e. , "Square-Loop") Ferrite	3 - 3
3	Relative Directions of the Saturation Magnetization \vec{M}_s and of the Net Effective Static Magnetic Field Acting on a Single Domain	3 - 8
4	Conventional Spinwave Manifold Showing the Dependence of Availability Spinwave Numbers (k) on Operating Frequency (ω)	3 - 20
5	Normalized Spinwave Dispersion Curve Assuming $H_1 = 4\pi M_s$ (Polder-Smit Domains)	3 - 23
6	Threshold Field of Polder-Smit Domains as a Function of Normalized Magnetization	3 - 24
7	A Waveguide Nonreciprocal Latching Phase Shifter	3 - 25
8	Twin-Slab Model for "Single-Toroid" Ferrite Latching Phase Shifter	3 - 25
9	A Ferrite Loaded Rectangular Waveguide	3 - 27
10	A Structure with Electromagnetic Symmetry about o	3 - 28
11	Dielectric Loaded Twin-Slab Structure	3 - 31
12	Hysteresis Loop of Ferrimagnetic Materials	3 - 35
13	Vibrating Sample Magnetometer	4 - 2
14a	X Band Resonance Spectrometer	4 - 4
14b	C Band Resonance Spectrometer	4 - 4
15	Furnace Arrangement for Simple Measurement of Curie Temperature. Explanatory Comments are in the Text	4 - 5
16	Dielectric Constant and Dielectric Loss Tangent Measurement Equipment (X Band)	4 - 6
17	General Electric XRD-5 X ray Diffractometer in Sperry Microwave Electronics Company Laboratory	4 - 7

LIST OF ILLUSTRATIONS (Cont'd)

<u>Figure</u>		<u>Page</u>
18	Square Loop Tester	4 - 8
19	Schematic of Square Loop Tested Modified for Measuring the Remanent Magnetization	4 - 9
20	Richert Metallograph Used for Material Evaluation	4 - 11
21	Fisher Sub-Sieve Sizer	4 - 12
22	Laboratory Setups for Measurement of Attenuation and Phase Shift at Low Power Levels	4 - 13
23	Power-Ratio Setup for Measuring Attenuation at High Power Levels	4 - 15
24	Typical Voltage and Current Waveforms Observed During Fast Switching of the Ferrite Toroids. The Switching Time T_s is also Shown	4 - 16
25	Photomicrographs of 60% Gadolinium Substituted YIG and 30% Gadolinium Substituted YIG	4 - 28
26	Remanent Magnetization and Coercive Force Dependence on Temperature with Drive Current (I_D) Constant	4 - 30
27	Remanence Ratio and Coercive Force Versus Temperature with Constant Drive Current I_D	4 - 31
28	Remanent Magnetization and Coercive Force Dependence on Temperature with H_d/H_c Constant	4 - 32
29	Remanent Magnetization and Coercive Force Dependence on Temperature with Drive Current (I_D) Constant	4 - 33
30	Remanent Magnetization and Coercive Force Versus Temperature with Constant Drive Current I_D	4 - 35
31	Variation of the Saturation Magnetization with Temperature for Yttrium Gadolinium Iron Garnet	4 - 36
32	The Variation of Saturation Magnetization with Temperature for Aluminum Substituted 85% YIG - 15% GdIG	4 - 37
33	Variation of Saturation Magnetization with Temperature for Aluminum Substituted 80% YIG 20% GdIG	4 - 38
34	Variation of Saturation Magnetization with Temperature for Aluminum Substituted 75% YIG 25% GdIG	4 - 38

LIST OF ILLUSTRATIONS (Cont'd)

<u>Figure</u>		<u>Page</u>
35	Variation of Saturation Magnetization with Temperature for Aluminum Substituted 70% YIG 30% GdIG	4 - 39
36	Variation of Saturation Magnetization with Temperature for Aluminum Substituted 50% YIG 50% GdIG	4 - 39
37	Cutaway Illustration of a Typical Nonreciprocal Digital Phase Shifter Structure	4 - 41
38	An Internal Toroid Latching Phase Shifter	4 - 43
39	Twin Slab Model	4 - 43
40	Differential Phase Shift vs Normalized Waveguide Width for a Latching Phase Shifter with Effective Internal Field as a Parameter	4 - 47
41	Loss Per 360° of Differential Phase Shift vs Normalized Waveguide Width for a Latching Phase Shifter with Effective Internal Field as a Parameter	4 - 48
42	Differential Phase Shift vs Effective Internal Field for a Latching Phase Shifter	4 - 55
43	Loss Per 360° of Differential Phase Shift vs Effective Internal Field for a Latching Phase Shifter	4 - 56
44	Separation of Losses in a Latching Phase Shifter	4 - 58
45	Loss Per 360° vs Frequency Normalized Magnetization with Anisotropy Field as Parameter	4 - 59
46	Variation of Loss Per 360° with Saturation Magnetization in Aluminum-Doped YIG. Experimental Data Obtained in Configuration Shown in Table V	4 - 61
47	Loss Per 360° vs Frequency for Ferrite 83-8 in X Band and C Band Phase Shift Structures, Shown in Table VI	4 - 61
48	Loss Per 360° vs Magnetization for Ferrite 83-8. Configuration Shown in Table VI	4 - 62
49	Variation of Differential Phase Shift as a Function of of Normalized Saturation Magnetization	4 - 63

LIST OF ILLUSTRATIONS (Cont'd)

<u>Figure</u>		<u>Page</u>
50	Loss Per 360° of Differential Phase Shift vs Intrinsic Linewidth	4 - 65
51	C Band Loss Per 360° vs Polycrystalline Linewidth. Experimental Data Obtained in the Configuration Shown in Table V	4 - 66
52	S Band Loss Per 360° vs Polycrystalline Linewidth. Experimental Data Obtained in the Configuration Shown in Table V	4 - 67
53	Differential Phase Shift vs Normalized Thickness of Dielectric Load with Load Dielectric Constant as a Parameter	4 - 71
54	Comparison of Performance of a Typical Ferrite and a Typical Garnet in a FDPS	4 - 72
55	Differential Phase Shift vs Normalized Frequency with Waveguide Width as a Parameter	4 - 74
56	Differential Phase Shift vs Normalized Frequency with Dielectric Load Thickness as a Parameter	4 - 75
57	Phase Slope vs Normalized Waveguide Width with Dielectric Load Thickness as a Parameter	4 - 76
58	Phase Slope vs Normalized Waveguide Width with Dielectric Load Thickness as a Parameter	4 - 77
59	Helical Phase Shifter Structure Used for Magnetic Loss Measurements	4 - 78
60	Magnetic Loss vs Frequency for G-289-6J in the Helix Structure	4 - 80
61	Magnetic Loss vs Frequency for G290R in the Helix Structure	4 - 80
62	Magnetic Loss vs Frequency for G404J in the Helix Structure	4 - 81
63	Differential Phase Shift and Loss vs Frequency in the Helix Structure	4 - 81

LIST OF ILLUSTRATIONS (Cont'd)

<u>Figure</u>		<u>Page</u>
64	Ferrite Critical Field Dependence on the Frequency Normalized Saturation Magnetization for Aluminum and Gadolinium Substituted YIG. Experimental Data from the Configuration of Table V	4 - 84
65	Critical Power Level Variation with Applied DC Magnetic Field in a Dielectrically Loaded Ferrite Slab Configuration	4 - 86
66	Loss and Phase Shift Versus Applied Field in the Dielectric-Loaded Ferrite Slab Configuration Shown in Figure 65	4 - 87

1 SYNOPSIS

This report describes the results of work performed by Sperry Microwave Electronics Company for the Rome Air Development Center and the Advanced Research Projects Agency during the first semiannual period of Contract No. AF30(602)-4122(ARPA Order No. 550).

The objectives of this program are

1. To determine the limitations imposed by intrinsic material parameters on the peak power handling capacity of ferrite digital phase shifters,
2. To develop ferrimagnetic materials with improved properties for use in high peak power digital phase shifters, and
3. To evaluate both the improved materials and various existing materials in appropriate rf structures at frequencies in L, S, C and X bands.

Emphasis is placed on attaining high peak power capacity even at the expense of some degradation of other performance characteristics. To permit an assessment of the cost of attaining a specified peak power capacity in terms of possible degradation of other performance characteristics, the interrelationships between peak power capacity, insertion loss, phase shift, temperature stability, etc., are examined. These interrelationships arise from the dependence of each of these device characteristics on intrinsic material parameters. Such studies highlight the "tradeoffs" that might be made to obtain the optimum digital phase shifter for a given high peak power application.

A brief description of the contents of each section of this report follows.

Section 2

Background information and a statement of the program objectives are presented.

Section 3

This section presents both a qualitative and an analytical discussion on how the intrinsic material parameters of remanent state ferrimagnetic materials

influence the operating characteristics of ferrite digital phase shifters (FDPS). Emphasis is placed on clearly describing the limitations imposed by intrinsic material parameters on high peak power operation.

The section begins with a qualitative description of the operating principles of a waveguide nonreciprocal digital phase shifter. Following the introductory comments is a discussion of a physical model for remanent state ferrites which appears to account quite well for the experimentally observed properties of these materials. The central concept used in the development of the physical model is that a remanent state material is made up of a substantial number of magnetic domains. Each domain is a magnetically saturated region whose properties can be described by conventional theory of saturated media. The behavior of the domains differs because each may have a different shape, and the magnetization of the various domains points in different directions. Each of these domains then experiences an "effective" bias field whose magnitude is related to intrinsic material parameters and to the shape of the domain. From the physical model a mathematical model for remanent state ferrites is developed based on averaging the properties of the individual saturated regions to obtain a set of effective properties for the bulk remanent state material. The mathematical characterization, thus, takes the form of a complex "average" tensor permeability which includes the effects of intrinsic linewidth, magnetocrystalline anisotropy, remanent magnetization, and an average demagnetizing field appropriate to the distribution of magnetic domains. The distribution and shape of the magnetic domains, and hence the value of the average demagnetizing field, are determined to a large extent by sample shape and the remanence ratio of the material.

The discussion of physical and mathematical models of remanent state ferrites is followed by a description of analysis techniques which can be used to obtain numerical relationships between the transfer characteristics of a phase shifter (i.e., loss and phase) and the dimensional and material parameters of the structure. As an example of these techniques, the propagation constant equation is derived for a typical digital phase shifter model.

An analysis of peak power effects in remanent state ferrites is next presented. The analysis is based on the multidomain model of remanent materials

mentioned previously. Since each domain is a magnetically saturated region, the peak power effects on a domain by domain basis may be interpreted in terms of the spin wave interactions of the well known Suhl-Schloemann theory of nonlinear effects in saturated media. Each domain may experience a different effective bias field and hence may have a different threshold power level from all other domains. The threshold level observed experimentally by comparing power levels at the output and input of a phase shifter is the threshold level of the "worst" or most unfavorably biased domain. In the usual FDPS, the occurrence of the first order nonlinear process is the factor which limits peak power performance. In the first order process energy from the uniform precession is scattered and lost to half-frequency spin wave modes. For this process the threshold field h_{crit} is proportional to the spin wave linewidth ΔH_k and inversely proportional to the normalized saturation magnetization ω_m/ω . Since ΔH_k is a function of the wave number k ($\Delta H_k \approx A + Bk^2$), obviously h_{crit} depends dramatically upon the availability of low k number half-frequency spin waves. In remanent state ferrites the availability of half-frequency spin waves with low k values in turn depends upon ω_m/ω through the dependence of each domain's effective bias field on demagnetizing terms.

For even the most unfavorably biased domains (Polder-Smit type domains) low k spin waves are no longer available when ω_m/ω drops below about 0.3. As a result of the k dependence of ΔH_k , these domains will exhibit an abrupt increase in ΔH_k , and hence h_{crit} , for $\omega_m/\omega \approx 0.3$. For other types of domains the restriction of scattering to high k states (and increase in h_{crit}) will occur at larger values of ω_m/ω . Thus, the rate of change of h_{crit} with ω_m/ω will vary with the type of domains present in the toroid. In any event, however, h_{crit} must increase rapidly in the vicinity of 0.3.

Thus, the threshold field, and hence the peak power handling capacity can be controlled by changes in the ΔH_k of low k spin waves (e.g., by rare earth doping of garnets) or by changing ω_m/ω (e.g., by aluminum doping of garnets).

The final portion of this section deals with the ferrite square loop properties of interest in FDPS. The dependence of remanence ratio (R_r) coercive force (H_c) and switching time T_s are related to the intrinsic and ceramic properties of the ferrite.

Section 4

This section presents a discussion and comparison of the results of the analytical and experimental phases of the program. The results presented include

1. Numerical predictions of phase shifter performance characteristics obtained from a computer-aided solution of the exact boundary value problem, including the effects of losses, for the waveguide digital phase shifter configuration on which most of the experimental measurements were performed,
2. Extensive experimental data depicting the effect of material and dimensional parameters on low and high peak power digital phase shifter characteristics,
3. Experimental data depicting the dependence of the microwave and square loop material properties on preparation techniques and ambient temperature, and
4. Experimental data depicting phase shift and magnetic loss variations at frequencies below resonance.

From these data it can be seen that

1. Good agreement is obtained between theoretical performance predictions and experimental data,
2. Material parameters and structural dimensions can be selected to optimize phase shifter performance in terms of
 - Loss per 360° of differential phase shift,
 - Peak power handling capacity,
 - Phase shift per unit length, or
 - Stability of performance over a large frequency range, or
 - Stability of performance over a large temperature range, etc.,

but if more than one of these capabilities is required simultaneously then compromise, rather than ultimate, characteristics must be accepted,
3. Peak power handling capacity at a given frequency can be increased by increasing the spin wave linewidth of the material and/or decreasing its saturation magnetization,
4. Low power insertion loss increases with increasing intrinsic linewidth,
5. High density materials lead to the best overall ferrite characteristics for FDPS applications and

004002

6. Magnetic losses in some remanent materials appear to decrease at frequencies below resonance at about the same rate as at frequencies above resonance, much the same as they do in magnetically saturated materials.

Section 5

This section presents a summary of the conclusions deduced from the results of this study. Typical tradeoffs between peak power, insertion loss, and phase shift per unit length are illustrated in Table VII.

004002

BLANK PAGE

2 INTRODUCTION

2.1 BACKGROUND OF PROGRAM

004002

Research and development efforts on ferrite digital phase shifters (FDPS) have established certain guidelines useful in the selection of materials and structures for these devices. These efforts have established that materials from the magnesium-manganese ferrite and the rare earth substituted yttrium aluminum iron garnet families are the chief materials of interest. The structures of principal interest are dielectrically loaded rectangular ferrite toroid configurations in reduced width waveguide. Within these basic guidelines, certain refinements of the material and structural parameters will serve to optimize the performance characteristics of digital phase shifters. For example, rare earth doping may be utilized to increase the peak power handling capacity of the ferrite and gadolinium substitutions can stabilize the magnetization of the ferrite, and hence the phase shift of the devices over wide temperature ranges. The limitations of these and other such techniques and the interrelation of the various device properties have not been clear.

It is the purpose of this program to determine these limitations, develop the necessary improvements in the materials, and establish quantitative information which will clearly define the tradeoffs involved in obtaining satisfactory peak power performance with minimum sacrifice of insertion loss, switching characteristics, etc. To this end, a combined theoretical and experimental program have been initiated. The theoretical and experimental efforts are closely coordinated. It is felt that a more complete understanding of the physical processes involved in remanent state devices has been obtained, and that the analytical techniques developed can permit the prediction of the intrinsic material parameters required to yield prescribed phase shifter characteristics. In addition, an investigation is being performed on the effects of material preparation techniques on the material parameters which are found to be important in determining phase shifter performance.

2.2 PROGRAM OBJECTIVES

The basic program objectives are as follows:

- Improvement and evaluation of ferrite and garnet materials for use in digital phase shifters at L, S, C, and X bands will be pursued with increased effort at the lower frequency bands. Emphasis will be placed on development of peak power capability of the order of 100 kilowatts while generating insertion losses of 1 db or less and phase stability with temperature variation over the military range.
- Microwave digital phase shift structures will be studied with special emphasis on materials derived in this program combined with the requirements for high switching speed, low switching power, low loss, low holding power, compact configuration, low unit cost, and high peak and average power handling capability.

3 OPERATING DYNAMICS OF FERRITE* DIGITAL PHASE SHIFTERS

3.1 BASIC CONCEPT OF FERRITE DIGITAL PHASE SHIFTERS (FDPS)

Ferrite loaded transmission structures have been used for a number of years to obtain electrically-controllable reciprocal and nonreciprocal phase shift.¹ The operation of early ferrite phase shifters was based on changes in the propagation constant of the ferrite loaded structure which occur when the rf permeability of the ferrite is varied by controlling the ferrite's dc magnetic bias field. These variable-bias-field phase shifters were rather bulky in size and slow in switching from one phase shift value to another, due to the substantial electromagnet required. In addition, dc power consumption was high because of the holding current required to maintain a given phase shift. Such characteristics are unacceptable in many applications. Beam steering in a rapid scanning array, for example, requires high performance, variable phase shifters capable of fast switching, requiring low switching and holding power, and producible in large numbers at low cost.

The ferrite "digital"² or "latching" phase shifter concept represents a significant and promising advance in phase shifters for rapid scanning array application. The innovation that distinguishes the digital phase shifter from its predecessors is the utilization, as the phase shift element, of a "square hysteresis loop" ferrite physically arranged to form a closed magnetic path. Operation is then based on the change in propagation constant which occurs when the rf permeability of the ferrite is varied by changing the remanent magnetization of the ferrite. The remanent magnetization is varied by switching from one remanent state to another around major or minor hysteresis loops. Digital phase shifters can be realized in rectangular and cylindrical waveguide, coaxial, stripline, helical, meander and other transmission structures.

A cutaway view of a particularly useful nonreciprocal ferrite digital phase shifter is shown in Figure 1. In this structure, the phase shifting element is a rectangular toroid of "square loop" ferrite positioned along the axis of the rectangular waveguide. A single turn of wire coaxial to the ferrite toroid provides a path for the current pulses which magnetize the ferrite to either of two remanent magnetization states

* The word "ferrite" is used in this report to represent any ferrimagnetic material.

¹ B. Lax and K. J. Button, Microwave Ferrites and Ferrimagnetics, McGraw-Hill Book Company, Inc., 1962. pp. 589-609.

² M. A. Treuhaft and L. M. Silber, "Use of Microwave Ferrite Toroids to Eliminate External Magnets and Reduce Switching Power," Proc. IRE, vol. 46, p. 8, 1958.

($+M_r$ or $-M_r$) as shown in Figure 2. Bias power is thus required only in switching from one state to the other, i.e., no holding current is required. Corresponding to these states, there are phase shifts $+\phi_r$ and $-\phi_r$ and their difference, $\Delta\phi_r$, is the nonreciprocal, differential phase shift of the ferrite "bit." In the device several bits of different values are used in cascade to achieve step-wise variable, or digital, phase shift by activating (charging to $+M_r$) the appropriate combinations of bits, with the remaining bits left in the "inactive" ($-M_r$) state. The dielectric core of the toroid helps to concentrate the rf energy in the ferrite. If a total adjustable phase shift of 360° is required, for example, the lengths of the toroid segments might be selected so that phase shifts of 180° , 90° , 45° , 22.5° , 11.25° , and 5.625° are obtained. The result is a phase shifter capable of exhibiting any differential phase shift from 0° to 360° in 5.625° steps. Common terminology is to call such a device a six-digit or six-bit phase shifter.

As implied above, the FDPS may be devised in a variety of transmission structures and may be nonreciprocal or reciprocal, depending upon the manner in which the rf fields couple to the magnetic moments of the ferrite. All of the ferrite toroid may be immersed in the rf field or, alternatively, to aid in temperature stabilization, only a portion of the ferrite may be immersed in the rf field with the magnetic path completed by external ferrite segments.³ However, in all the varieties of ferrite digital phase shifters, the properties of the ferrite itself have the dominant role in determining the "quality" of the device.

The sections that follow discuss and analyze the role of the ferrite properties in determining the operating characteristics of ferrite digital phase shifters. Material requirements for reciprocal and nonreciprocal phase shifters are very similar. Emphasis in the analysis and experiments reported here is placed on the nonreciprocal variety which, thus far, appears to be most promising for phased array application.

³ E. Stern and W. J. Ince, "Temperature Stabilization of Unsaturated Microwave Ferrite Devices," 11th Annual Conf. on Magnetism and Magnetic Materials, San Francisco (November 1965); *J. Appl. Phys.* **37**, 1075 (1 March 1966).

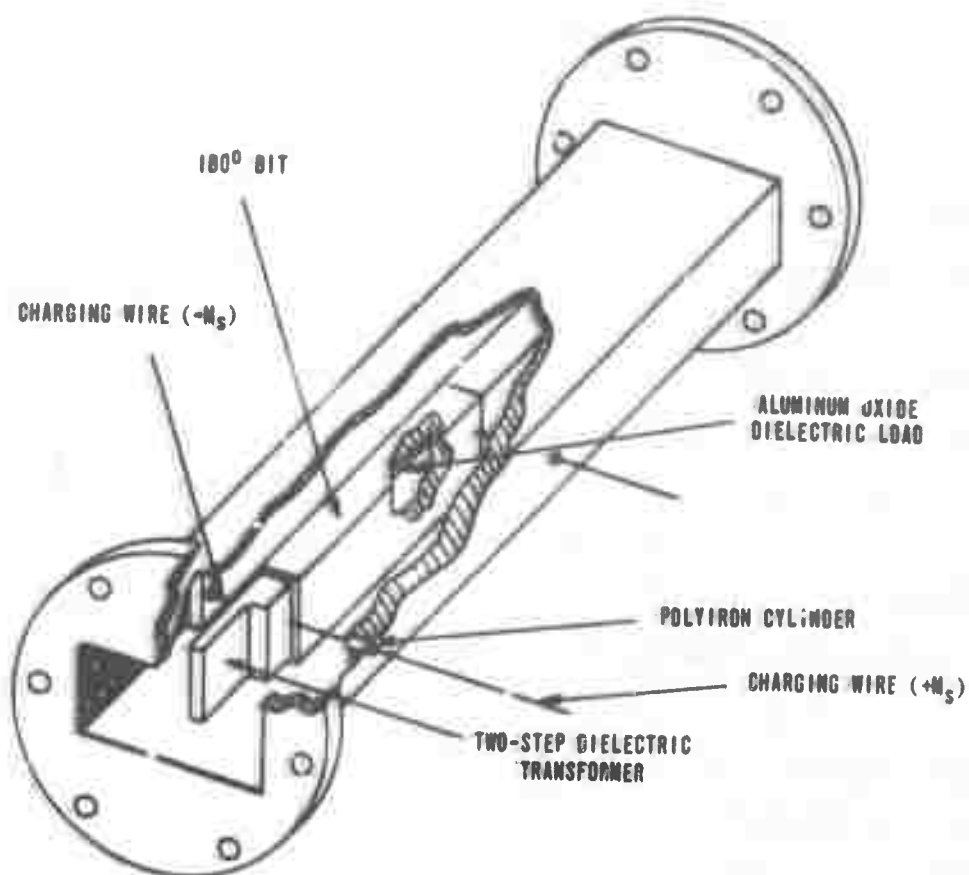


Figure 1. Cutaway View of a Waveguide Latching Phase Shifter

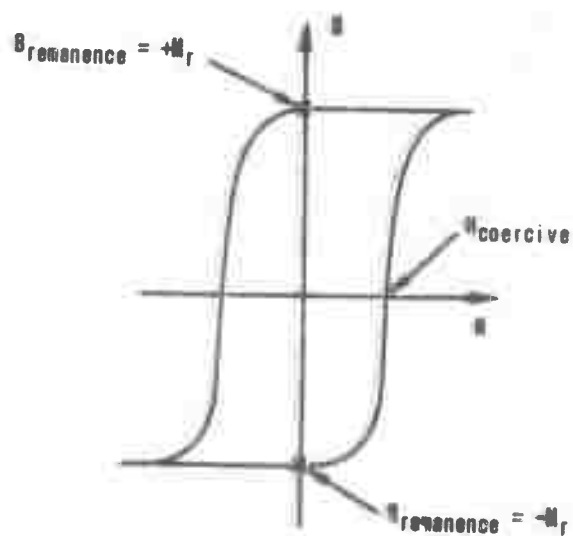


Figure 2. Hysteresis Loop of a High Remanence (i.e., "Square-Loop") Ferrite

3.2 ANALYTICAL MODELS OF FERRITE DIGITAL PHASE SHIFTERS

The proper evaluation of materials for use in ferrite digital phase shifters requires the availability of at least a qualitative physical model for the materials and other elements of the phase shifter. Such models serve as an indispensable aid in correlating and interpreting experimental data. To be able to predict the material parameters required for producing a phase shifter with specified performance characteristics or, alternatively, to predict how a given material will perform in a phase shifter without actually carrying out an experimental test, it is necessary to have an accurate mathematical model for the material and other elements of the phase shifter. In addition to the mathematical models, analysis techniques are required which enable the transfer characteristics of the phase shifter to be related mathematically to the intrinsic material and dimensional parameters of the device structure. The validity of the mathematical models and analysis techniques must then be carefully evaluated by comparison of analytical predictions with the results of experiments performed on laboratory models of the phase shifter. With such models and analysis techniques available, the performance of ferrite in different frequency bands and with different geometries can be evaluated without having to resort to an actual laboratory measurement for each geometry and frequency.

The principal difficulty in generating analytical models for ferrite devices is in the representation of the ferrite itself. If the ferrite is magnetically saturated, then its microwave magnetic properties, including magnetic losses, can be represented by the Landau - Lifshitz permeability tensor.⁴ However, for a partially magnetized or remanent state material, such as those used in ferrite digital phase shifters, the Landau - Lifshitz permeability tensor is not an accurate representation of its magnetic properties and a more general representation, based on a generalized physical model of the ferrite, must be derived.

⁴ B. Lax and K. J. Button, Ibid, P 154.

3.2.1 Microwave Magnetic Properties of Partially Magnetized Ferrites

The representation of the microwave magnetic properties, particularly of magnetic losses, in partially magnetized ferrites is complicated by the existence of a multiplicity of magnetic domains of various shapes and orientations. It has been suggested by Ince and Stern⁵ and others that the remanent state ferrites in digital phase shifters can be treated as though the ferrite is magnetically saturated with an equivalent saturation magnetization equal to the actual remanence magnetization, so far as phase shift is concerned, and totally unmagnetized so far as losses are concerned. Magnetic losses are then represented by the artifice of a magnetic loss tangent ($\tan \delta = \frac{\mu''}{\mu'}$) in analogy with the lossy initial permeability of unmagnetized samples. This characterization suffers from the fact that it obscures the relation of the magnetic losses to the intrinsic parameters of the ferrite. Magnetic loss tangents of remanent state ferrite toroids are not intrinsic parameters of the material. The measured value of loss tangent varies with the manner in which it is measured, the frequency of the measurement, and so forth. Thus, in order for a magnetic loss tangent characterization of the losses in a device to be truly meaningful, the measurement frequency and the geometry of the test configuration (i.e., the manner in which the rf field couples to the magnetic moments of the ferrite) must be the same as those of the operational device.

Another issue arising in the characterization of remanent state ferrite toroids is the question of the value of the effective internal bias field H_i of the material. Because there is no externally applied bias field, a possible starting point is to assume that H_i is zero. This is in fact the procedure followed by most other investigators. However, inasmuch as a resonance type of loss has been experimentally observed in remanent state toroids,⁶ it appears that the effective internal bias field is not zero, and this fact must be taken into account in any accurate model for partially magnetized materials.

⁵ W.J. Ince and E. Stern, "Non-Reciprocal Remanence Phase Shifters in Rectangular Waveguide," IEEE International Convention Record, Part 5, p. 33, 1966.

⁶ Final Report on "Advanced Ferrimagnetic Materials Applied To Digital Phase Shifters," Sperry Microwave Electronics Company, Report on ARPA Order No 550, Program Code No 4730, RADC Contract No AF-30(602)3490, January 1966, PP 130-160.

Because of the inherent disadvantages of available characterizations of the microwave magnetic properties of remanent state ferrites, a strong effort has been made to develop a model which accounts for observed phenomena and which can be used for accurate prediction of phase and loss characteristics in ferrite devices such as the digital phase shifter. In the "new" model for remanent state or partially magnetized ferrites, magnetic losses are accounted for via an intrinsic resonance linewidth and the effects of a nonzero effective internal field are included. This model, to be described below, appears to account rather completely for the observed loss and phase properties of remanent state ferrite toroids.

The physical "picture" on which the new model is based is as follows. A saturated ferrite sample is composed of a single magnetic domain, i.e., all the microscopic moments in the material are aligned. However, in a remanent state or partially magnetized material, the microscopic magnetic moments are no longer all aligned. Instead, the sample will be composed of a number of magnetic domains, each of which is completely saturated (i.e. the moments are all aligned), but with the moments in various domains oriented in different directions. Each domain has associated with it an effective bias field which arises from magnetocrystalline anisotropy effects and from demagnetizing fields that result from the rf demagnetizing factors associated with the particular domain shape and environment (i.e. similar to the Polder - Smit argument).⁷ The effective field of each domain may be different, and as a consequence in each domain the magnetization will exhibit precessional resonance at a characteristic frequency determined by the anisotropy field and the particular demagnetizing field of the domain. In general then, a spatial averaging process must be carried out to mathematically relate the net rf magnetization to the rf magnetic field, and it is apparent that the domain structure will exert an appreciable influence on the macroscopic properties of the material.

The permeability tensor for partially magnetized ferrites can be obtained by an extension of a concept suggested by Rado,⁸ who made an extensive qualitative examination of arbitrarily magnetized ferrite media. In such media the intrinsic tensor relationship may be written in the form

⁷ D. Polder and J. Smit, "Resonance Phenomena in Ferrites," Rev. Modern Physics, 25, 89(1953).

⁸ G. T. Rado, "On the Electromagnetic Characterization of Ferromagnetic Media: Permeability Tensors and Spin Wave Equations, "IRE Trans. on Ant. and Prop., vol. AP-4, p. 512 (1956).

$$\begin{bmatrix} \langle b_x \rangle \\ \langle b_y \rangle \\ \langle b_z \rangle \end{bmatrix} = \mu_0 \begin{bmatrix} \langle \mu_{11} \rangle & \langle \mu_{12} \rangle & \langle \mu_{13} \rangle \\ \langle \mu_{21} \rangle & \langle \mu_{22} \rangle & \langle \mu_{23} \rangle \\ \langle \mu_{31} \rangle & \langle \mu_{32} \rangle & \langle \mu_{33} \rangle \end{bmatrix} \begin{bmatrix} \langle h_x \rangle \\ \langle h_y \rangle \\ \langle h_z \rangle \end{bmatrix} \quad (1)$$

where $\langle b \rangle$ and $\langle h \rangle$ are the spatial averages of the time-varying components of the magnetic induction and the magnetic field intensity. The $\langle \mu_{jk} \rangle$ are effective permeability components averaged over several domains and, as such, are directly measurable quantities. Under the assumptions of Rado's theory, the relation between the macroscopic "point" field quantities \vec{b} and \vec{h} (not average) is given by a spin wave equation at points within the domain walls and by a tensor inside the domains, but the experimentally important relation between the average quantities $\langle \vec{b} \rangle$ and $\langle \vec{h} \rangle$ is given by a tensor everywhere. Relating $\langle \mu_{jk} \rangle$ to the measurable intrinsic magnetic properties of the ferrite is, in general, exceedingly difficult.

As suggested by Rado, the relation $\langle \mu_{jk} \rangle$ between the effective rf fields $\langle \vec{b} \rangle$ and $\langle \vec{h} \rangle$ can sometimes be obtained by performing spatial averages on the relation μ_{jk} between the "point" rf fields \vec{b} and \vec{h} of an appropriate saturated media problem. With this in mind the relationships between \vec{b} and \vec{h} for a ferrite sample consisting of a single domain magnetized by an applied magnetic field will now be considered.* The saturation magnetization \vec{M}_s of the domain and the net effective magnetic field \vec{H}_i are assumed to be oriented in different directions as shown in Figure 3.

* The following derivation closely follows that of J. L. Allen as given in "The Analysis of Ferrite Phase Shifters Including the Effects of Losses," Ph.D. Dissertation, Georgia Institute of Technology, May, 1966.

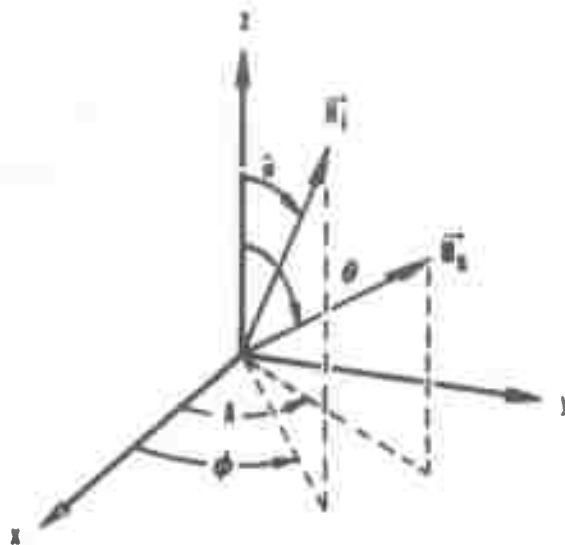


Figure 3. Relative Directions of the Saturation Magnetization \vec{M}_s and of the Net Effective Static Magnetic Field Acting on a Single Domain

The equation of motion for the macroscopic magnetization, including losses via the Landau-Lifshitz damping term, is

$$\frac{d\vec{M}}{dt} = \gamma_e (\vec{M} \times \vec{H}) - \frac{\alpha}{M} \vec{M} \times \frac{d\vec{M}}{dt} \quad (2)$$

where $\vec{M} = \vec{M}_s + \vec{m}e^{j\omega t}$ $\vec{H} = \vec{H}_1 + \vec{h}e^{j\omega t}$

$\vec{M}_s = |\vec{M}_s| [\vec{i} \sin \theta \cos \phi + \vec{j} \sin \theta \sin \phi + \vec{k} \cos \theta] = \text{saturation magnetization}$

$\vec{h} = \vec{i}h_x + \vec{j}h_y + \vec{k}h_z = \text{rf magnetic field}$

$\vec{m} = \vec{i}m_x + \vec{j}m_y + \vec{k}m_z = \text{rf magnetization}$

$\gamma_e = \gamma(1 + \alpha^2)$, $\alpha = \frac{1}{\omega\tau}$, $\tau = \text{damping time-constant}$

$\vec{H}_1 = \vec{i}H_x + \vec{j}H_y + \vec{k}H_z = \text{net effective field acting on a single domain}$

$$= |\vec{H}_1| [\vec{i} \sin B \cos A + \vec{j} \sin B \sin A + \vec{k} \cos B]$$

Expanding Equation 2, equating coefficients of $e^{j\omega t}$, and after considerable algebra the following small signal permeability is obtained.

$$\vec{\mu} = \mu_0 \begin{bmatrix} \mu_{11} & \mu_{12} & \mu_{13} \\ \mu_{21} & \mu_{22} & \mu_{23} \\ \mu_{31} & \mu_{32} & \mu_{33} \end{bmatrix} \quad (3)$$

$$\mu_{11} = 1 + \frac{\gamma_e |\vec{M}_s|}{\Delta} \left\{ \left| \gamma_{e_z} H_z (\cos \theta - \alpha \sin^2 \theta \sin \phi \cos \phi) + \gamma_{e_y} H_y (\sin \theta \sin \phi + \alpha \sin \theta \cos \theta \cos \phi) \right| + j \left[\omega \alpha (\cos^2 \theta + \sin^2 \phi \sin^2 \theta) + \frac{1}{\omega} (\gamma_{e_z} H_z \gamma_{e_x} H_x \sin \theta \sin \phi - \gamma_{e_x} H_x \gamma_{e_y} H_y \cos \theta) \right] \right\}$$

$$\mu_{12} = \frac{-j \gamma_e |\vec{M}_s|}{\Delta} \left\{ \omega \cos \theta + \alpha \sin^2 \theta \cos \phi (\omega \sin \phi + j \gamma_{e_z} H_z \cos \phi) - \frac{1}{\omega} (\gamma_{e_x} H_x) (\gamma_{e_x} H_x \cos \theta + \gamma_{e_z} H_z \sin \theta \cos \phi) + j (\alpha \gamma_{e_x} H_x \cos \theta - \gamma_{e_y} H_y) \sin \theta \cos \phi \right\} \quad (4)$$

$$\mu_{13} = \frac{-j \gamma_e |\vec{M}_s|}{\Delta} \left\{ -\omega \sin \theta \sin \phi + \omega \alpha \cos \theta \sin \theta \sin \phi + \frac{1}{\omega} \gamma_{e_x} H_x \sin \theta (\gamma_{e_x} H_x \sin \phi - \gamma_{e_y} H_y \cos \phi) + j \alpha \sin^2 \theta \cos \phi (2 \gamma_{e_x} H_x \sin \phi - \gamma_{e_y} H_y \cos \phi) - j \gamma_{e_z} H_z \sin \theta \cos \phi \right\}$$

$$\mu_{21} = \frac{-j \gamma_e |\vec{M}_s|}{\Delta} \left\{ -\omega \cos \theta + \omega \alpha \sin^2 \theta \sin \phi \cos \phi + \frac{1}{\omega} \gamma_{e_y} H_y (\gamma_{e_y} H_y \cos \theta - \gamma_{e_z} H_z \sin \theta \sin \phi) + j \sin \theta \sin \phi (\alpha \gamma_{e_y} H_y \cos \theta - \alpha \gamma_{e_z} H_z \sin \theta \sin \phi - \gamma_{e_x} H_x) \right\}$$

$$\begin{aligned}
\mu_{22} &= 1 + \frac{\gamma_e |\vec{M}_s|}{\Delta} \left\{ \gamma_e H_z (\cos \theta + \alpha \sin^2 \theta \sin \phi \cos \phi) \right. \\
&\quad + \gamma_e H_z \sin \theta (\cos \phi - \alpha \cos \theta \sin \phi) + j \omega \alpha (\cos^2 \theta + \cos^2 \phi \sin^2 \theta) \\
&\quad \left. + \frac{1}{\omega} \gamma_e H_y (\gamma_e H_x \cos \theta - \gamma_e H_z \sin \theta \cos \phi) \right\} \\
\mu_{23} &= \frac{-j \gamma_e |\vec{M}_s|}{\Delta} \left\{ \omega \sin \theta \cos \phi + \omega \gamma \cos \theta \sin \theta \sin \phi \right. \\
&\quad + \frac{1}{\omega} \gamma_e H_y (\gamma_e H_x \sin \theta \sin \phi - \gamma_e H_y \sin \theta \cos \phi) \\
&\quad \left. + j \alpha \gamma_e H_x \sin^2 \theta \sin^2 \phi - j \gamma_e H_z \sin \theta \sin \phi - j \alpha \gamma_e H_y \sin^2 \theta \sin \phi \cos \phi \right\} \\
\mu_{31} &= \frac{-j \gamma_e |\vec{M}_s|}{\Delta} \left\{ \omega \sin \theta \sin \phi + \omega \alpha \sin \theta \cos \theta \cos \phi \right. \\
&\quad + \frac{1}{\omega} \gamma_e H_z (\gamma_e H_x \cos \theta - \gamma_e H_z \sin \theta \sin \phi) \\
&\quad \left. + j \alpha \gamma_e H_y \cos^2 \theta - j \gamma_e H_x \cos \theta - j \alpha \gamma_e H_z \sin \theta \cos \theta \sin \phi \right\} \\
\mu_{32} &= \frac{-j \gamma_e |\vec{M}_s|}{\Delta} \left\{ -\omega \sin \theta \cos \phi + \omega \alpha \sin \theta \cos \theta \sin \phi \right. \\
&\quad + \frac{1}{\omega} \gamma_e H_z (\gamma_e H_z \sin \theta \cos \phi - \gamma_e H_x \cos \theta) \\
&\quad \left. - j \alpha \gamma_e H_x \cos^2 \theta - j \gamma_e H_y \cos \theta + j \alpha \gamma_e H_z \cos \theta \sin \theta \cos \phi \right\} \\
\mu_{33} &= 1 + \frac{\gamma_e |\vec{M}_s|}{\Delta} \left\{ \alpha \gamma_e H_x \sin \theta \cos \theta \sin \phi + \gamma_e H_y \sin \theta \sin \phi \right. \\
&\quad - \alpha \gamma_e H_y \sin \theta \cos \theta \cos \phi + \gamma_e H_x \sin \theta \cos \phi \\
&\quad \left. - j \frac{1}{\omega} \gamma_e H_z (\gamma_e H_x \sin \theta \sin \phi + \gamma_e H_y \sin \theta \cos \phi) + j \omega \alpha \sin^2 \theta \right\}
\end{aligned}$$

$$\text{where } \Delta = \left[-\omega^2 - (\omega\alpha)^2 + (\gamma_e |\vec{H}_1|)^2 \right] + j \left[2\omega\alpha\gamma_e H_x \sin\theta \cos\phi + 2\omega\alpha\gamma_e H_y \sin\theta \sin\phi + 2\omega\alpha\gamma_e H_z \cos\theta \right]$$

$$H_x = |\vec{H}_1| \sin B \cos A$$

$$H_y = |\vec{H}_1| \sin B \sin A$$

$$H_z = |\vec{H}_1| \cos B$$

If θ and B are both zero, corresponding to a saturated media with saturation magnetization and bias field oriented in the same direction, the permeability given in Equation 4 reduces to the familiar Landau-Lifshitz form.

As previously noted, an unsaturated material is composed of many domains with the magnetizations of the individual domains oriented at different angles (θ - B , ϕ - A) relative to the effective internal magnetic field \vec{H}_1 . The result of Equation 4 can be extended so that it applies in unsaturated media if spatial averages which extend over several domains can be performed. Since the distributions of the magnetizations of the domains as functions of ϕ and θ and of the \vec{H}_1 's as functions of B and A are not always known, the averaging cannot, in general, be carried out explicitly. However, observing that, in most cases of practical interest, there exists a physically preferred direction for the magnetization and the effective static magnetic field often permits the averaging with respect to angles in the plane perpendicular to the preferred direction to be performed explicitly. The physically preferred direction of magnetization may arise in various ways. For instance, if we apply even a very small dc bias field to the sample, a preferred direction of magnetization is established in the direction of the applied field. Alternatively, if we arrange the ferrite so that it forms a closed magnetic path, such as the toroids in the latching phase shifters, the geometry of the sample establishes preferred magnetization directions. Assume, then, that the preferred magnetization direction is the $+z$ direction and that this is also the preferred direction for the \vec{H}_1 's. For this

situation, all values of ϕ and of A between 0 and 2π are equally likely. If it is assumed that $|\vec{M}_n|$ and $|\vec{H}_1|$ have the same value for all of the "several domains" over which the spatial averaging is to be performed and that the angles between the \vec{H}_1 's and the z-axis are small, the tensor permeability of Equation 3 after averaging with respect to ϕ and A becomes

$$\langle \vec{\mu} \rangle_{\phi, A} = \mu_0 \begin{bmatrix} \langle \mu_{11} \rangle_{\phi, A} & \langle \mu_{12} \rangle_{\phi, A} & 0 \\ \langle \mu_{21} \rangle_{\phi, A} & \langle \mu_{22} \rangle_{\phi, A} & 0 \\ 0 & 0 & \langle \mu_{33} \rangle_{\phi, A} \end{bmatrix} \quad (5)$$

$$\langle \mu_{11} \rangle_{\phi, A} = \langle \mu_{22} \rangle_{\phi, A} = 1 + \frac{\gamma_e |\vec{M}_n| |\gamma_e |\vec{H}_1| \cos \theta + j \omega \alpha (\cos^2 \theta + \frac{1}{2} \sin^2 \theta)}{\Delta} \quad (6)$$

$$\langle \mu_{12} \rangle_{\phi, A} = -\langle \mu_{21} \rangle_{\phi, A} = \frac{-j \gamma_e |\vec{M}_n| \left[\omega \cos \theta + j \frac{\alpha \gamma_e |\vec{H}_1| \sin^2 \theta}{2} \right]}{\Delta}$$

$$\langle \mu_{33} \rangle_{\phi, A} = 1 + \frac{j \omega \alpha \sin^2 \theta}{\Delta}$$

$$\langle \mu_{13} \rangle_{\phi, A} = \langle \mu_{31} \rangle_{\phi, A} = \langle \mu_{23} \rangle_{\phi, A} = \langle \mu_{32} \rangle_{\phi, A} = 0$$

$$\text{where } \Delta = \left[(\gamma_e |\vec{H}_1|)^2 - \omega^2 - (\omega \alpha)^2 \right] + j \left[2 \gamma_e |\vec{H}_1| \omega \alpha \cos \theta \right]$$

It is now convenient to change notation and write

$$\begin{aligned} \langle \mu \rangle_{\phi, A} &= \langle \mu_{11} \rangle_{\phi, A} = \langle \mu_{22} \rangle_{\phi, A} \\ -j \langle k \rangle_{\phi, A} &= \langle \mu_{12} \rangle_{\phi, A} = -\langle \mu_{21} \rangle_{\phi, A} \\ \langle \mu_z \rangle_{\phi, A} &= \langle \mu_{33} \rangle_{\phi, A} \end{aligned}$$

Separating $\langle \mu \rangle_{\phi, A}$, $\langle \kappa \rangle_{\phi, A}$, and $\langle \mu_z \rangle_{\phi, A}$ into real and imaginary parts yields after some simplifying algebra

$$\langle \mu' \rangle_{\phi, A} = 1 + \frac{\gamma_e |\vec{M}_s| \gamma_e |\vec{H}_1| \cos \theta \left[\gamma_e |\vec{H}_1| \right]^2 - \omega^2 - (\omega \alpha)^2 \cos^2 \theta}{\Delta} \quad (7)$$

$$\langle \mu'' \rangle_{\phi, A} = \frac{\gamma_e |\vec{M}_s| \omega \alpha \cos^2 \theta \left[\frac{3}{2} (\gamma_e |\vec{H}_1|)^2 + \frac{1}{2} \omega^2 + \frac{1}{2} (\omega \alpha)^2 \right]}{\Delta} - \frac{1}{2} \left[(\gamma_e |\vec{H}_1|)^2 - \omega^2 - (\omega \alpha)^2 \right]$$

$$\langle \kappa' \rangle_{\phi, A} = \frac{\gamma_e |\vec{M}_s| \omega \cos \theta \left[(\gamma_e |\vec{H}_1|)^2 \alpha^2 \sin^2 \theta + \left[(\gamma_e |\vec{H}_1|)^2 - \omega^2 - (\omega \alpha)^2 \right] \right]}{\Delta}$$

$$\langle \kappa'' \rangle_{\phi, A} = \frac{\gamma_e |\vec{M}_s| \omega \alpha \gamma_e |\vec{H}_1| \left[2\omega - \frac{\sin^2 \theta}{\omega} \left[\frac{1}{2} (\gamma_e |\vec{H}_1|)^2 + \frac{3}{2} \omega^2 - \frac{1}{2} (\omega \alpha)^2 \right] \right]}{\Delta}$$

$$\langle \mu_z' \rangle_{\phi, A} = 1 + \frac{\gamma_e |\vec{M}_s| \left[(\omega \alpha)^2 (\gamma_e |\vec{H}_1|) (2 \sin^2 \theta \cos \theta) \right]}{\Delta}$$

$$\langle \mu_z'' \rangle_{\phi, A} = \frac{\gamma_e |\vec{M}_s| \left[\omega \alpha \sin^2 \theta \left[\omega^2 + (\omega \alpha)^2 - (\gamma_e |\vec{H}_1|)^2 \right] \right]}{\Delta}$$

$$\text{where } \Delta = \left[(\gamma_e |\vec{H}_1|)^2 - \omega^2 - (\omega \alpha)^2 \right]^2 + \left[2 \gamma_e |\vec{H}_1| \omega \alpha \cos \theta \right]^2$$

If the angle between \vec{H}_1 and the z-axis is large, the expressions for the components of the permeability tensor are somewhat more complicated. In this more general situation the permeability components, after averaging with respect to angles in the xy-plane, are functions of both θ and B. To perform the averages

with respect to θ and B , it is necessary to know the distribution of these angles as functions of the other parameters of the problem (e. g. , as a function of the applied bias field).

For the case in which the angle between \vec{H}_1 and the z -axis is small, the permeability components, as given in Equation 7, are functions of θ alone. Even in this case, the average with respect to θ cannot be performed explicitly without making specific assumptions about the distributions of θ as a function of the applied bias field. However, because the average with respect to θ is intimately related to measurable physical quantities, a very useful form of the permeability tensor for unsaturated media can be obtained as follows. Write the average of the permeability components given in Equation 7 with the operator $\langle \rangle_\theta$ denoting spatial average with respect to θ . Collecting terms and recognizing their physical significance leads to the desired permeability components. Writing out the average with respect to θ , the following expressions are obtained

$$\begin{aligned}
 \langle \mu' \rangle_{\phi, A, \theta} &= 1 + \frac{1}{\Delta} \left\{ \gamma_e |\vec{H}_1| \left[(\gamma_e |\vec{H}_1|)^2 - \omega^2 \right] \gamma_e |\vec{M}_s| \langle \cos \theta \rangle_\theta \right. \\
 &\quad \left. + \gamma_e |\vec{H}_1| (\omega \alpha)^2 \gamma_e |\vec{M}_s| \langle \cos^3 \theta \rangle_\theta \right\} \\
 \langle \mu'' \rangle_{\phi, A, \theta} &= \frac{\omega \alpha}{\Delta} \left\{ \left[\frac{3}{2} (\gamma_e |\vec{H}_1|)^2 + \frac{1}{2} \omega^2 + \frac{1}{2} (\omega \alpha)^2 \right] \gamma_e |\vec{M}_s| \langle \cos^2 \theta \rangle_\theta \right. \\
 &\quad \left. - \frac{\gamma_e |\vec{M}_s|}{2} \left[(\gamma_e |\vec{H}_1|)^2 - \omega^2 - (\omega \alpha)^2 \right] \right\} \\
 \langle \kappa' \rangle_{\phi, A, \theta} &= \frac{1}{\Delta} \left\{ (\gamma_e |\vec{H}_1|)^2 \alpha^2 \gamma_e |\vec{M}_s| (\langle \cos \theta \rangle_\theta - \langle \cos^3 \theta \rangle_\theta) \right. \\
 &\quad \left. + \left[(\gamma_e |\vec{H}_1|)^2 - \omega^2 - (\omega \alpha)^2 \right] \gamma_e |\vec{M}_s| \langle \cos \theta \rangle_\theta \right\}
 \end{aligned} \tag{8}$$

$$\begin{aligned}\langle \kappa'' \rangle_{\phi, A, \theta} &= \frac{\omega \alpha \gamma_e |\vec{H}_1|}{\Delta} \left[2 \omega \gamma_e |\vec{M}_s| - \frac{1}{\omega} \left[\frac{1}{2} (\gamma_e |\vec{H}_1|)^2 + \frac{3}{2} \omega^2 \right. \right. \\ &\quad \left. \left. - \frac{1}{2} (\omega \alpha)^2 \right] \gamma_e |\vec{M}_s| (1 - \langle \cos^2 \theta \rangle_\theta) \right] \\ \langle \mu_z' \rangle_{\phi, A, \theta} &= 1 + \frac{1}{\Delta} \left[(\omega \alpha)^2 (\gamma_e |\vec{H}_1|) (2 \gamma_e |\vec{M}_s|) (\langle \cos \theta \rangle_\theta - \langle \cos^3 \theta \rangle_\theta) \right] \\ \langle \mu_z'' \rangle_{\phi, A, \theta} &= \frac{\omega \alpha}{\Delta} \left[\left| \omega^2 + (\omega \alpha)^2 - (\gamma_e |\vec{H}_1|)^2 \right| \gamma_e |\vec{M}_s| \right] \left[1 - \langle \cos^2 \theta \rangle_\theta \right]\end{aligned}$$

Where it has been recognized that the second term of Δ is very small compared to the first term for parameter values corresponding to the normal operating range of phase shifters so that $\Delta \approx \left[-\omega^2 + (\gamma_e |\vec{H}_1|)^2 - (\omega \alpha)^2 \right]^2$.

In the permeability components of Equation 8, terms of the form $|\vec{M}_s| \langle \cos \theta \rangle_\theta$, $|\vec{M}_s| \langle \cos^2 \theta \rangle_\theta$, and $|\vec{M}_s| \langle \cos^3 \theta \rangle_\theta$ are observed to occur. The first term, $|\vec{M}_s| \langle \cos \theta \rangle_\theta$, is physically just the remanent magnetization, M_r , in the z-direction. The second and third terms can be related to the remanence ratio, R_r , which is defined by

$R_r = \frac{M_r}{|\vec{M}_s|} = \langle \cos \theta \rangle_\theta$. If M_r is to be greater than zero, the distribution of the magnetizations of the domains with respect to θ must be "peaked" in the first quadrant so that $\langle \cos \theta \rangle_\theta > 0$. If this is true, it is easily shown that

$$|\vec{M}_s| \langle \cos^2 \theta \rangle_\theta \geq |\vec{M}_s| \left[\langle \cos \theta \rangle_\theta \right]^2 = |\vec{M}_s| R_r^2$$

and

$$|\vec{M}_s| \langle \cos^3 \theta \rangle_\theta \leq |\vec{M}_s| \langle \cos \theta \rangle_\theta = |\vec{M}_s| R_r$$

The saturation magnetization $|\vec{M}_s|$ and the remanent magnetization can be measured by independent methods. The damping constant α (or ΔH) can be determined from other measurements. The quantities $\langle \cos^2 \theta \rangle_\theta$ and $\langle \cos^3 \theta \rangle_\theta$ can be approximated by R_r^2 and R_r^3 , respectively, where R_r

is the measured ratio of remanence magnetization to saturation magnetization.

Since ω the microwave radian frequency, will be known, this leaves only $|\vec{H}_1|$ as an unknown factor in Equation 8. $|\vec{H}_1|$ can often be estimated by using Kittels equation to compute an effective field for an "average" or "major" domain. The demagnetizing factors for the "average" domain can often be estimated from the geometry of the sample.

It is significant that the real and imaginary parts of the permeability components depend in different ways upon $\langle \cos \theta \rangle_\theta$, $\langle \cos^2 \theta \rangle_\theta$, and $\langle \cos^3 \theta \rangle_\theta$.

The following special case vividly displays these differences. Suppose that $|\vec{H}_1| = 0$ in Equation 8. The permeability components then become

$$\langle \mu' \rangle_{\phi, A, \theta} \approx 1$$

$$\langle \kappa' \rangle_{\phi, A, \theta} \approx \frac{-\omega \gamma_e |\vec{M}_s| \langle \cos \theta \rangle_\theta}{[\omega^2 + (\omega \alpha)^2]}$$

$$\langle \mu_z' \rangle_{\phi, A, \theta} \approx 1$$

$$\langle \mu'' \rangle_{\phi, A, \theta} \approx \frac{\omega \alpha \left[\frac{\gamma_e |\vec{M}_s|}{2} (1 + \langle \cos^2 \theta \rangle_\theta) \right]}{[\omega^2 + (\omega \alpha)^2]}$$

$$\langle \kappa'' \rangle_{\phi, A, \theta} \approx 0$$

$$\langle \mu_z'' \rangle_{\phi, A, \theta} \approx \frac{\omega \alpha \gamma_e |\vec{M}_s|}{[\omega^2 + (\omega \alpha)^2]} (1 - \langle \cos^2 \theta \rangle_\theta)$$

where

$$|\vec{M}_s| \langle \cos \theta \rangle_\theta = \text{remanent magnetization} = M_r$$

$$\langle \cos \theta \rangle_\theta = \text{remanent ratio} = R_r$$

$$\text{Then } \frac{1}{2} |\vec{M}_s| \langle 1 + \cos^2 \theta \rangle_\theta = \frac{1}{2} |\vec{M}_s| \{ 1 + \langle \cos^2 \theta \rangle_\theta \}$$

$$\geq \frac{1}{2} |\vec{M}_s| \left(1 + [\langle \cos \theta \rangle_\theta]^2 \right).$$

Therefore, $\frac{1}{2} |\vec{M}_s| \langle 1 + \cos^2 \theta \rangle_\theta \stackrel{d}{=} M_{L_{xy}} \geq \frac{1}{2} |\vec{M}_s| (1 + R_r^2)$.

Similarly, $|\vec{M}_s| \langle 1 - \cos^2 \theta \rangle_\theta = |\vec{M}_s| \{1 - \langle \cos^2 \theta \rangle\}$
 $\leq |\vec{M}_s| \left(1 - \left[\langle \cos \theta \rangle_\theta\right]^2\right)$ or $|\vec{M}_s| \langle 1 - \cos^2 \theta \rangle_\theta \stackrel{d}{=} M_{L_z}$
 $\leq |\vec{M}_s| (1 - R_r^2)$. Thus the magnetization enters the real and imaginary parts of the permeability components in different manners. The appropriate effective magnetization to use in the real (phase shift) part is the remanent magnetization, M_r , while the proper effective magnetization to use in the imaginary (loss) parts is $M_{L_{xy}}$ for the xy-components and M_{L_z} for the z-component. The bounds on the M_L 's are

$$\frac{1}{2} |\vec{M}_s| (1 + R_r^2) \leq M_{L_{xy}} \leq |\vec{M}_s|$$

$$0 \leq M_{L_z} \leq |\vec{M}_s| (1 - R_r^2)$$

The magnetic losses represented by the imaginary parts of the permeability components of Equation 8 physically represent the spatial averages of losses due to damping of the precessional motion of the magnetization within the individual domains. The effective static magnetic field H_i is to be interpreted as an effective internal field which includes anisotropy and demagnetizing effects. With this interpretation, the high-frequency portion of the "low-field" losses⁹ are accounted for directly by the model. The model does not include domain-wall losses. However, in high-density, unstressed ferrites domain-wall losses are usually confined to the frequency region below 100 Mc¹⁰ and will, therefore, not be important in predicting losses at microwave frequencies.

⁹ Ibid, P46

¹⁰ Ibid, P541

The mathematical model, which has been described above, for the properties of remanent state or partially magnetized ferrites has been utilized in the solution of the boundary value problems for several FDPS configurations. The results of these computations, together with comparison with experimental data, are given in Section 4.5. Very good correlation of experimental and analytical results is obtained leading to considerable confidence in the above model.

3.2.2 High Power Characteristics of Partially Magnetized Ferrites

Performance characteristics of ferrite phase shifters normally deteriorate as either the rf average power or peak power level is increased to high values. Degradation of performance characteristics at high average power levels is due primarily to heating effects and may be controlled to some extent by designing the device structures to promote efficient removal of heat from the ferrite and/or utilizing ferrites having temperature stable properties.

As the peak rf input power to a ferrite device is increased, a threshold power level will be reached beyond which the insertion loss will increase appreciably due to inherent nonlinearities of the system of precessing dipole moments. The peak power capacity of FDPS depends both on the intrinsic threshold or critical field (h_{crit}) of the ferrite and on the dimensional and electromagnetic parameters of the device structure through their influence on the actual rf magnetic field intensity that will exist in the ferrite for a given input power level. The nonlinear or high power effects in saturated ferrites has been reasonably well explained in terms of spinwave interactions.¹¹ There has, however, been some question as to the role of spinwave interactions in nonlinear phenomena in remanent state materials.

The domain model, which was used in Section 3.2.1 to obtain a mathematical representation of the low power properties of partially magnetized materials, offers a means by which high power phenomena in remanent state materials can be interpreted in terms of the theory developed for saturated materials. A partially magnetized ferrite sample, such as the "latched" toroid in a FDPS, is made up of a number of domains of various shapes, sizes, and orientations. The magnetic moments within each domain are all, of course, aligned (i.e., a domain is, by definition, a saturated region). When an rf field is applied to a partially magnetized sample, the magnetic

¹¹ Ibid, page 206

004002

004002

moments of each domain "see" an effective field determined by magnetocrystalline anisotropy and the rf demagnetizing factors of the domain. Each saturated region of domain may thus experience an effective bias field different from that of all other domains. The rf magnetic field intensity (h_{crit}), for which the precession of the magnetic spin system first becomes unstable, is a function of intrinsic ferrite properties (saturation magnetization, spinwave linewidth, etc.), operating frequency (ω) and the effective internal bias field (H_1). When the maximum rf magnetic field intensity in a domain exceeds h_{crit} for that domain, the spin system becomes unstable and nonlinear effects contribute to the losses. Therefore, for a given ferrite at a specified frequency, the domain or domains biased most unfavorably will go unstable first.

From the nonlinear theory for saturated samples, it is well known that high power effects in ferrites arise from the unstable buildup of oscillations of pairs of spinwaves whose frequencies are either degenerate with the microwave signal frequency or equal to one-half the operating frequency. The half-frequency spinwaves are more closely coupled to the uniform precession of the magnetization than are the degenerate spinwaves. Thus, the diversion of energy from the uniform precession to half-frequency spinwaves is known as a first order process, while the coupling to degenerate spinwaves is referred to as second order.

The second order nonlinear process, when it takes place, results in a saturation of the main resonance absorption line. The minimum threshold field for the second order process occurs when the material is biased to resonance. For lower or higher bias fields, the threshold field for this process is quite high.

The first order nonlinear process may occur when the material is biased to resonance, or it may be observed as an anomalous absorption at bias field values below that required for resonance. Effective bias field values in the remanent state toroids used in FDPS are normally well below the field required for resonance. For this case, the threshold field for the first order process is appreciably lower than that for the second order process. Therefore, the first order process, in which energy is transferred from the uniform precession to half-frequency spinwaves, is the nonlinear process that limits the high peak power performance of digital phase shifters.

Since the occurrence of the first order nonlinear process depends upon the availability of half-frequency spinwaves, considerable insight into the magnitude of the threshold field h_{crit} can be obtained from an examination of the spinwave dispersion relationship. Figure 4 illustrates the spinwave dispersion curve in traditional manner. The abscissa is the spinwave number, $k = 2\pi/\lambda$, where λ is the spinwave wavelength. The ordinate is frequency. The upper curve is for spinwaves propagating perpendicular to the magnetization and the lower curve for spin waves propagating parallel to the static magnetization. The position of the spinwave manifold relative to the microwave signal frequency ω can be adjusted by varying the saturation magnetization of the ferrite or its effective bias field. If the position of the spinwave manifold is such that $\omega/2$ is greater than ω_b , then half-frequency spinwave states are available and the first order process will take place at sufficiently high power levels. If the spin wave manifold is positioned such that $\omega/2$ is less than ω_b , half-frequency spinwaves are not available* and the first order process is forbidden. In remanent state toroids $\omega/2$ is normally greater than ω_b , and the first order process is allowed. The damping of the

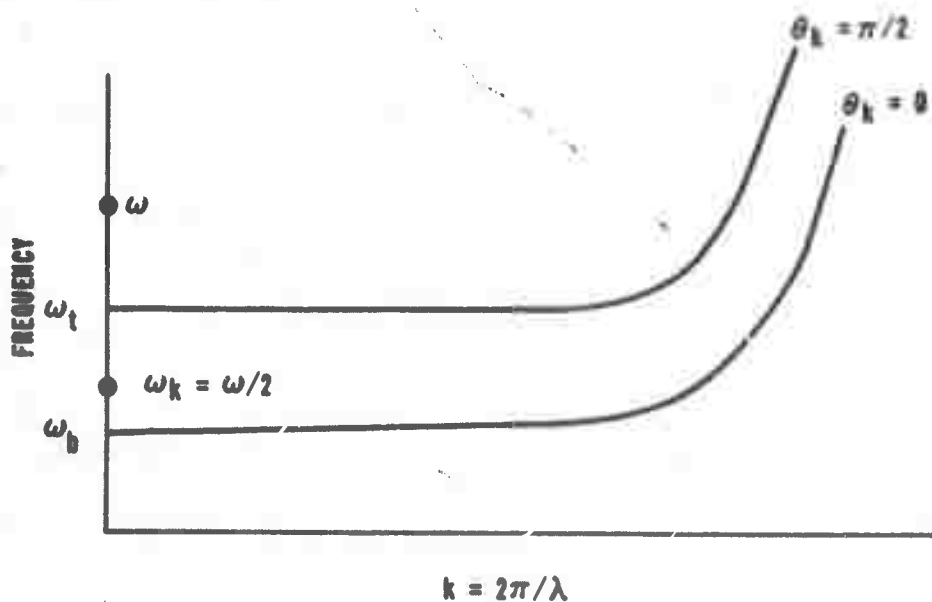


Figure 4. Conventional Spinwave Manifold Showing the Dependence of Availability Spinwave Numbers (k) on Operating Frequency (ω)

* There are, however, discrete "Walker" modes¹⁰ with very low k numbers which have frequencies somewhat less than ω_b .

uniform precession by the various spinwaves depends upon the wave number k of the spinwaves to which energy is being transformed. Thus, the spinwave linewidth is a function of k .

It appears that the dependence of ΔH_k on k is $\Delta H_k^* = A + B k^2$ where A and B are intrinsic material parameters.¹² The parameter A is the spinwave linewidth for $k = 0$ modes. The magnitude of A depends heavily upon material composition. For polycrystalline YIG, A is of the order of five oersteds. Materials doped with fast relaxing ions, such as the rare earths Dy, Ho, Yb, etc., have much larger A 's. Four percent Dy doped YIG for example, has an A value of about 150 oersteds. The $B k^2$ term in the ΔH_k expression does not appear to depend upon composition. That is, $B k^2$ for YIG seems to be about the same as $B k^2$ for a heavily rare earth doped material. Therefore, the $B k^2$ factor is much more important in determining the magnitude of ΔH_k for materials such as YIG than for rare earth doped materials. In fact, for heavy rare earth doping, A may well be so large that it "swamps" the $B k^2$ term to such an extent that ΔH_k appears to be independent of k .

The first order nonlinear process can occur both for the normal pumping arrangement in which the rf magnetic field lies in a plane perpendicular to the direction of the static magnetization and for the parallel pumping scheme in which the rf magnetic field is parallel to the static magnetization direction. Perpendicular and parallel pumping occurs simultaneously in the usual internal toroid FDPS. The threshold fields for normal and parallel pumping are somewhat different, but both are directly proportional to the spinwave linewidth ΔH_k and inversely proportional to the ratio of the saturation magnetization and frequency ω_m/ω , i.e.

$$h_{\text{crit}} = \left[\Delta H_k / (\omega_m / \omega) \right] \left[F(H_1, \theta_k) \right] \quad (9)$$

where $\omega_m = \gamma 4\pi M_s$ and $F(H_1, \theta_k)$ is a function of bias field H_1 and spinwave propagation direction θ_k as appropriate for the pumping arrangement under consideration. Direct control of h_{crit} for both normal and parallel pumping at a given frequency can thus be obtained by variation of ΔH_k (such as by rare earth doping of garnets) or by variation

¹² E. Scholomann, J. J. Green, U. Milano, JAP, Supp. To Vol 31. No. 5, May 1960, P3685.

* Recent data by Comstock (J. Appl. Phys., January 1965) indicates that this k dependence may be more nearly $\Delta H_k = Fk$, but in either event the arguments presented would hold.

of ω_m/ω (for example, by aluminum doping of garnets). The damping of the various spinwaves depends upon their wave numbers k with the shorter wavelength modes being more heavily damped.

A very dramatic and abrupt change in the threshold field for both normal and parallel pumping occurs when the spinwave manifold is positioned so that $\omega_k = \omega/2$ is greater than ω_t . In this situation the only half-frequency spinwaves available are those with very large k values. Thus, since $\Delta H_k = A + Bk^2$, ΔH_k , and hence h_{crit} , increases abruptly as low k half-frequency spinwaves become unavailable. This effect will be most marked for materials having low A values (e.g., pure YIG) and will be less important as rare earth doping is increased to provide very large values of $\Delta H_k \Big|_{k=0}$.

From the above discussion some interesting observations can be made about the values to be expected from measurements of the apparent critical field, h_{crit} for FDPS. A variety of domains, each having a different effective bias field, exist in a remanent state toroid (or any other partially magnetized sample). The measurement of the high power threshold for a phase shifter consists simply of detecting the rf peak power level at which the device insertion loss first increases from its low power level. This effect will take place at the power level for which the precession of the magnetic moments in the most unfavorably biased domain first goes unstable. To obtain higher threshold powers in FDPS, it is therefore necessary to increase the threshold field of the most unfavorable domains. Doping with rare earths accomplishes this feat by increasing the ΔH_k of all domains, including the most unfavorable, and the observed threshold power level naturally increases. Decreasing ω_m/ω likewise increases the h_{crit} of each domain somewhat. As ω_m/ω is decreased, the effective bias field (arising from demagnetization effects) for each domain also decreases. The most dramatic influence on the threshold field from variation in ω_m/ω occurs when ω_m/ω is decreased to the point where the effective bias field of every domain is such that there are no low k , $\omega/2$ spinwaves available, i.e., where the relative position of the spinwave manifold is such that $\omega/2 > \omega_t$. At this value of ω_m/ω a very abrupt increase in h_{crit} occurs. The value of ω_m/ω for which all domains are biased so that $\omega/2 > \omega_t$ can be estimated as follows.

The most unfavorable biasing of a domain that is possible, occurs for the Polder-Smit (anti-parallel) domains. For these domains H_i is approximately $\left(4/3 \frac{K_1}{M_s} + 4\pi M_s\right)$, or if $\frac{K_1}{M_s}$ is negligible with respect to $4\pi M_s$, then $H_i \approx 4\pi M_s$.

Inserting this value of H_i into the equation for the upper frequency limit of the spinwave manifold and equating that frequency to $\omega/2$, it is easily shown that when $\omega_m/\omega > 0.345$, H_i is sufficiently small to guarantee that only high k , $\omega/2$ spinwave will be available.

This situation is illustrated in the normalized spinwave dispersion plot for Polder-Smit domains shown in Figure 5.

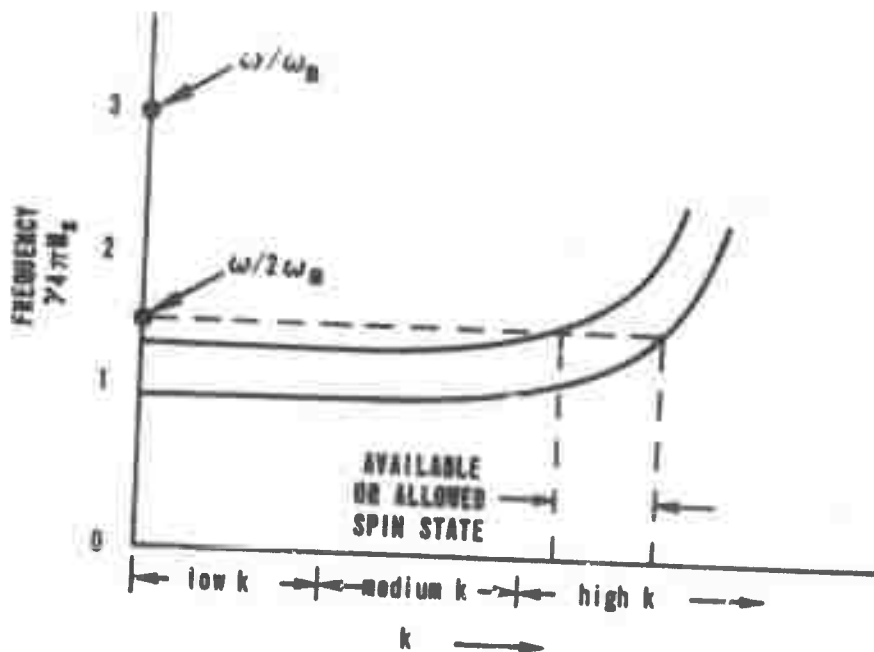


Figure 5. Normalized Spinwave Dispersion Curve Assuming $H_i = 4\pi M_s$ (Polder-Smit Domains)

Figure 6 presents a pictorial summary of the various conditions which can occur.

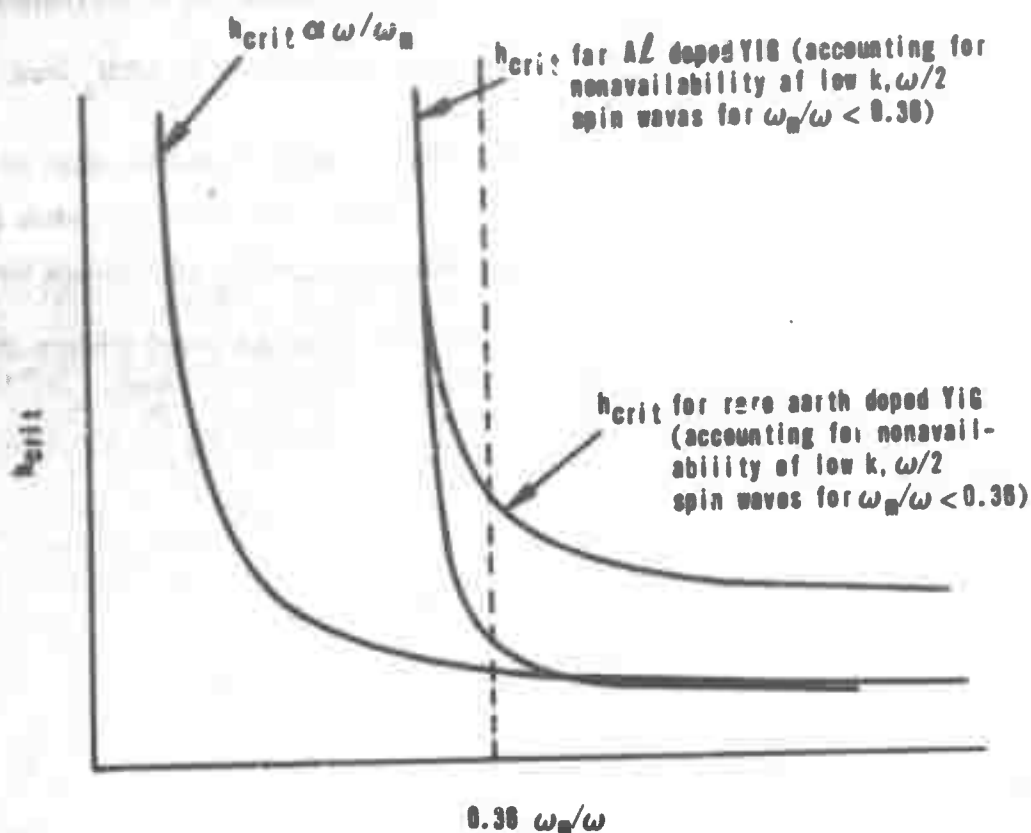


Figure 6. Threshold Field of Polder-Smit Domains as a Function of Normalized Magnetization

3.2.3 Dielectric and Geometrical Characteristics of FDPS

The macroscopic electromagnetic properties, including the effects of losses, of dielectric materials in the phase shifters are accounted for in the usual manner by a complex permittivity $\epsilon_d = \epsilon_o (\epsilon'_d - j \epsilon''_d)$ and by a permeability $\mu_d = \mu_o$ where ϵ_o and μ_o are the permittivity and permeability of free space. Similarly, the dielectric properties of the ferrite are accounted for by the complex permittivity $\epsilon_f = \epsilon_o (\epsilon'_f - j \epsilon''_f)$.

For the purpose of analysis, it is usually convenient and often necessary to consider a model which is geometrically less complicated than the physical device. As an example, refer to Figure 7 which illustrates a cross-section of the single-toroid FDPS shown in Figure 2. In the normal operational mode of this phase shifter (i.e., the fundamental TE mode), the rf magnetic field is entirely in the xy-plane. The magnetization in the top and bottom "crossbars" of the toroids is principally in the

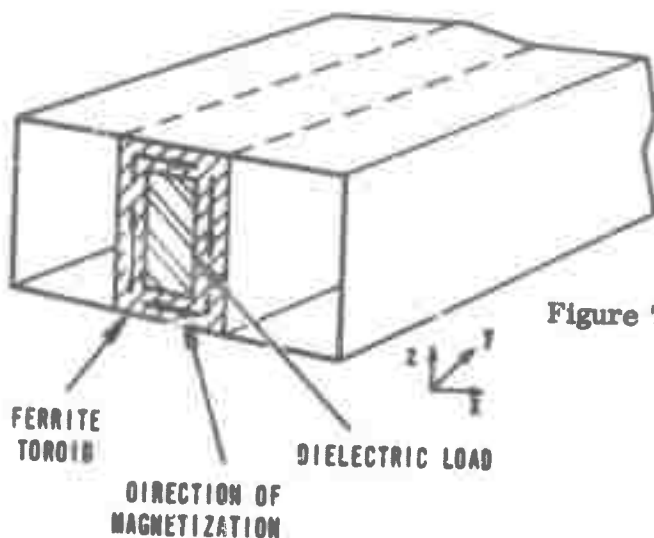


Figure 7. A Waveguide Nonreciprocal Latching Phase Shifter

$\pm x$ direction, while in the vertical legs the magnetization tends to be in the $\pm z$ direction. To first order, when the incident rf magnetic field and the direction of magnetization of a sample are mutually parallel, there is no interaction between the field and the magnetization. Therefore, the crossbars of the toroid "look" approximately like pieces of dielectric to the incident rf field. In the vertical legs the magnetization is normal to the rf magnetic field and a strong interaction takes place.

From the above observations, it is apparent that the single-toroid latching phase shifter can be represented by the twin slab model shown in Figure 8. When the dielectric core and the ferrite toroid of the practical device have the same dielectric constant, that value is, of course, used for the dielectric constant of the dielectric load of the model. If the dielectric constants of the dielectric core and the ferrite are different, an "effective" dielectric constant is used for the dielectric load of the model. Geometrical models for other configurations are obtained in a similar fashion.

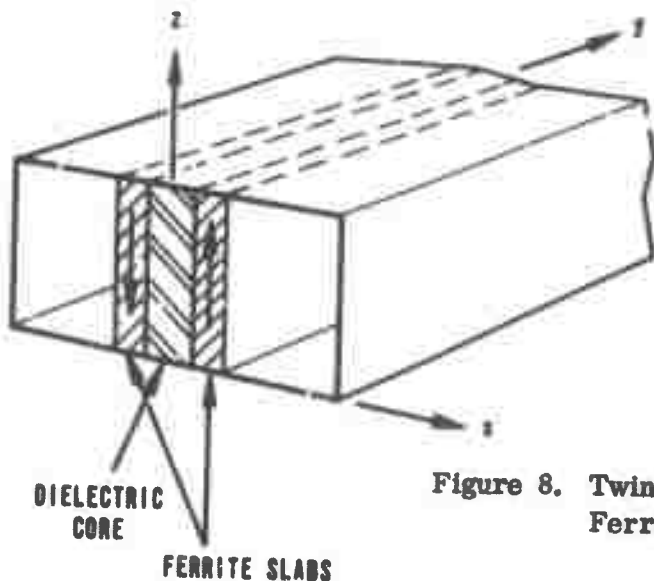


Figure 8. Twin-Slab Model for "Single-Toroid" Ferrite Latching Phase Shifter

3.3 ANALYSIS TECHNIQUES

To establish quantitative relationships between the transfer characteristics of a ferrite device and its material and dimensional parameters, it is necessary to solve the boundary value problem for the device structure. The general procedure is to solve Maxwell's equations in an appropriate coordinate system and apply the pertinent boundary conditions. The resulting equations can be manipulated to yield an equation which can be numerically solved for the propagation constant. For many transmission structures it is possible to derive the characteristic equation for the propagation constant by a simpler procedure which was suggested by Seidel¹² and is referred to as the "transverse operator" method. Seidel's procedure is closely related to the familiar ABCD matrix formulation for transmission line circuits. The transverse operator technique is based on the fact that in a TE mode waveguide where the rf field components have no variation in the direction of the E field, the electromagnetic field is completely specified by the E field and the longitudinal h component alone. For example, the electromagnetic field in the structure of Figure 9 has components E_z , h_x , and h_y but is completely specified by E_z and h_y since h_x is linearly related to h_y through the divergence condition on the induction field. Both E_z and h_y are continuous at the interfaces of the strata of the waveguide cross section. Hence, in analogy with the ABCD matrix representation of cascaded transmission lines, a transverse transfer matrix is defined which "transfer" the quantities E_z and h_y from one point along a transverse axis to another.

$$\begin{bmatrix} E_{za} \\ h_{ya} \end{bmatrix} = \begin{bmatrix} A & B \\ C & D \end{bmatrix} \begin{bmatrix} E_{zb} \\ h_{yb} \end{bmatrix} \quad (10)$$

The overall transverse operator matrix relating the fields at point a to the fields at point b is the matrix product of the transfer operators of the individual regions separating the point. If points a and b are taken to be the walls of the waveguide, then

$$E_{za} = E_{zb} = 0 \text{ and } \begin{bmatrix} 0 \\ h_{ya} \end{bmatrix} = \begin{bmatrix} A & B \\ C & D \end{bmatrix} \begin{bmatrix} 0 \\ h_{yb} \end{bmatrix} \quad (11)$$

¹²H. Seidel, "Ferrite Slabs in Transverse Electric Mode Wave Guide," J. Appl. Phys., 28, February 1957.

14002

or

$$\begin{aligned} 0 &= B h_{yb} \\ h_{ya} &= D h_{yb} \end{aligned} \quad (12)$$

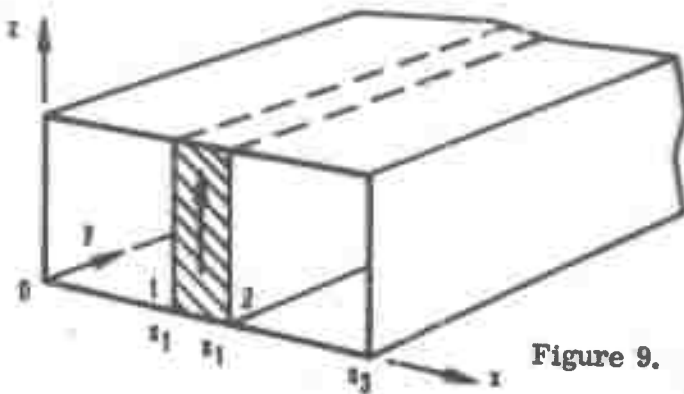


Figure 9. A Ferrite Loaded Rectangular Waveguide

For a nontrivial solution h_{yb} must be nonzero. Therefore, B must be zero. From this condition the equation for the propagation constant is easily determined. If the structure analyzed has electromagnetic symmetry about some point, for example, point o is such a point in the structure of Figure 10; the y -component of the h field must be zero about that point and a simplification in the computations is necessary to obtain the propagation equation results. The operator relating the fields at point o to those at the wall can be written as

$$\begin{bmatrix} 0 \\ h_{ya} \end{bmatrix} = \begin{bmatrix} A & B \\ C & D \end{bmatrix} \begin{bmatrix} E_{zo} \\ 0 \end{bmatrix} \quad (13)$$

or

$$\begin{aligned} 0 &= A E_{zo} \\ h_{ya} &= C E_{zo} \end{aligned} \quad (14)$$

For a nontrivial solution E_{zo} must be different from zero, and A must, therefore, be identically zero. This condition leads to the equation for the propagation constant of symmetrical structures.

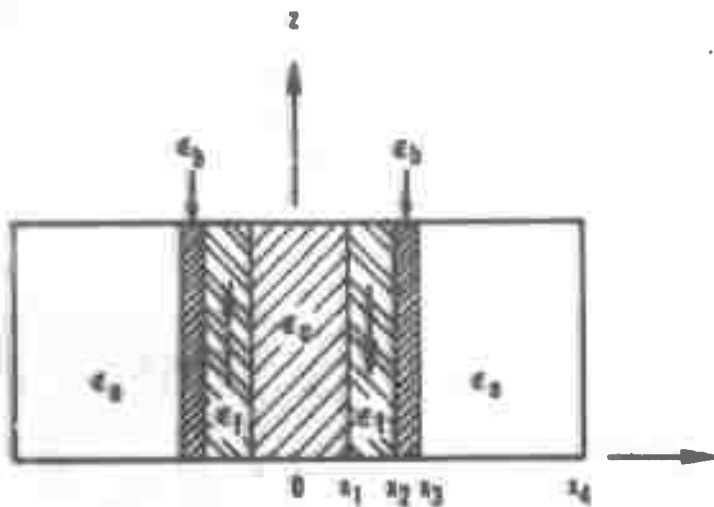


Figure 10. A Structure with Electromagnetic Symmetry about $z = 0$

The ABCD parameters for ferrite and dielectric regions are easily obtained from Maxwell's equations. The following derivation for these parameters is modeled after that of Seidel, but the notation is somewhat different.

Consider a TE mode waveguide structure such as that shown in Figure 9. The ferrite slab is of width δ and is assumed to be infinitely long in the y direction. The preferred direction for the effective internal static magnetic field H_1 and the saturation magnetization \vec{M}_s is assumed to be in the $+z$ direction. The intrinsic permeability tensor then has the general form

$$\langle \vec{\mu} \rangle_{\text{avg}} = \mu_0 \begin{bmatrix} \langle \mu \rangle_{\text{avg}} & -j \langle \kappa \rangle_{\text{avg}} & 0 \\ j \langle \kappa \rangle_{\text{avg}} & \langle \mu \rangle_{\text{avg}} & 0 \\ 0 & 0 & \langle \mu_z \rangle_{\text{avg}} \end{bmatrix} \quad (15)$$

where

$$\langle \mu \rangle_{\text{avg}} = \langle \mu' \rangle_{\text{avg}} - j \langle \mu'' \rangle_{\text{avg}}$$

$$\langle \kappa \rangle_{\text{avg}} = \langle \kappa' \rangle_{\text{avg}} - j \langle \kappa'' \rangle_{\text{avg}}$$

$$\langle \mu_z \rangle_{\text{avg}} = \langle \mu_z' \rangle_{\text{avg}} - j \langle \mu_z'' \rangle_{\text{avg}}$$

and $\langle \mu' \rangle_{\text{avg}}$, $\langle \mu'' \rangle_{\text{avg}}$, $\langle \kappa' \rangle_{\text{avg}}$, $\langle \kappa'' \rangle_{\text{avg}}$, $\langle \mu_z' \rangle_{\text{avg}}$, and $\langle \mu_z'' \rangle_{\text{avg}}$ are given by Equation 8 of Section 3.2.1.

Assume a general form for the electric field inside the ferrite, say

$$E_z = \left[B e^{jk_m x} + C e^{-jk_m x} \right] e^{-\gamma y} e^{j\omega t} \quad (16)$$

where

$$k_m^2 = \gamma^2 + \frac{\omega^2 \mu_o \epsilon_o \epsilon_f}{\rho} = \text{square of the wave number in the ferrite}$$

$$\rho = \frac{\langle \mu \rangle_{\text{avg}}}{\left[\langle \mu \rangle_{\text{avg}} \right]^2 - \left[\langle \kappa \rangle_{\text{avg}} \right]^2}$$

γ = propagation constant

The magnetic field intensity in the y direction is

$$h_y = \frac{\rho}{j\omega\mu_o} \left[\left(jk_m + \frac{\gamma}{\theta} \right) B e^{jk_m x} + \left(-jk_m + \frac{\gamma}{\theta} \right) C e^{-jk_m x} \right] e^{-\gamma y} e^{j\omega t} \quad (17)$$

where

$$\theta = \frac{-\langle \mu \rangle_{\text{avg}}}{j\langle \kappa \rangle_{\text{avg}}}$$

Using Equations 16 and 17, the fields at point one ($x = x_1$) and at point two ($x = x_1 + \delta$) can be written as

$$E_{z1} = \left[B e^{jk_m x_1} + C e^{-jk_m x_1} \right] e^{-\gamma y} e^{j\omega t} \quad (18)$$

$$E_{z2} = \left[B e^{jk_m (x_1 + \delta)} + C e^{-jk_m (x_1 + \delta)} \right] e^{-\gamma y} e^{j\omega t} \quad (19)$$

$$h_{y1} = \frac{\rho}{j\omega\mu_o} \left[\left(jk_m + \frac{\gamma}{\theta} \right) B e^{jk_m x_1} + \left(-jk_m + \frac{\gamma}{\theta} \right) C e^{-jk_m x_1} \right] e^{-\gamma y} e^{j\omega t} \quad (20)$$

$$h_{y2} = \frac{\rho}{j\omega\mu_0} \left[\left(jk_m + \frac{\gamma}{\theta} \right) B e^{jk_m(x_1 + \delta)} + \left(-jk_m + \frac{\gamma}{\theta} \right) C e^{-jk_m(x_1 + \delta)} \right] e^{-\gamma y} e^{j\omega t} \quad (21)$$

Referring to Figure 9, the electric field in the z-direction and the magnetic field in the y-direction at point one can be related to the corresponding fields at point two by the transverse operator equation

$$\begin{bmatrix} E_{z1} \\ h_{y1} \end{bmatrix} = \begin{bmatrix} A & B \\ C & D \end{bmatrix} \begin{bmatrix} E_{z2} \\ h_{y2} \end{bmatrix} \quad (22)$$

Expanding Equation 22 yields the following two equations.

$$E_{z1} = A E_{z2} + B h_{y2} \quad (23)$$

$$h_{y1} = C E_{z2} + D h_{y2} \quad (24)$$

Substituting Equations 18 through 21 into Equations 23 and 24 allows the parameters ABCD to be evaluated. These parameters for a ferrite region of width δ are

$$\begin{aligned} A &= \cos k_m \delta + \frac{\gamma}{k_m \theta} \sin k_m \delta \\ B &= \frac{-j\omega\mu_0}{\rho k_m} \sin k_m \delta \\ C &= \frac{j\rho}{\omega\mu_0 k_m} \left(\frac{-\gamma^2}{\theta} - k_m^2 \right) \sin k_m \delta \\ D &= \cos k_m \delta - \frac{\gamma}{k_m \theta} \sin k_m \delta \end{aligned} \quad (25)$$

If the internal effective static magnetic field and the magnetization reverse in direction, the only change necessary is to reverse the sign of θ .

For a dielectric region $\rho \rightarrow 1$ and $\theta \rightarrow \infty$, so that the parameters for a dielectric region of width W can be written as

$$\begin{aligned} A &= \cos k_d W \\ B &= \frac{-j \omega \mu_0}{k_d} \sin k_d W \\ C &= \frac{-j k_d}{\omega \mu_0} \sin k_d W \\ D &= \cos k_d W \end{aligned} \quad (26)$$

As an example of the application of this method, consider the structure shown in Figure 11 which is a twin-slab model of the single internal toroid FDPS. This structure has electromagnetic symmetry about o . The overall transfer matrix is

$$\begin{bmatrix} A & B \\ C & D \end{bmatrix} = \begin{bmatrix} A_1 & B_1 \\ C_1 & D_1 \end{bmatrix} \begin{bmatrix} A_2 & B_2 \\ C_2 & D_2 \end{bmatrix} \begin{bmatrix} A_3 & B_3 \\ C_3 & D_3 \end{bmatrix}$$

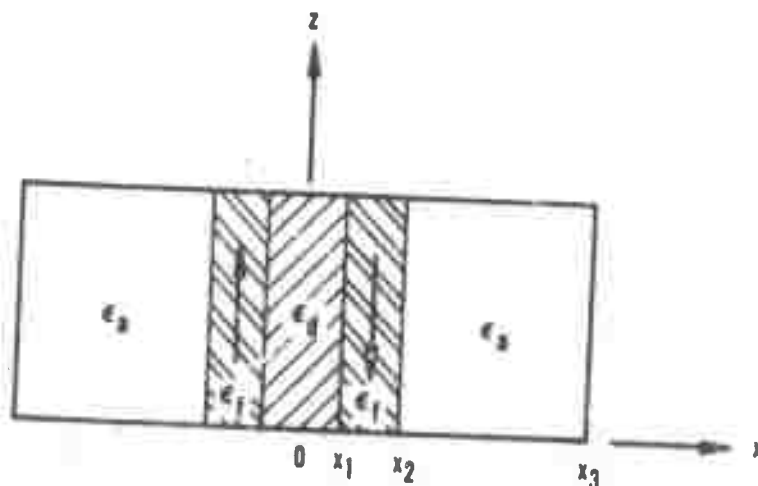


Figure 11. Dielectric Loaded Twin-Slab Structure

Carrying out this multiplication and setting $A = 0$ yields

$$A = A, (A_2 A_3 + B_2 C_3) + B, (C_2 A_3 + D_2 C_3) = 0$$

Substituting for the A's B's, C's, and D's from Equations 25 and 26, the following equation for the propagation constant is obtained

$$\begin{aligned} & \left[\frac{k_m}{\rho} (k_a - k_d) \cot k_m (x_2 - x_1) - \frac{\gamma}{\rho \theta} (k_a + k_d) \right] \cos \{k_d x_1 - k_a (x_3 - x_2)\} \\ & + \left[\frac{k_m}{\rho} (k_a + k_d) \cot k_m (x_2 - x_1) - \frac{\gamma}{\rho \theta} (k_a - k_d) \right] \cos \{k_d x_1 + k_a (x_3 - x_2)\} \\ & + \left[k_m^2 + \frac{\gamma^2}{\theta^2} - \frac{k_a k_d}{\rho^2} \right] \sin \{k_d x_1 - k_a (x_3 - x_2)\} \\ & - \left[k_m^2 + \frac{\gamma^2}{\theta^2} + \frac{k_a k_d}{\rho^2} \right] \sin \{k_d x_1 + k_a (x_3 - x_2)\} = 0 \end{aligned} \quad (27)$$

where

$$k_m^2 = \frac{\omega^2 \mu_o \epsilon_o \epsilon_f}{\rho} + \gamma^2$$

$$k_d^2 = \omega^2 \mu_o \epsilon_o \epsilon_d + \gamma^2$$

$$k_a^2 = \omega^2 \mu_o \epsilon_o \epsilon_a + \gamma^2$$

$$\rho = \frac{\mu}{u^2 - \kappa^2}$$

$$\theta = j \frac{\mu}{\kappa}$$

$$\gamma = \alpha + j\beta$$

$$\mu = \mu' - j\mu''$$

$$\kappa = \kappa' - j\kappa''$$

$$\epsilon_d = \epsilon'_d - j\epsilon''_d$$

$$\epsilon_f = \epsilon'_f - j\epsilon''_f$$

$$\epsilon_a = \epsilon'_a - j\epsilon''_a$$

If the dimensional and material parameters of the structure are specified, this equation can be solved numerically for the propagation constant γ . With γ known, the rf electric and magnetic fields are easily obtained from Maxwell's equations.

A presentation and discussion of the solutions of the propagation constant equation for a number of FDPS configurations are given in Section 4.5. Good correlation is found between experimental and calculated results, leading to considerable confidence in the mathematical models and techniques presented in the above sections.

3.4 INFLUENCE OF INTRINSIC AND CERAMIC PROPERTIES ON SQUARE LOOP CHARACTERISTICS

The relative desirability of a ferrite material for use in a digital phase shifter depends strongly on the materials' ratio of remanent magnetization to saturation magnetization, its coercive field, and time required for switching it from one remanent state to the other. In general, a "good" ferrite for digital phase shifter applications will have a high remanence ratio, a low coercive field, and a small switching time. Each of these properties is discussed below.

3.4.1 Remanence Ratio

The remanence ratio is probably the single most important square loop property as far as microwave applications of ferrite toroids is concerned. Ideally, the remanent magnetization should equal the saturation magnetization, i.e., the remanence ratio R_r should be 1.0. This ideal situation is unlikely to be attained in practice. Remanence ratios of 0.6 to 0.7 are more normally encountered.

In a polycrystalline ferrite or garnet material, the magnetization in the individual crystallites will, due to crystalline anisotropy, prefer to be aligned along the easy (111) directions of the crystallites. If magnetocrystalline anisotropy were the only factor influencing the magnetization in individual crystallites, the remanence ratio for a cubic material would be approximately 0.87. This result assumes that in the saturated state the magnetization in all crystals is parallel to the applied field and relaxes to the nearest easy direction, or body diagonal, when the field is removed. This ideal value is difficult to realize in practice because of unfavorable contributions from other anisotropies (stress anisotropy or magnetostriction) and shape anisotropy. The existence in polycrystalline materials of pores or voids, in the material also gives rise to local demagnetizing fields which will lower the resultant remanence ratio. Thus, magnetocrystalline anisotropy will tend to favor a high remanence ratio while porosity and other anisotropies tend to decrease remanence ratio. If the magnetocrystalline anisotropy is large compared to other anisotropies and demagnetizing fields arising at magnetic discontinuities in the materials, the remanence ratio can approach the theoretical limit of 0.87. Thus, highest remanence ratios will be realized in materials having low magnetostriction, low unfavorable internal stresses, and a dense, homogenous magnetic structure with a high magnetocrystalline anisotropy. The same ceramic qualities that lead to high remanence ratio also tend to lead to low resonance linewidths.

A unidirectional anisotropy favoring high remanence ratio can sometimes be built into a material by controlling its shape and internal stresses. Quenching, lattice

deformations, applied pressure, etc., are techniques sometimes used. Such techniques, however, do not seem very practical for microwave materials because of their unfavorable effects on microwave properties.

In actual device applications, most microwave materials are not driven into saturation with the available drive fields (approximately 25 oersteds maximum). The hysteresis loop on which operation is based is then not the saturated loop, but rather some minor loop. To classify and optimize materials, it is necessary to measure the absolute value of the remanent magnetization at the drive fields normally used in digital phase shifters in order that such measurements have practical meaning. It is desirable that these drive fields be as low as possible consistent with a realization of nearly maximum values of remanence ratio, R_r .

The following procedures are used to measure the remanent magnetization.

- 1) The $4\pi M_s$ of the material is measured by some independent means, such as a vibrating sample magnetometer, in applied fields of the order of 5,000 oersteds.
- 2) The hysteresis loop is measured on a hysteresograph. The drive fields used are, whenever possible, 10 times the coercive field of the material. For most materials the remanent magnetization is observed to change very little between drive fields of 8 to 10 times the coercive field of the material. From this hysteresis loop, the "squareness" and coercive field can be measured. The squareness is defined as $S_D = \frac{4\pi M_{RD}}{4\pi M_D}$, where S_D is the "squareness," $4\pi M_{RD}$ is the remanent magnetization for the drive field used and $4\pi M_D$ is the magnetization at the peak of the drive field. The measurement of $4\pi M_D$ is described below.

If the core reverses an amount of flux $\Delta\phi$ in a time Δt , the average voltage V produced during switching is

$$\langle V \rangle = N \frac{\Delta\phi}{\Delta t} \quad (28)$$

where N is the number of turns threading the core. If A is the cross-sectional area of the legs of the core and B_D is the change in flux density at the drive field used

$$\Delta\phi = A \Delta B_D \quad (29)$$

and

$$\Delta B_D = \Delta(4\pi M_D) \quad (30)$$

for the low drive fields used for toroidal geometries. Therefore

$$\Delta \phi = A \Delta (4\pi M_D) \quad (31)$$

and

$$(4\pi M_D) = -\frac{\langle V \rangle \Delta t}{AN} \quad (32)$$

Using proper integrating circuits and known values of A and N, $\Delta (4\pi M_D)$ can be measured (see Figure 12 for interpretation of $\Delta (4\pi M_D)$). It is recommended that calibration samples be used for ease in the measurement and use of $\langle V \rangle \Delta t$.

With the measured value of "squareness" and $4\pi M_D$, the $4\pi M_{RD}$ can be computed. For drive fields of eight to ten times the coercive field of the material

$$4\pi M_{RD} = 4\pi M_R \quad (33)$$

for most materials. The remanence ratio of the material is then computed as

$$R_R = \frac{4\pi M_R}{4\pi M_S} \quad (34)$$

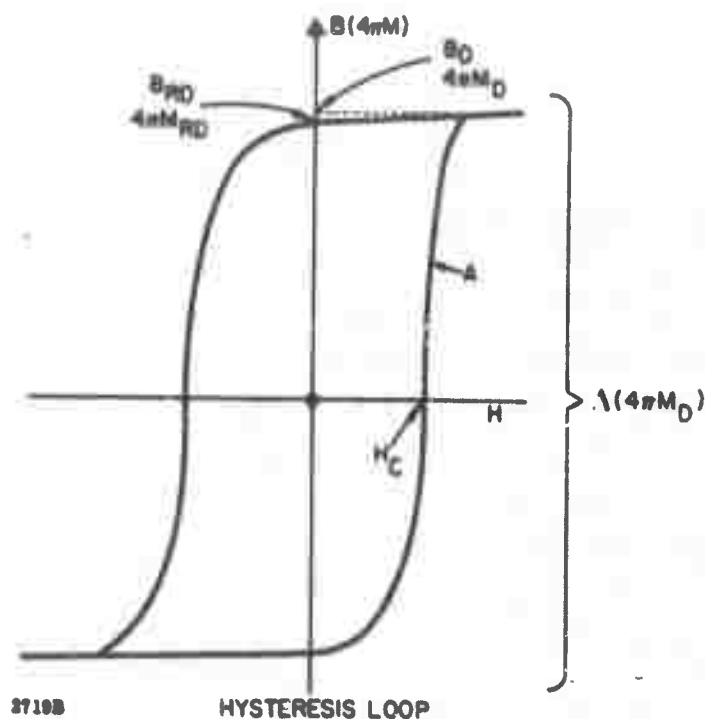


Figure 12. Hysteresis Loop of Ferrimagnetic Materials

3.4.2 Coercive Force

The coercive force of ferrite materials used in digital phase shifters is determined principally by the ease with which domain walls can move through the polycrystalline material. At the drive fields encountered in digital phase shifters, the switching action is due almost entirely to domain wall motion, and thus it is the ease with which domain walls can be nucleated and moved through the material that determines the coercive field.

The motion of a domain wall through a magnetic material is determined by a combination of both intrinsic and ceramic properties. The coercive field for domain wall motion can be described by the empirical relation

$$H_c = \frac{2 K_1 (\Delta v)}{\pi M_s} \left[0.386 + \log \sqrt{\frac{2\pi M_s^2}{K_1}} \right] \quad (35)$$

where (Δv) is the fractional volume of nonmagnetic inclusions, and H_c is the coercive field in oersteds. $\frac{2 K_1}{M_s}$ is the conventional magnetocrystalline anisotropy field. Experimental results are generally found to be in reasonable agreement with this expression.

Thus, we see that the coercive field varies directly with the anisotropy field, $\frac{2 K_1}{M_s}$, and the volume of nonmagnetic inclusions (pores, impurities, etc.). For minimum coercive field, a maximum density and a minimum anisotropy field are desirable. Clearly, optimum square loop properties (minimum H_c and maximum R_r) place conflicting demands on the magnetocrystalline anisotropy. A minimum anisotropy field is desirable for a small coercive field, while a large anisotropy field is desirable for a large remanence ratio. This set of opposing demands normally leads to an observed decrease in remanence ratio when very small coercive fields are encountered. However, coercive fields of less than one oersted are easily obtainable in combination with remanence ratios of approximately 0.7.

3.4.3 Switching Time

The switching time of a ferrite toroid is essentially the sum of the time required to nucleate a domain wall and the time required for the domain wall to propagate across the width of the toroid. The switching and dynamic behavior of ferrimagnetic oxides have been treated in detail in two summary articles on this subject. These articles are as follows:

- (1) J. B. Birks and J. Hart, Progress in Dielectrics, Volume 5, Academic Press, Inc., Publishers, New York, 1963, (H. P. Peloschek; "Square Loop Ferrites and their Applications," pp 37-93).
- (2) Harvey Rubinstein, "Switching Properties of Ferrites and Garnets," Scientific Report No. 6 (Series 2), Gordon McKay Laboratory of Applied Science, Harvard University, Cambridge, Mass. (Nov. 30, 1962) Cont. No. AF19(604)5487, AFCRL.

These articles deal with all of the possible switching mechanisms and analytical expressions which describe the behavior of flux reversal in ferrimagnetic oxides. The highlights of these articles, as they pertain particularly to switching aspects of materials used in ferrite digital phase shifters, have been discussed in considerable detail in the Final Report on RADC Contract No. AF30(602)3490.

Perhaps it can suffice here to mention that three possible mechanisms for switching are possible. One is called pure wall displacement, the second, incoherent rotations, and the third, coherent rotations. These various mechanisms have switching times which vary between the longest time for pure wall displacement and the shortest time for coherent rotations. The switching fields involved vary also, being smallest for pure wall displacement and largest for coherent rotations. In any case, the switching time can be given by the expression $t_s(H - H_0) = S$, where S is a constant for the material at a given temperature and is called the switching coefficient. $(H - H_0)$ is the effective drive field where H is the applied field and H_0 is a function of the material and approximately equal to the coercive field.

The switching coefficient of the material is expressed in oersteds-microseconds and varies with the type of switching mechanism used. The switching constants for the three different modes of flux reversal in ferrites may differ by as much as a factor of 20. That is, the switching coefficient for pure wall displacement may be 20 times the switching coefficient for coherent rotations. In view of the drive fields normally used in FDPS, however, the domain wall motion mechanism is the principal switching mechanism operative, and its switching constant is the one to be considered in calculations of switching time. This switching coefficient for domain wall motion can be shown to be given by

$$S_w = \frac{6.4 d \lambda \times 10^{-2}}{\delta g^2 M_s} = \frac{\beta d}{2M_s} \quad (36)$$

where d = distance moved by domain wall

$$\beta = \frac{17.8 \lambda \times 10^{-2}}{\delta^2}$$

$$\delta = \text{domain wall thickness} = \sqrt{\frac{kT_c}{K_1^2}}$$

k = Boltzman's constant,

$$\lambda = \text{intrinsic damping parameter} = \frac{\gamma M_s \Delta H}{2H_r}$$

ΔH = intrinsic linewidth

H_r = field (oe) required for ferrimagnetic resonance at the linewidth measurement frequency.

Typical switching constants S_w for domain wall motion are of the order of 0.1 to 1 oersted microseconds. Thus, for a drive field of approximately 5 times the coercive field, we find that the switching time, t_s , is of the order of 0.02 to 0.2 microseconds. These switching times are sufficiently rapid for most microwave applications so that other flux reversal processes involving domain rotation need not be considered. The application of flux reversal processes would lead to very high drive field requirements which would be intolerable for most phased array applications.

U 4002

4 SUMMARY AND DISCUSSION OF RESULTS

4.1 INTRODUCTION

This section presents and discusses currently available results of the analytical and experimental work carried out to determine the effect of intrinsic ferrite parameters on the performance characteristics of FDPS. The overall goal of this work is to develop theoretical and experimental techniques which will permit the pin-point specification of the intrinsic material parameter values required to obtain optimum FDPS performance characteristics under a specified set of constraints (i. e. , constraints such as average and peak power handling requirements, permissible insertion loss, stability of phase and loss with temperature, etc.).

Physical and mathematical models for remanent state ferrites were presented in Section 3. These models were developed to enable the prediction and evaluation of the performance characteristics of ferrites in different frequency bands and with different geometries without having to resort to an actual measurement of loss and phase shift for each frequency and geometry employed. Moreover, the models permit the prediction and evaluation of the effects of variations in intrinsic material parameters on loss, phase shift, and high power threshold. In attempting to verify the material models proposed, a computer-aided analysis has been carried out to find the exact solutions to the boundary value problems for various device configurations. Differential phase shift, insertion loss, and rf field intensities for each configuration are obtained from the solution to its boundary value problem. This analysis has been supported and guided by an extensive set of experimental measurements on a variety of FDPS configurations and a wide array of material parameters. The combined theoretical and experimental effort has been aimed towards substantiating and improving the physical model proposed for remanent state ferrites, so that a more complete understanding of the operation and limitations on FDPS could be obtained.

4.2 MEASUREMENT EQUIPMENT AND TECHNIQUES

Equipment and techniques are described for performing measurements of the following material parameters: density, saturation magnetization, g-factor, linewidth, Curie temperature, dielectric constant, dielectric loss tangent, remanence ratio, and coercive field. In addition, equipment and techniques for measuring device phase shift, insertion loss, VSWR, high power threshold, switching time, and switching energy are described.

4.2.1 Measurement of Material Properties

(a) Measurement of $4\pi M_s$. The measurement of $4\pi M_s$ was made with the vibrating sample magnetometer shown in Figure 13. This measurement is based on the detection of the ac magnetic field set up by the vibrating magnetic sample. A small sphere of the unknown material is placed in a strong saturating dc magnetic field. The sample is vibrated at a low audio frequency (100 cps) and the oscillating dipole field thus generated is detected by two coils so positioned as to minimize stray pickup. The magnitude of this dipole field is compared to the signal detected by two similar coils from a known calibrated sample attached to the same vibrating rod. This system, first proposed by Foner,¹⁴ is capable of accurate, continuous readout and lends itself well to the measurement of saturation magnetization as a function of temperature. The magnetometer can also be used to measure coercive force on spherical samples.

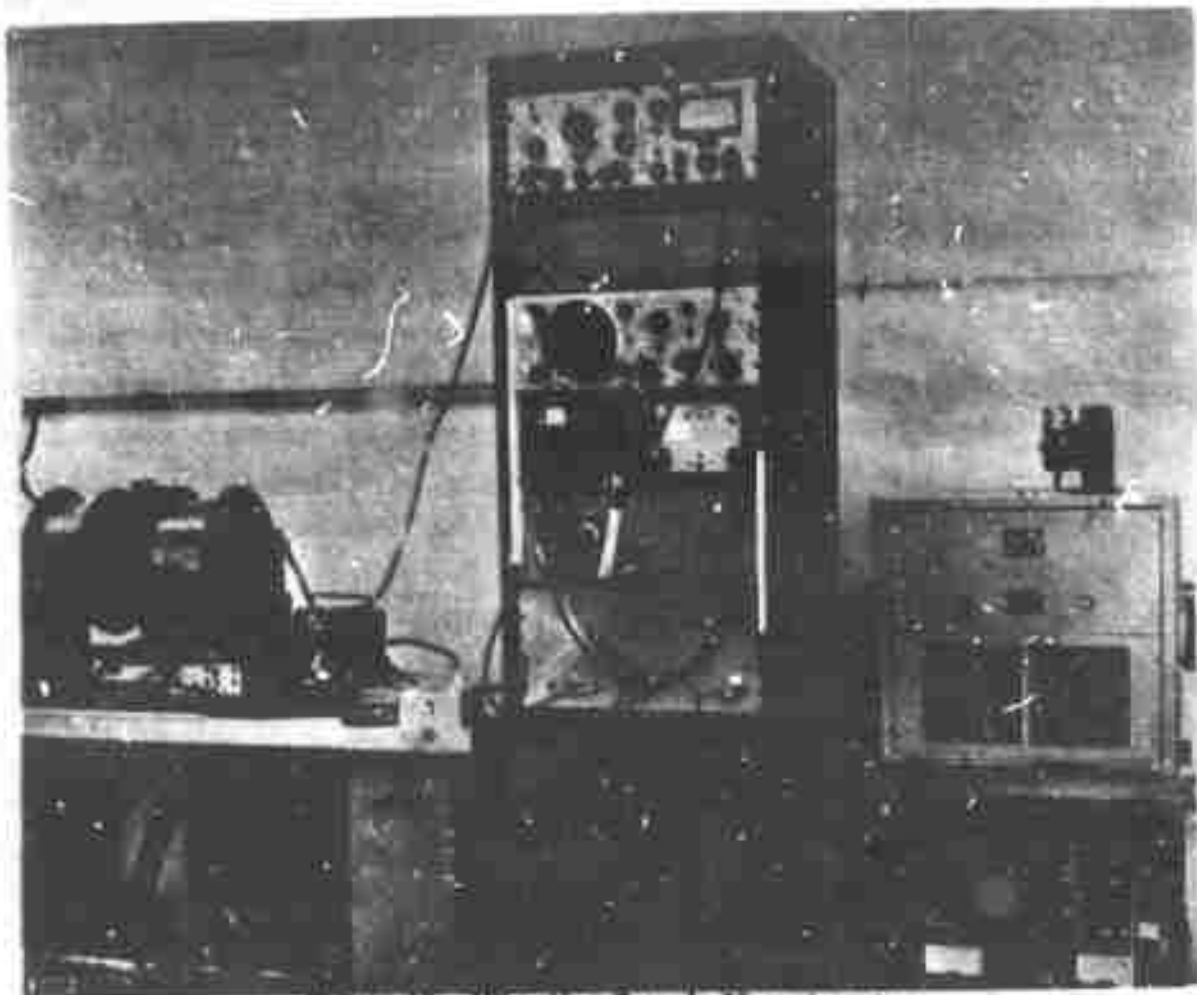


Figure 13. Vibrating Sample Magnetometer

¹⁴ Foner, "Versatile and Sensitive Vibrating Sample Magnetometer," Rev. of Scientific Instrument **30**, 549 (1959)

(b) Measurement of ΔH , g_{eff} -factor, Magnetic Susceptibility and Anisotropy Field. Reflection type resonance spectrometers were used for measurements of linewidths. The samples measured were generally in the form of spheres 20 ± 2 mils in diameter. The spheres were made by forcing a roughly cubical shaped sample of the material with compressed air around the inner periphery of a wheel coated with an abrasive powder. A 4/0 finish can easily be obtained using this method.

The effective g -factor is obtained simultaneously with the linewidth data by simply noting the field at which maximum absorption occurs and substituting this into Kittel's resonance equation. Figure 14a shows the X band resonance spectrometer and Figure 14b shows the C band resonance spectrometer in Sperry's Materials Measurements Laboratory.

This same equipment can be used for the measurement of anisotropy field in aligned single crystal samples.

By monitoring the reflected signal from the cavity or shorted coaxial line as the field is varied, it is possible to obtain a plot of resonance line profile or imaginary part of the magnetic susceptibility as a function of applied field. Such plots are of considerable value when considering materials for off resonance applications such as phase shifters.

(c) Measurement of T_c . Curie temperature measurements are done most rapidly with the simple furnace arrangement sketched in Figure 15. The test procedure is based on the balancing of gravitational and magnetic forces. As the temperature is raised and the Curie temperature is approached, the magnetization of a ferromagnetic body approaches zero. The Curie temperature can then be defined, in this measurement, as the temperature at which the force of gravity overcomes the magnetic force. The temperature at which the sample (S) drops from the magnet (P) can be determined by using two strips of foil (F) to close an electrical circuit and ring a bell when the sample forces the strips to touch. The temperature can then be read on a thermocouple. More precise determinations are made by measuring the temperature at which the magnetization falls to zero on the vibrating sample magnetometer of Figure 13. Curie temperature data are obtained directly when the saturation magnetization is measured as a function of temperature.



Figure 14 a. X Band Resonance Spectrometer

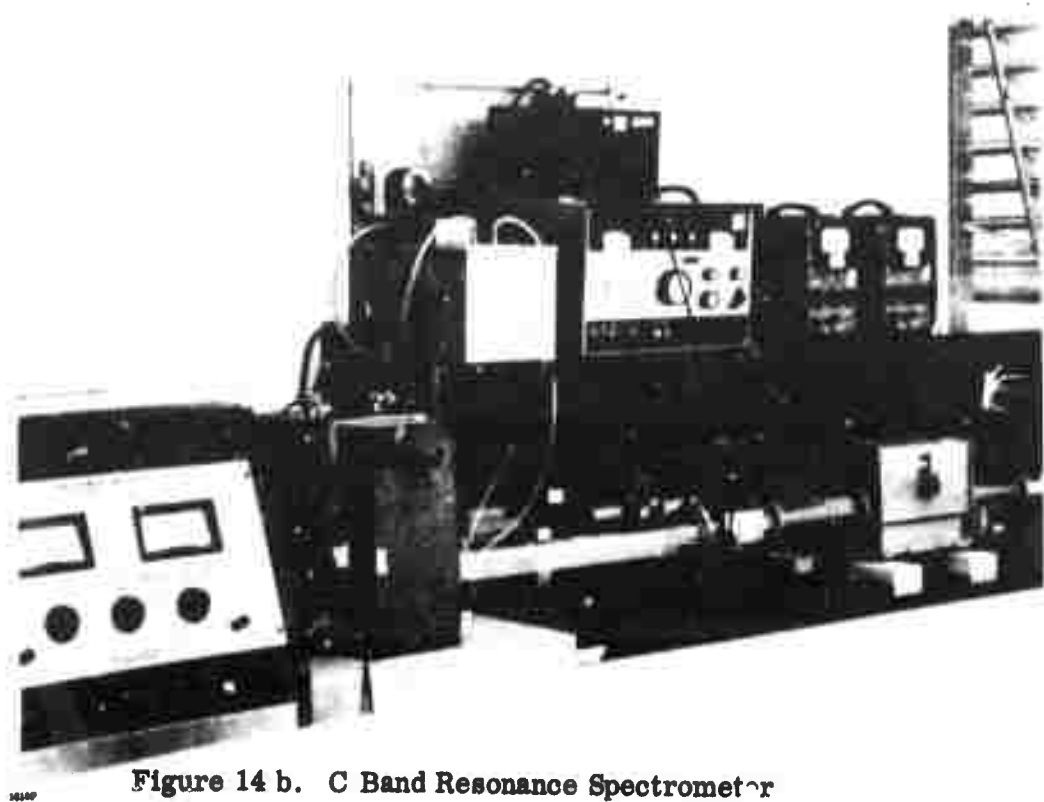


Figure 14 b. C Band Resonance Spectrometer

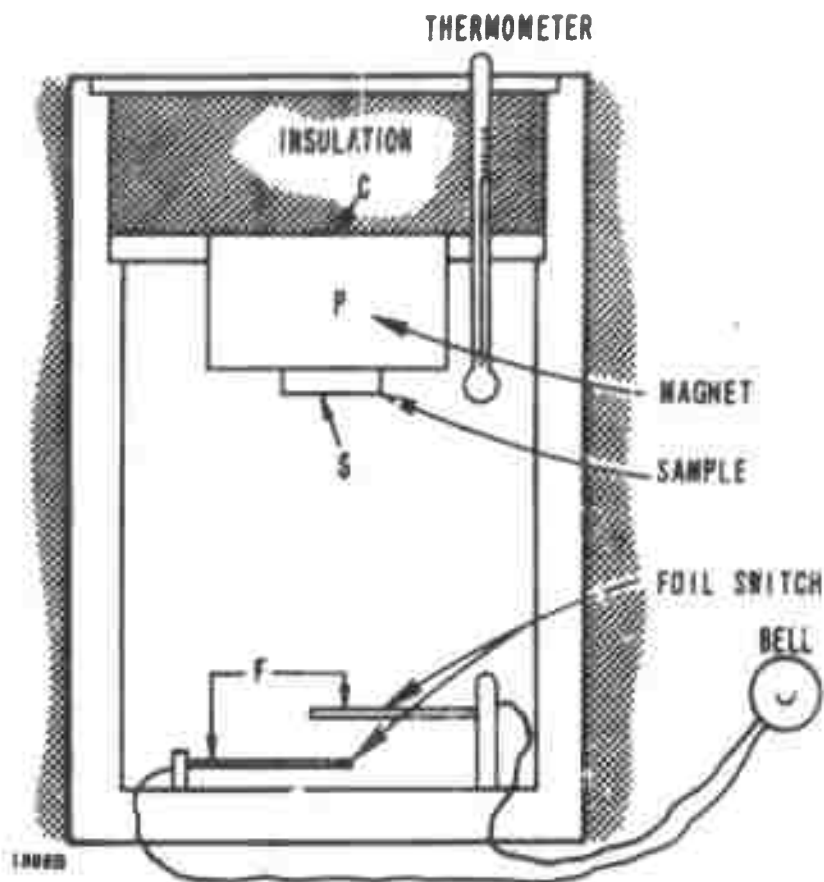


Figure 15. Furnace Arrangement for Simple Measurement of Curie Temperature. Explanatory Comments are in the Text.

(d) Measurement of Dielectric Constant and Dielectric Loss Tangent. Measurements of dielectric loss tangent and dielectric constant were made at X band. A small cylindrical sample of the material to be measured is inserted into a transmission cavity at a point of a maximum electric field and minimum magnetic field. In the case of samples with large saturation magnetizations a magnetic field is applied to essentially eliminate domain wall, magnetic, losses at the test frequency. If the Q and the resonant frequency of the cavity are known before and after a sample is inserted, $\tan \delta$ and ϵ can be calculated. $\tan \delta$ can be measured down to 0.0001 and ϵ values are accurate to about 5 percent. This equipment is shown in Figure 16.

(e) Lattice Constants and X Ray Density. The lattice constants of various garnet and ferrite compounds vary from compound to compound. For a garnet of the series $5 \text{Fe}_2\text{O}_3 \cdot 3 (\text{Y}_{2-x}\text{Gd}_x\text{O}_3)$, if the lattice constants of the end points (in this case YIG and GdIG) were known, the variation of lattice constant with x can be calculated by Vegard's rule. The lattice constant of these materials was determined from X-ray

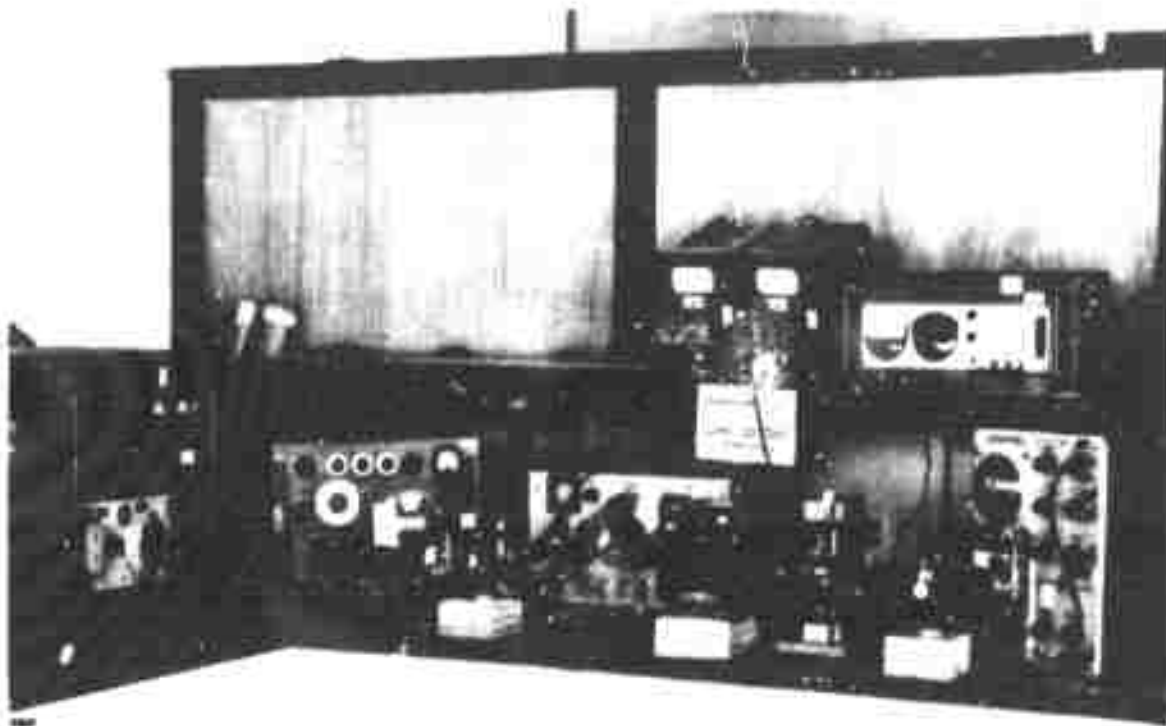


Figure 16. Dielectric Constant and Dielectric Loss Tangent Measurement Equipment (X Band)

diffractometer of Figure 17 Model (General Electric XRD-5). The theoretical density of the materials can be computed once the lattice constants and chemical composition are known. X-ray diffraction data collected on this apparatus was also used to study the phase purity of materials.

(f) Measurement of Density. Density was measured in this laboratory by weighing accurately on chemical balances a sample of regular, measured dimensions, and by computing the ratio of weight to volume. For irregular samples, a mercury volumeter was used; this device works by measurement of the buoyancy of the sample when immersed in mercury.

(g) Measurement of Remanence Ratio and Coercive Field. A hysteresisograph, or square loop tester, has been built for the evaluation and measurement of the hysteresis properties of ferrimagnetic oxides. The equipment operates at 60 cps and consists of a coaxial drive probe, integrator, function generator, peak reading voltmeter and scope display. Squareness ratio ($S_D = 4\pi M_{RD} / 4\pi M_D$) and the ratio of the coercive field to the drive field (H_C / H_D) are read directly from digital potentiometers.

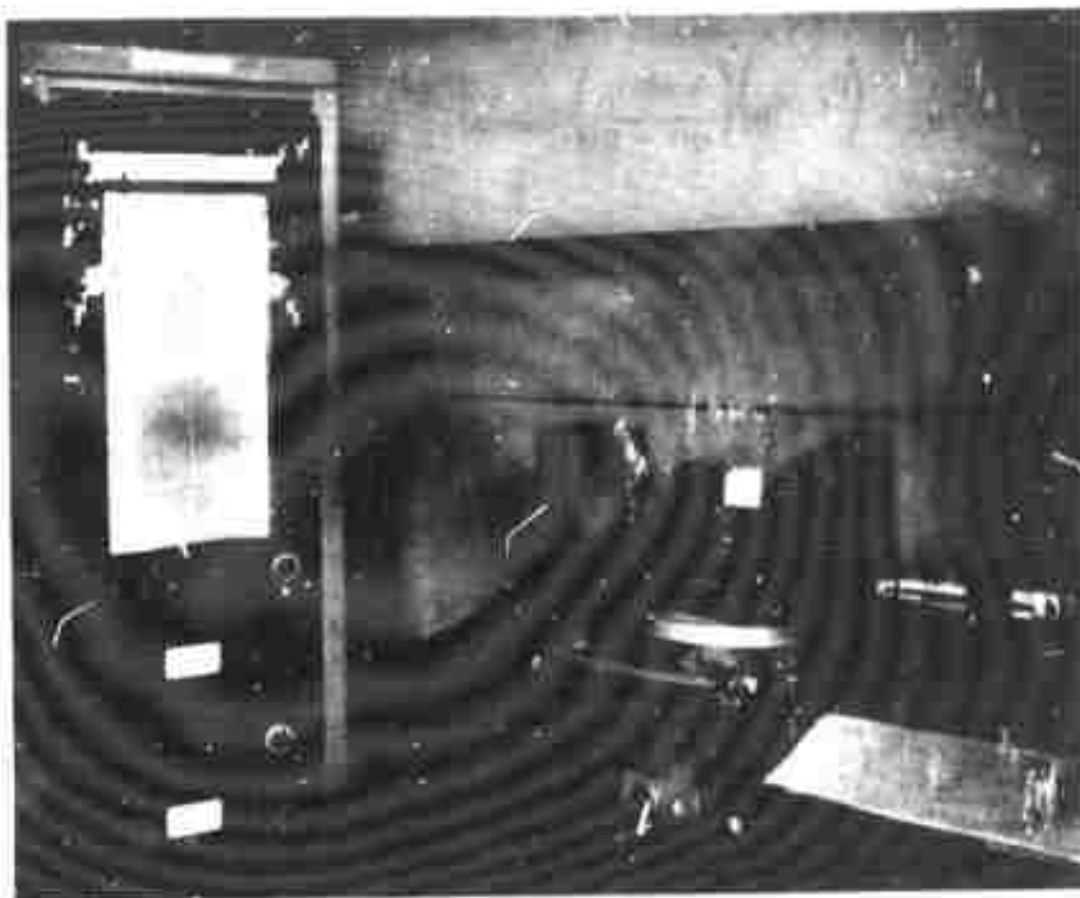


Figure 17. General Electric XRD-5 X ray Diffractometer in Sperry Microwave Electronics Company Laboratory

The square loop tester is depicted in Figure 18 and Figure 19 is a brief schematic of the apparatus.

The flux change involved in switching from $(-4\pi M_D)$ to $(+4\pi M_D)$, namely $\Delta\phi$, is calculated from the voltage read on the peak-reading voltmeter using a reference toroidal sample supplied by Mr. D.H. Temme of M.I.T. Lincoln Laboratories. The remanent flux density $(4\pi M_{RD})$ is then the product of this flux and the squareness ratio divided by the cross sectional area of the toroid legs: $4\pi M_{RD} = S_D(\Delta\phi)/A$

where

$$A = \ell W_4$$

$$\ell = \text{length of the toroid}$$

$$W_4 = \text{width of the toroid legs}$$

The coercive field is calculated from the equation

$$H_C = \left(\frac{H_C}{H_D} \right) \left(\frac{0.445 I_D}{OD + ID} \right) \text{ oersteds}$$

where

I_D = the RMS current (amperes) used to magnetize the toroid to $\pm 4\pi M_D$

and

OD, ID = the mean toroid outer and inner diameters respectively, in inches.

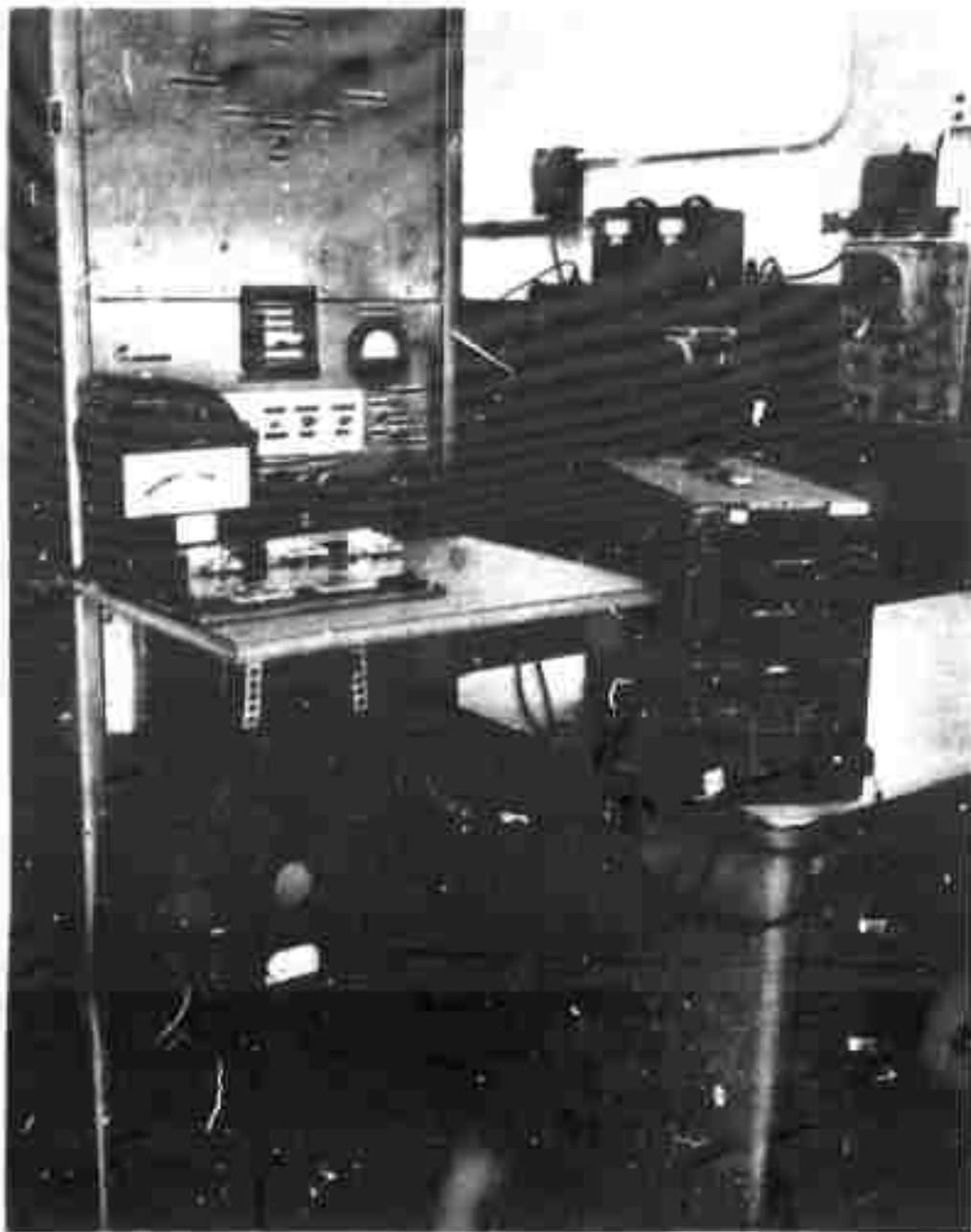


Figure 18. Square Loop Tester

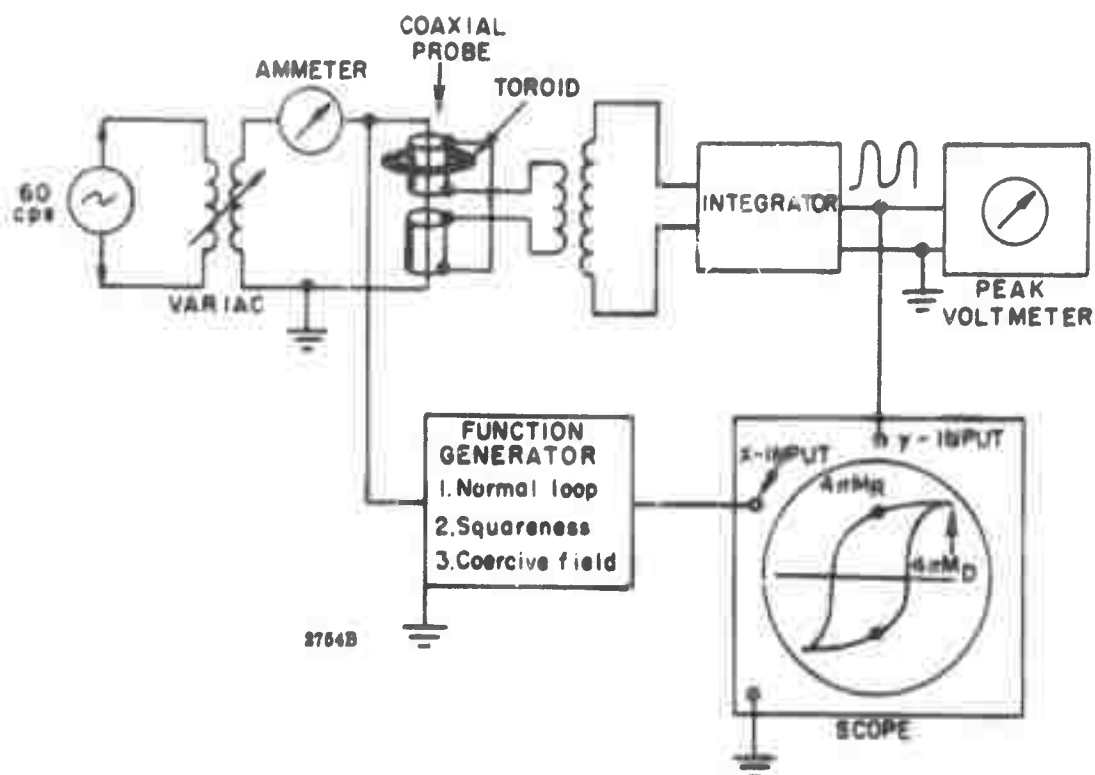


Figure 19. Schematic of Square Loop Tester Modified for Measuring the Remanent Magnetization

(h) Grain Size and Shape. A Richert metallograph was used in the measurement of grain size and shape. The instrument is capable of magnifications up to 2300 and is equipped with photographic attachments. The metallograph is shown in Figure 20.

The toroid sample which was used for measuring remanence ratio and coercive field was sliced in half with a diamond cutoff wheel. The newly exposed surface of the sample was then polished using 9 micron, 1 micron and 0.05 micron aluminum oxide polishing powders on a lapping wheel. After the proper polished surface was obtained, the sample was thermal etched for 1 hour at 200°C below the sintering temperature.

Photomicrographs, 500 magnification, were taken of the etched surface of the sample using the metallograph. Transparent material printed with hexagonal shapes were prepared as overlays for the photomicrographs. The distance between parallel sides of the hexagonal shapes were made to correspond to 5, 7, 11, 13, 16, 20, 22, 25 or 29 microns at 500 magnification. The particle size of the sample was then determined by comparison of the overlays with the photomicrograph.

(i) Average Powder Particle Size. The average particle size of each material batch was measured just before the pressing and sintering operations. The apparatus shown in Figure 21 is a Fisher Sub-Sieve Sizer. The powder samples were first heated to 500°C to drive off the wax binder, then weighed to obtain 1 cm^3 portions based on the theoretical material density. This method of measurement is supposed to have an accuracy of ± 0.05 microns.

4.2.2 Preparation Procedure

The square loop properties of these materials are strongly related to the process by which they are prepared and to the mechanical properties of the microstructure of the fired ceramic. Therefore, the preparation procedure was given special attention and studies of the structure were made at various points in the fabrication procedure.

From the raw oxide stage to the final (rf testing) stage, the following procedure was used. The particle sizes of the raw oxides were first measured in a Fisher Sub-Sieve Sizer. They were then measured out and placed in stainless steel ball jars. Batch sizes varied from 1500 to 3000 grams for the ferrites and from 1400 to 4000 grams for the garnets. The oxides were mixed by ball milling with water and one-half inch diameter stainless steel balls for 8 hours. (Mixing times of 8, 16 and 24 hours were compared in 30 and 60 percent gadolinium substituted YIG). The water was then removed by vacuum filtering, the oxides dried, screened and presintered MgO boats from 900°C to 1150°C (for 8 hours) for the ferrites and 1200°C (for 8 hours) for the garnets. Average particle sizes of some of the compositions were measured at this point with the Fisher Sub-Sieve Sizer.

A second ball milling operation (with water) was performed to achieve a good distribution of small average size particles and to introduce a binder. The ball milling time was 4 hours for the ferrites and varied from 16 to 24 hours for the garnets. The mixture was then filtered and dried and samples of the dried powders were checked for average particle sizes.

The dried powders were then pressed into hollow cylinders (for measuring square loop and switching properties), bars (to be machined into toroids for rf measurements in the 1250 MHz to 1450 MHz frequency range), and toroids (for rf measurements in C and X bands). The samples were then fired in electric furnaces at 1250°C

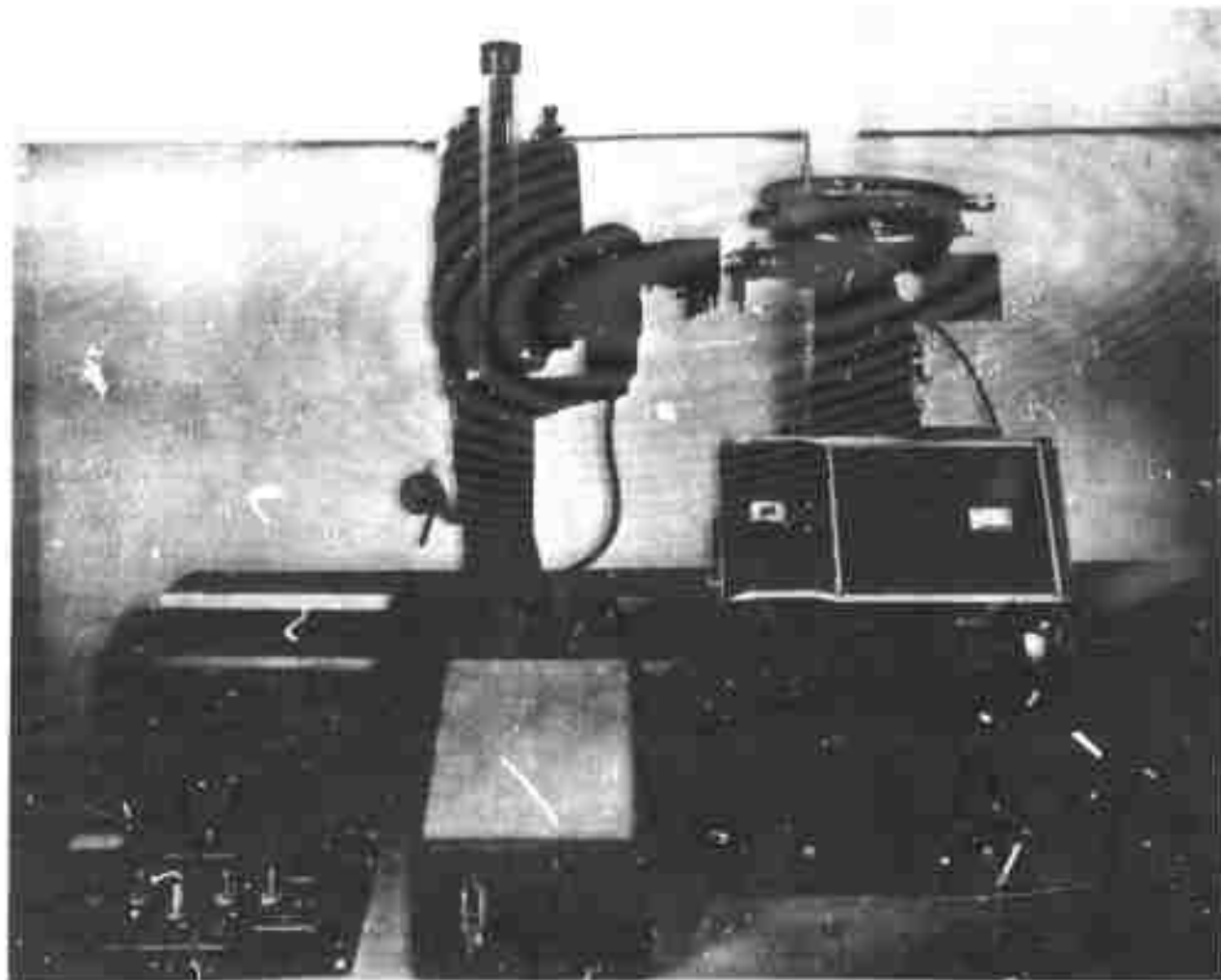


Figure 20. Richert Metallograph Used for Material Evaluation

to 1400°C for the ferrites and 1475°C to 1500°C for the garnets (except that some cylindrical samples of YIG were prepared using varying firing temperatures so as to check remanence ratio versus density). Minute samples were removed from the rf samples for measuring loss tangent, linewidth, magnetization, etc.

4.2.3 Measurement of Device Characteristics

(a) Measurement of Attenuation and VSWR. Measurement of attenuation and VSWR was done in the so-called ratio-detector setup depicted in Figure 22a. This method, described by Hunton et al,¹⁵ yields a continuous display of the loss and VSWR across the frequency band and, assuming 30 db directivity, is accurate to 7 percent. This method was used only at milliwatt power levels. At high power levels the attenuation was measured by a slightly different technique as shown in Figure 23.

¹⁵ J. K. Hunton and E. Lorence, "Improved Sweep Frequency Techniques for Broadband Microwave Test," Hewlett-Packard Journal, Vol. 12, No. 4, December 1960.

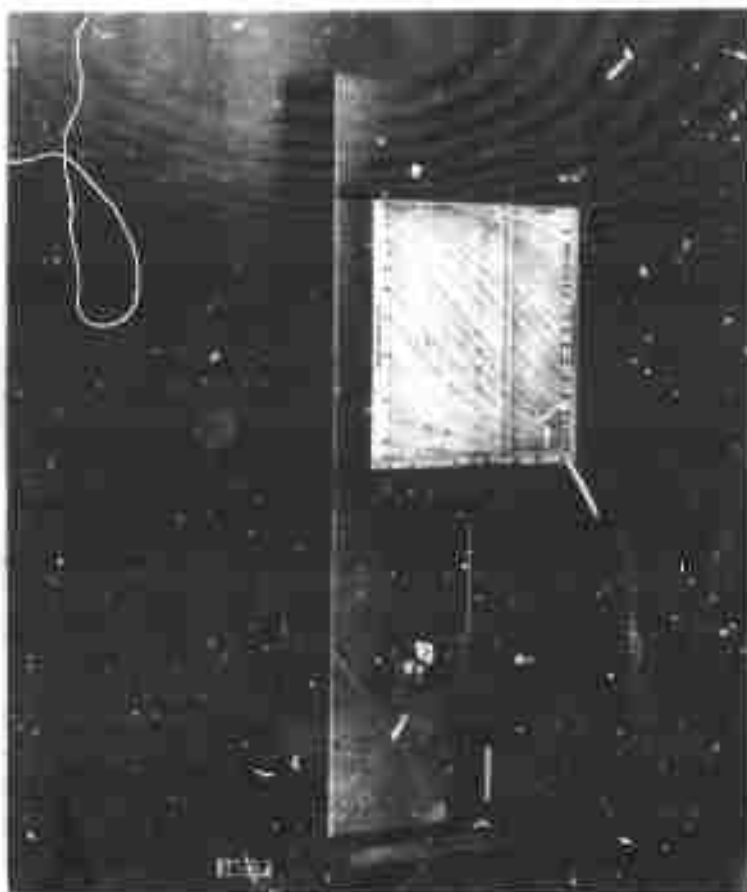
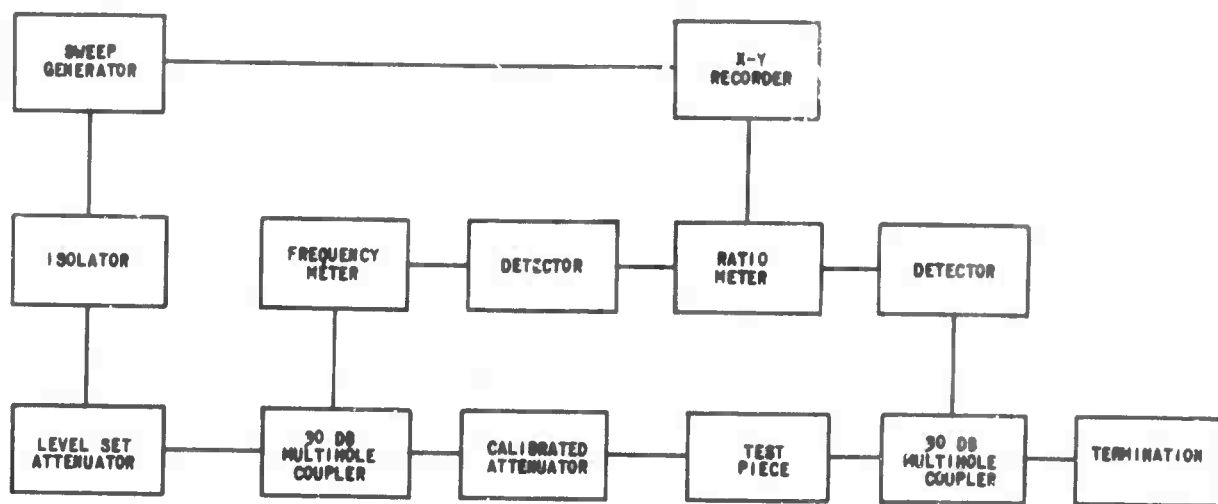
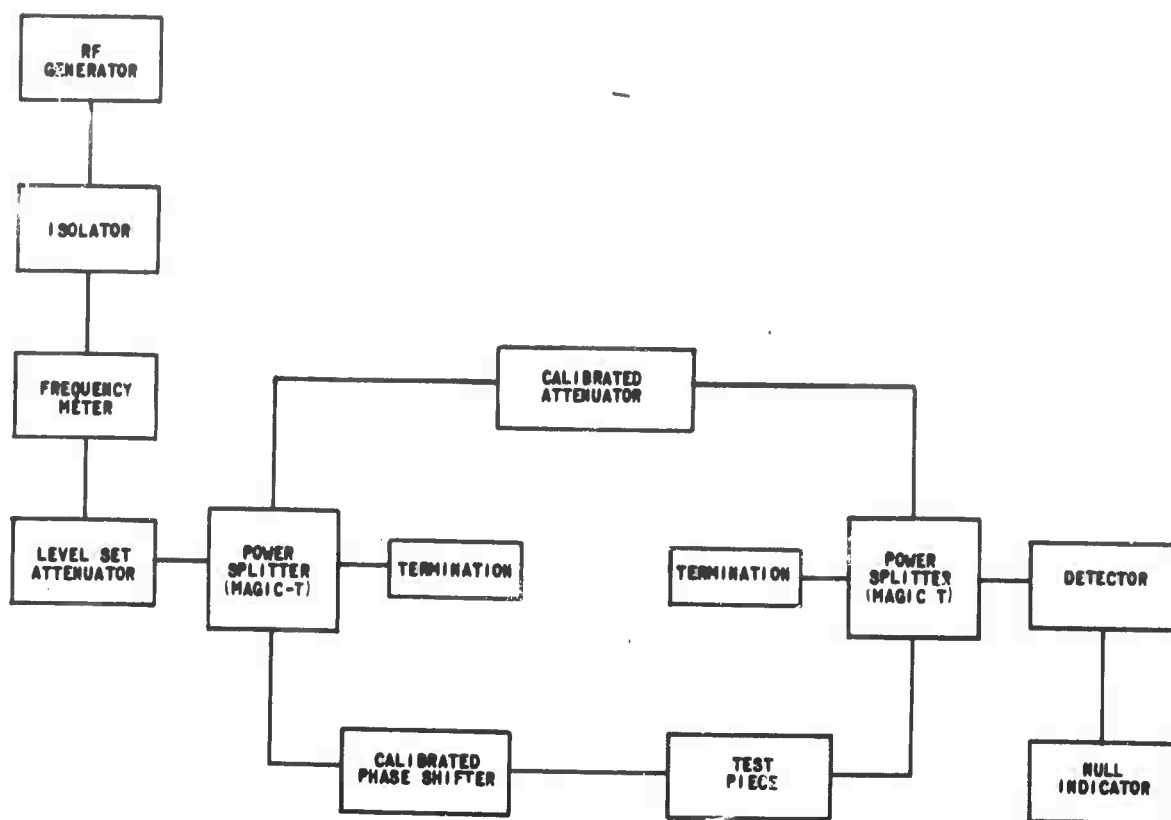


Figure 21. Fisher Sub-Sieve Sizer

(b) Measurement of Differential Phase Shift. Differential phase shift was measured in the phase bridge setup shown in Figure 22b. At the power splitter the rf energy divides with half the energy going into each arm. The losses of the test piece (digital phase shifter) in the lower arm are balanced and monitored by the calibrated attenuator in the upper arm. The ferrite is magnetized to the state corresponding to β^+ and the calibrated phase shifter is adjusted to provide a null readout at the detector. The reading on the calibrated phase shifter is noted. The ferrite is then magnetized to β^- and the calibrated phase shifter is again adjusted for a null. The second reading can now be subtracted from the first, the difference representing the differential phase shift. This method has an accuracy of better than 5 percent.



A. RATIO DETECTOR SETUP FOR MEASURING ATTENUATION AND VSWR



B. PHASE BRIDGE SETUP FOR MEASURING PHASE SHIFT

Figure 22. Laboratory Setups for Measurement of Attenuation and Phase Shift at Low Power Levels

This method of measuring phase shift is easily adapted to measurements at high power levels. The calibrated phase shifter is then used in the upper arm which is strongly decoupled from the main (high power) line containing the PDPS through the use of a multihole or crossguide coupler instead of the first magic-tee. A similar coupler is placed in the main line just after the test piece. The down-arm energy of this second coupler is combined by a magic-tee with the energy flowing through the calibrated phase shifter. Providing the main-line arm of this second coupler is well terminated, the accuracy should be 5 percent or better.

(c) Measurement of Attenuation at High Power Levels. The conventional means of measuring attenuation at high power levels are generally quite inaccurate because of drift problems associated with the high power source and the nulling of the detector-bridge apparatus. This problem has been largely solved by using the power-ratio scheme depicted in Figure 23.

This method involves the use of two 30 db multihole couplers, two attenuators, two thermistors, two average power meters and an x-y recorder. The line is first calibrated by butting the couplers and adjusting the attenuators so that, at all anticipated power levels, the recorder tracks a previously recorded zero-db line when the output from meter #1 is used to form the x-axis and the output from meter #2 forms the y-axis. Grid lines representing other attenuation levels can then be traced by appropriately setting attenuator #2. When the device is inserted in the line, its attenuation vs input power level is recorded as a continuous function of power in a matter of seconds.

This method has the following advantages over conventional methods:

1. Since power level ratios only are recorded, any fluctuations in source output cancel.
2. Because of the speed with which the measurement is made, null drift is minimized.
3. The attenuation display is continuous with increasing input power so that the onset of peak power instabilities can be detected at early levels.

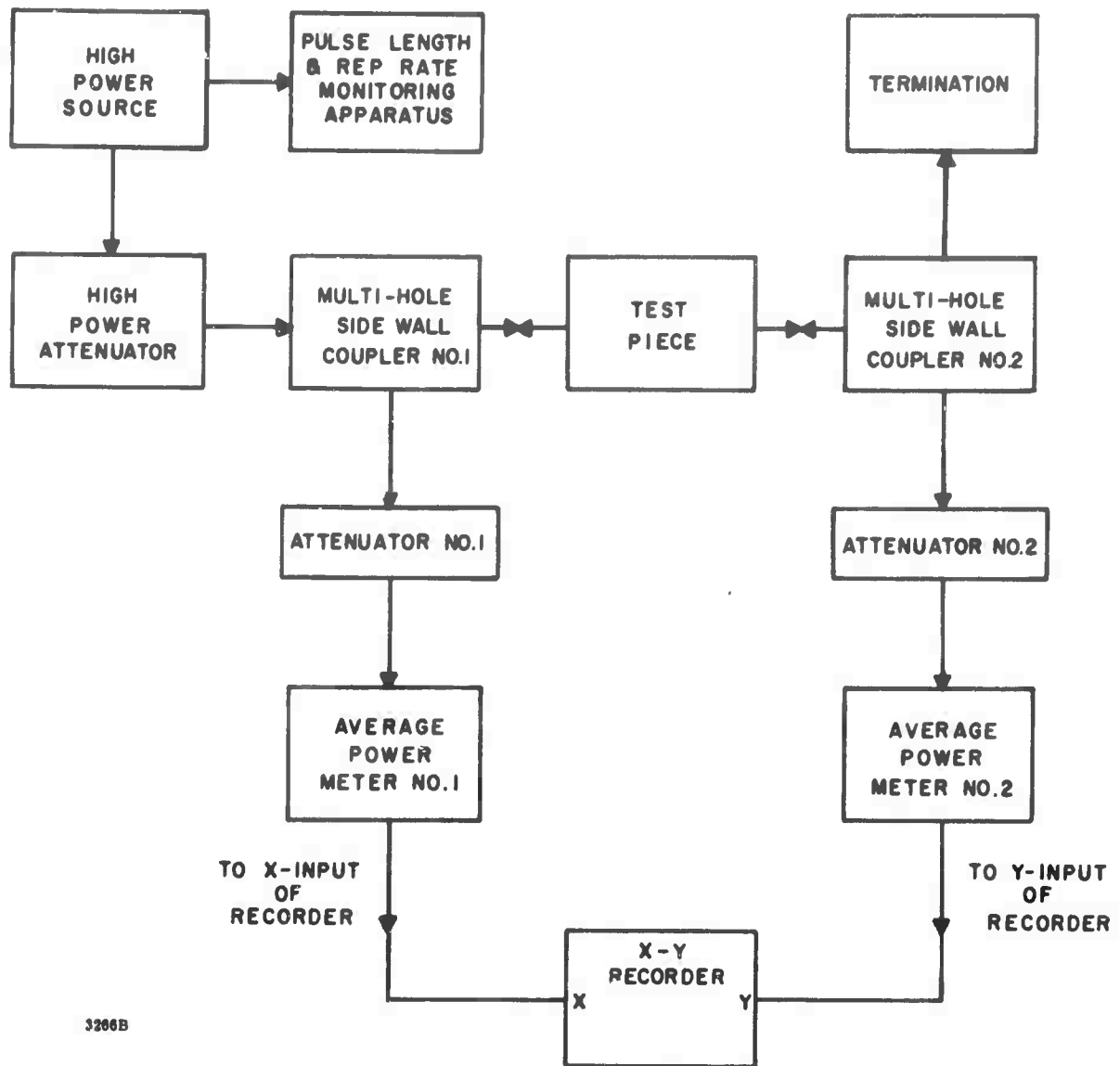


Figure 23. Power-Ratio Setup for Measuring Attenuation at High Power Levels

(d) Measurement of Switching Energy and Switching Time. The switching energy cannot be measured directly. There are several methods by which it can be measured indirectly and two are described below.

The solid traces in the graphs of Figure 24 show the voltage pulse across and the current pulse through the charging wire of the toroid. These traces are typical of the oscillograms obtained using fast-responding current and voltages probes. The dashed lines are intended to enclose a geometrical area roughly equivalent to the irregular area actually obtained. The switching energy is then

$$U_s = \int_0^0 V I (dt) \text{ (Joules).} \quad (37)$$

Typically

$$V_o = 35 \text{ volts}$$

$$I_o = 10 \text{ amps}$$

$$\Delta t = 1 \text{ microsecond}$$

so

$$U_s = 35 \times 10 \times 10^{-6} = 350 \text{ microjoules.}$$

The second method is that of measuring the rms voltage and current required for continuous switching at a rate R . Using this method

$$U_s = \frac{I_{rms} \times V_{rms}}{2R} \text{ joules} \quad (38)$$

where the factor 2 is used because R is given in cycles/second and therefore represents switching from a given state to another and back again.

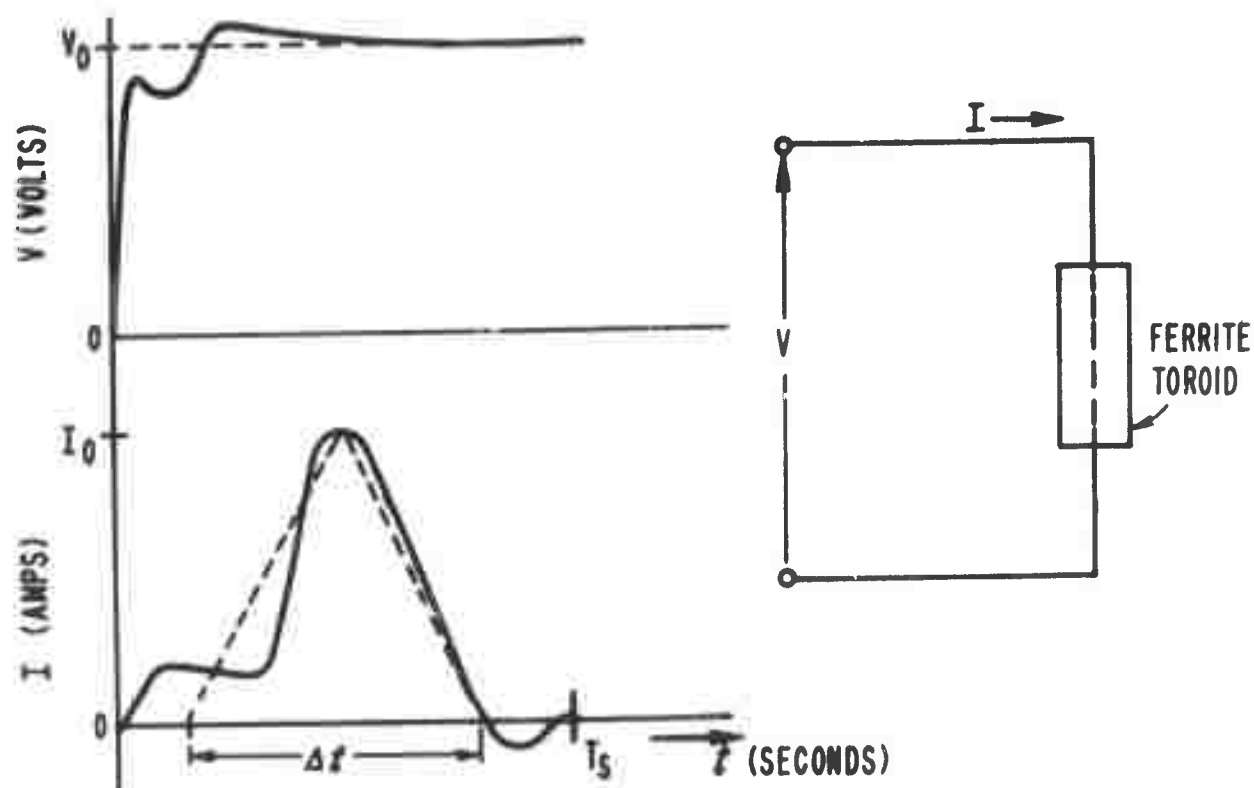


Figure 24. Typical Voltage and Current Waveforms Observed During Fast Switching of the Ferrite Toroids. The Switching Time T_s is also Shown.

4.3 MATERIALS FOR EVALUATION (COMPOSITIONS AND REASONS FOR SELECTION)

A comprehensive list of the material compositions which have been fabricated for evaluation is provided by Tables I and II of Section 4.4 and Tables V and VI of Section 4.5. It is, perhaps, worthwhile noting that the materials listed in the referenced tables have been selected a few at a time throughout the program. These materials thus, reflect a continuous feedback of the information obtained from the evaluation studies discussed in Section 4.4 and 4.5.

The suitability of a given ferrimagnetic material for use in a phase shifter ultimately depends on the performance requirements imposed on the phase shifter. Certain features, however, are desired of all good phase shifter materials. Among these are low dielectric and magnetic losses, high remanence ratio, low coercive field, high reproducibility of all properties, temperature stability of microwave and square loop properties, and low cost. Low cost is particularly important in large array applications. The relative costs of nonoriented ferrimagnetic materials can be compared by simply examining the cost of the raw oxides used in fabricating each material, since the preparation cost is reasonably constant from one material to the next. The raw oxide costs for the spinel ferrites is considerably less than that for the garnets, and when cost is the overriding factor, ferrites certainly are preferred over garnets.

In a given application tradeoffs must normally be made among the various desired properties to obtain a material that is satisfactory from all points of view. The material studies carried out on this program have been selected to determine and highlight possible trade-off areas. Particular emphasis has been placed on obtaining optimum materials for use in high peak power phase shifters in X, C, S, and L bands.

The materials listed in Tables I, II, V, and VI have been carefully selected to provide the basis for a thorough study of square loop and microwave properties of ferrimagnetic materials and their influence on the performance characteristics of FDPS. A brief summary of these investigations is as follows:

Three aluminum dysprosium doped YIG materials, three aluminum gadolinium doped YIG materials, and one aluminum gadolinium dysprosium doped material were selected for rf evaluation at low frequencies (L band). The aluminum doping is used to lower the saturation magnetization. Gadolinium doping imparts some measure of temperature (and average power) stability to the magnetization, and dysprosium doping is used to enhance the high peak power handling capacity of these materials.

Five gadolinium doped YIG materials were chosen for further studies of the dependence of loss and threshold power level on magnetization in materials with increasing anisotropy.

Four dysprosium doped YIG materials were selected to study the dependence of loss and threshold power level as a function of both magnetization and intrinsic linewidth.

Five ferrites from the nickel-zinc family were chosen for investigations of loss and threshold power level versus magnetization of these materials with larger intrinsic linewidths and widely varying anisotropy.

Four materials from the magnesium manganese aluminum ferrite family were selected to evaluate loss and threshold power level variation with magnetization for small intrinsic linewidths and varying anisotropy.

Three materials from the nickel cobalt ferrite family were selected for investigation of loss and threshold power variation with magnetization in the presence of low anisotropy and rather high intrinsic linewidths.

A single sample of lithium ferrite was also prepared for general rf evaluation in the 5 to 10 GHz frequency range.

Two compositions, namely D80A1-108 (YIG) and 91-3 (Nickel zinc ferrite), will be evaluated for below resonance (frequency-wise) operation in L band.

While some of these materials would not necessarily be selected as "good" digital phase shifter materials, they are nonetheless of considerable interest because their properties represent a wide range of intrinsic material parameters which can be used as an aid in testing and understanding the dependence of phase shifter performance on ferrite characteristics. The investigation of the dependence of magnetic loss on

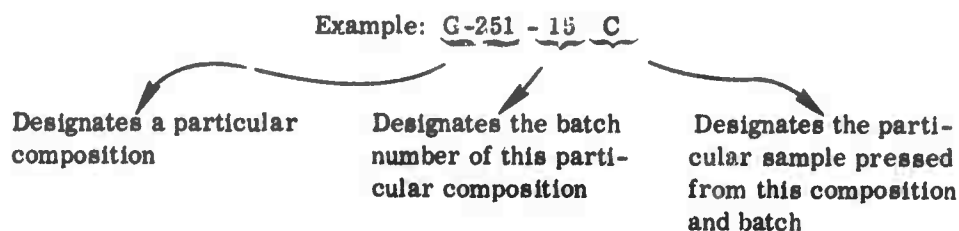
linewidth through the evaluation of the series of dysprosium doped garnets illustrates this point.

4.4 MATERIAL PROPERTIES

Tables I and II list data thus far accumulated on 14 garnet and 13 ferrite materials, respectively. Large batches of each composition were prepared for this second phase of the RADC /ARPA program so that extensive materials and device studies could be made on the same material batch. This eliminates the possibility of introducing batch-to-batch variations.

Measured properties of the compositions shown in Tables I and II are discussed in this section.

The sample nomenclature used on this program is as follows:



The average powder particle sizes were obtained using a Fisher Sub-Sieve Sizer according to the method outlined in Section 4.2.1. In general, the ferrite powders were found to have smaller average particle sizes than the garnets. However, since we are seeking here some sort of relationship between powder particle size and square loop properties for materials within a given family, further assessment must await more square loop data.

The grain size and square loop values listed were obtained from half-inch long, relatively thin walled (0.060") toroids fired in the same furnace with the device toroids. Photomicrographed surfaces were prepared in accordance with the method given in Section 4.2.1. The average grain sizes were estimated by comparing the photomicrographs with plastic overlays. At this time the data are insufficient to permit any conclusions to be made as to grain size requirements from one type of material to the next within a given family.

Some materials for these tables have been subjected to special investigations. Table III shows the effects of mixing time in 30% gadolinium substituted yttrium iron garnet and 60% gadolinium substituted yttrium iron garnet. Three batches of each material were made with mixing times of 8, 16 and 24 hours each. The usual mixing time is 8 hours. The purpose of this study was to determine if the square loop properties could be improved without degrading such microwave properties as the dielectric loss tangent. A waxing time of 24 hours was used throughout.

Powder particle size measurements made just after the mixing of the raw oxides showed a decrease in particle size with increasing mixing time as might be expected. However, there seems to be no correlation to the average particle sizes measured after the waxing time which are also shown. Furthermore, increasing the mixing time has no apparent effect on the measured densities or the measured grain sizes. The measured density for all three 30% gadolinium substituted yttrium iron garnet samples was approximately 5.50, while that for the 60% gadolinium substituted yttrium iron garnet was approximately 5.84. The grain sizes of the two compositions were approximately 12 and 16 microns for the 30% and 60% gadolinium substituted yttrium iron garnets, respectively. On the other hand, improvements in linewidth, coercive force and remanence ratio, taken on the whole, might indicate that the 24 hours mixing time is to be preferred (the observed small changes in loss tangent could very well be explained by experimental error).

Figure 25 shows photomicrographs of three samples each from the 30% and 60% gadolinium substituted yttrium iron garnets listed in Table III. It is seen from the remanence ratio and coercive force values that a reasonably good correlation exists between porosity, as evidenced by the holes, and square loop properties.

Dependence of Square Loop Properties on Porosity. Table IV lists the properties of materials fabricated to study the dependence of square loop properties on density. The remainder of these properties are listed in Table I. The composition chosen for this investigation is yttrium iron garnet. The changes in density were obtained by varying the firing temperature while the remaining fabrication variables were held constant. The firing temperature was varied between 1400°C and 1500°C with corresponding densities in the range 4.71 to 4.97.

TABLE I. GARNET
EVALUA

3 (1.0 x) Y₂O₃ · xRE

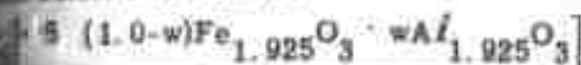
SMEC NO.	COMPOSITION		BATCH SIZE	WAXING TIME (HRS)	FIRING SCHEDULE (HRS)	P _m /P _x	PARTICLE SIZE (MICRONS)	GRAIN SIZE (MICRONS)	TAN δ
D80A1-108	0	0	3600	24	1475 5	5.08 5.17	2.50	NM	0.00
G238-6	0	0.20	2800	24	1500 5	4.98 5.04	NM	NM	0.00
G250-6	0	0.25	2750	24	1500 5	4.98 5.01	NM	NM	0.00
D80A2-1-14	0.15 Gd	0	3950	24	1475 5	5.30 5.35	2.15	NM	0.00
D80A2-2-10	0.30 Gd	0	3950	24	1475 5	5.50 5.56	1.75	12	0.00
D80A2-3-7	0.45 Gd	0	4100	24	1475 5	5.69 5.76	1.90	NM	0.00
D80A2-4-10	0.60 Gd	0	4200	24	1475 5	5.85 5.95	2.35	15	0.00
G129-4	0.02 Dy	0	2950	24	1475 5	5.14 5.20	1.90	NM	0.00
G351-4	0.05 Dy	0	2950	24	1475 5	5.18 5.32	1.85	NM	0.00
G131-3	0.10 Dy	0	3000	24	1475 5	5.26 5.25	1.90	NM	0.00
G490-1	0.02 Dy	0.20	2800	24	1500 5	5.04 5.10	NM	NM	0.00
G491-1	0.05 Dy	0.20	2850	24	1500 5	5.07 5.16	NM	NM	0.00
G431-3	0.15 Gd	0.20	2900	24	1500 5	5.20 5.24	NM	NM	0.00
G493-1	0.15 Gd 0.02 Dy	0.20	2950	24	1500 5	5.19 5.31	NM	NM	0.00

* ρ_m = measured density

ρ_x = x-ray density

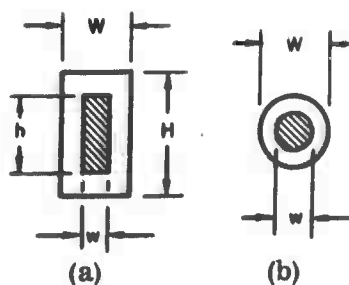
A

MATERIALS SELECTED FOR FURTHER
 FROM THE FAMILY



SAMPLE	LINE WIDTH (μm or inches)	4T H_c (GAUSS)	DRIVE CURRENT (AMPS RMS)	COERCIVE FIELD H_c (Oe) (100-)	COERCIVE FIELD (mG/M ₂)	SQUAREDNESS S_2	4T H_{90} (GAUSS)	REMANENCE RATIO R_R	SAMPLE SHAPE	w/t
1.02	47	1780	10.0	0.76	8.96	0.744	1165	0.825	b	0.385 0.265
2.02	35	NM	10.0	0.71	10.0b	0.851	250	NM	b	0.385 0.265
2.03	38	290	9.7	0.68	10.0b	0.518	100	0.345	b	0.385 0.265
2.02	47	NM	11.8	0.86	10.0b	0.783	1057	NM	b	0.385 0.265
2.02	66	NM	15.0	1.00	10.0	0.755	817	NM	b	0.385 0.265
2.02	69	NM	14.3	1.04	10.0	0.667	680	NM	b	0.385 0.265
2.05	220	710	20.0	2.59	5.80	0.589	290	0.405	b	0.385 0.265
1.99	91	1780	10.0	0.75	10.0	0.878	1340	0.755	b	0.385 0.265
1.96	164	NM	10.0	0.77	9.0	0.873	1256	NM	b	0.385 0.265
1.88	295	1755	10.0	0.90	8.0	0.875	1170	0.665	b	0.385 0.265
1.96	123	NM	9.25	0.85	10.0	0.590	220	NM	b	0.385 0.265
1.86	274	NM	9.90	0.72	10.0	0.437	160	NM	b	0.385 0.265
2.05	110	370	17.1	1.20	10.0	0.575	130	0.350	b	0.385 0.265
1.95	230	300	15.2	1.09	10.0	0.594	120	0.400	b	0.385 0.265

*SAMPLE SHAPE



B

TABLE II. χ^2 [illegible]

* ρ_m = measured density
 ρ_x = x-ray density

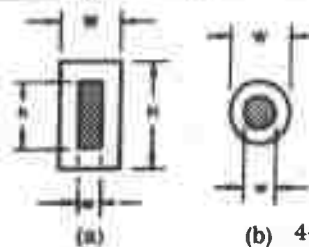
2000

A

WRITES SELECTED FOR EVALUATION

DATE	TIME	2 FACTOR	LINE WIDTH (INCHES)	4TH W ₂ (INCHES)	SPIN (SAMPLE SIZE)	REACTIVE FIELD P ₂ (INCHES)	CORRODE FIELD (INCHES)	SQUARENESS S ₂	4TH W ₂ (INCHES)	PERMANENCE RATIO R ₂	SAMPLE SHAPE	W ₂
0.010	12.6	2.44	520	2610	20.0	5.00	2.80	0.709	895	0.355	b	0.355
0.006	12.7	2.38	465	2965	20.0	6.80	2.15	0.803	1220	0.410	b	0.385
0.015	12.8	2.27	279	3820	20.0	3.20	4.80	0.750	1854	0.485	b	0.385
0.0010	13.7	2.13	115	3770	NM	NM	NM	NM	NM	NM	b	0.385
0.001	14.1	2.07	107	3770	2.53	0.18	10.0	0.342	535	0.196	b	0.385
0.001	12.8	2.13	512	2965	20.0	2.35	6.20	0.811	1175	0.370	b	0.385
0.005	12.3	NM	NM	NM	NM	NM	NM	NM	NM	NM	b	0.385
0.001	11.7	NM	NM	NM	NM	NM	NM	NM	NM	NM	b	0.385
0.001	11.5	NM	NM	NM	NM	NM	NM	NM	NM	NM	b	0.385
NM	NM	NM	NM	NM	NM	NM	NM	NM	NM	NM	b	0.385
NM	NM	NM	NM	NM	NM	NM	NM	NM	NM	NM	b	0.385
NM	NM	NM	NM	NM	NM	NM	NM	NM	NM	NM	b	0.385
0.009	12.5	2.35	625	NM	NM	NM	NM	NM	NM	NM	b	0.385
0.01	NM	2.23	595	3365	20.0	2.24	4.50	0.848	2175	0.645	b	0.385

*SAMPLE SHAPE



(b) 4-23/24

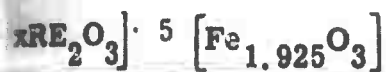
B

SAMPLE NO.	COMPOSITION	BATCH SIZE	MIXING TIME (HOURS)	PARTICLE SIZE (MICRONS)	HEATING TIME (HOURS)	PARTICLE SIZE (MICRONS)	FIRING SCHEDULE (°C/h)	YIELD (%)
D80A2-2-10B	0.30 Gd	3950	8	1.70	24	1.75	1475 / 5	5
D80A2-2-10C	0.30 Gd	3950	8		24	1.75	1475 / 5	5
D80A2-2-11B	0.30 Gd	3950	16	1.60	24	1.75	1475 / 5	5
D80A2-2-11C	0.30 Gd	3950	16		24	1.75	1475 / 5	5
D80A2-2-12B	0.30 Gd	3950	24	1.50	24	1.80	1475 / 5	5
D80A2-2-12C	0.30 Gd	3950	24		24	1.80	1475 / 5	5
D80A2-4-10B	0.60 Gd	4200	8	2.25	24	2.45	1475 / 5	5
D80A2-4-10C	0.60 Gd	4200	8		24	2.45	1475 / 5	5
D80A2-4-11B	0.60 Gd	4200	16	2.10	24	2.40	1475 / 5	5
D80A2-4-11C	0.60 Gd	4200	16		24	2.40	1475 / 5	5
D80A2-4-12B	0.60 Gd	4200	24	1.80	24	2.00	1475 / 5	5
D80A2-4-12C	0.60 Gd	4200	24		24	2.00	1475 / 5	5

A

004002

EFFECTS OF MIXING TIME IN TWO
 REACTIONS FROM THE FAMILY



GRIN SIZE (MICRONS)	S FACTOR	LINE WIDTH (MICRONS)	STRENGTH (KILOPOUNDS)	TENSILE STRENGTH (KILOPOUNDS)	COMPRESSION FIELD STRENGTH (KILOPOUNDS)	SQUARENESS RATIO	477 HZ (KILOCYCLES)	REMANENCE RATIO R _B	SAMPLE SHAPE	W/A
13	2.02	65	1200	0.0011 16.2	0.90	0.837	1005	0.70	b	0.385 0.265
NM	NM	NM	NM	NM	0.90	0.837	1005	0.70	b	0.385 0.265
NM	2.02	75	NM	0.0008 16.2	1.00	0.781	950	0.64	b	0.385 0.265
12	NM	NM	NM	NM	1.00	0.788	945	0.63	b	0.385 0.265
NM	2.02	59	NM	0.0016 16.0	0.95	0.821	1093	0.71	b	0.385 0.265
14	NM	NM	NM	NM	0.95	0.844	1013	0.72	b	0.385 0.265
NM	2.05	235	716	0.0021 16.2	2.20	0.539	386	0.33	b	NM
15	NM	NM	NM	NM	2.25	0.550	394	0.34	b	NM
NM	2.05	225	NM	0.0037 16.5	2.10	0.569	407	0.36	b	NM
16	NM	NM	NM	NM	2.10	0.576	412	0.36	b	NM
NM	2.06	220	NM	0.0013 16.5	2.05	0.574	411	0.37	b	NM
10	NM	NM	NM	NM	2.05	0.571	409	0.37	b	NM

*SAMPLE SHAPE

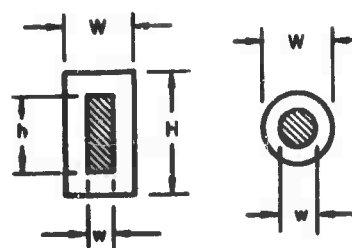


TABLE IV. PROPERTIES OF MATERIALS FABRICATED TO STUDY
THE DEPENDENCE OF SQUARE LOOP PROPERTIES ON DENSITY

SMEC No.	Firing Temp/ Time (°C/hr)	Density (gm/ Cm ³)	$\rho_m /$ ρ_x^*	$4\pi M_s$ (Gauss)	$4\pi M_r$ (Gauss)	Reman- ence Ratio	Coercive Force (Oer- stedes)
D80A1-108J	1400/5	4.76	0.9207	1639	972	0.546	1.12
D80A1-108K	1400/5	4.71	0.9110	1622	972	0.546	1.12
D80A1-108G	1425/5	4.75	0.9188	1635	990	0.556	1.05
D80A1-108H	1425/5	4.83	0.9342	1663	1013	0.569	1.01
D80A1-108E	1450/5	4.80	0.9284	1653	1013	0.569	0.94
D80A1-108F	1450/5	4.92	0.9517	1694	1100	0.618	0.78
D80A1-108	1475	4.94	0.9555	1700	1152	0.647	0.63
D80A1-108	1475	4.92	0.9517	1694	1062	0.597	0.59
D80A1-108	1500	4.97	0.9613	1711	1098	0.617	0.41

* ρ_m = Measured density
 ρ_x = X-ray density



D80A2-4-10C Mix Time=8 hours
Average Grain Size=15 microns
Density=5.85 gm/Cm³
R_r=.34 H_c=2.25 oe.



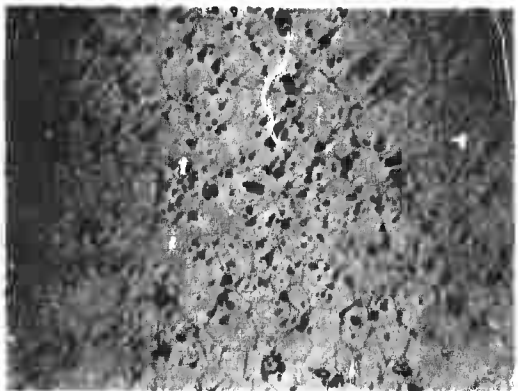
D80A2-2-10C Mix Time=8 hours
Average Grain Size=13 microns
Density=5.50 gm/Cm³
R_r=.20 H_c=.90 oe.



D80A2-4-11C Mix Time=16 hours
Average Grain Size=16 microns
Density=5.82 gm/Cm³
R_r=.38 H_c=2.10 oe.



D80A2-2-11C Mix Time=16 hours
Average Grain Size=12 microns
Density=5.48 gm/Cm³
R_r=.63 H_c=1.00 oe.



D80A2-4-12C Mix Time=24 hours
Average Grain Size=16 microns
Density=5.88 gm/Cm³
R_r=.37 H_c=2.05 oe.



D80A2-2-12C Mix Time=24 hours
Average Grain Size=12 microns
Density=5.49 gm/Cm³
R_r=.72 H_c=.95 oe.

Figure 25. Photomicrographs of 60% Gadolinium Substituted YIG and 30% Gadolinium Substituted YIG

60 4002

In general, the remanence ratio increased with increasing density while the coercive force decreased with increasing density. These data are shown graphically in Figure 26, plotted as a function of the percent theoretical density. In these calculations the theoretical density of this yttrium iron garnet material was taken as 5.17. This number is calculated from the measured x-ray lattice constant. In Figure 26 it is seen that the remanence ratio increases from 0.50, corresponding to 91% theoretical density, to 0.605 corresponding to 96% density. The coercive force decreases from approximately 1.20 oersteds at 91% to about 0.60 oersteds at 95.5% theoretical density. Thus, a general improvement in square loop properties of these yttrium iron garnet samples is obtained by increasing the density.

Temperature Dependence of Square Loop Properties. Figure 27 shows the remanence ratio and coercive force dependence on temperature in a round, thin walled toroid of 2% dysprosium substituted yttrium iron garnet. Also shown is the variation of the magnetization of yttrium iron garnet with temperature over this temperature range of -100°C to $+100^{\circ}\text{C}$. The coercive force is seen to decrease quite linearly from 1.18 oersteds at -100°C to 0.55 oersteds at $+100^{\circ}\text{C}$. This is a result which is felt to reflect the temperature dependence of the anisotropy field. The remanence magnetization also decreases rather linearly over this range from about 1560 gauss at -100°C to about 1080 gauss at $+100^{\circ}\text{C}$. The rate of decrease of the remanent magnetization is not as rapid as the decrease in saturation magnetization of the yttrium iron garnet. The reason for this decreased dependence on temperature in the remanence magnetization is probably connected to the concurrent decrease in coercive force. When a constant current drive is used, the net effect is that of driving the sample harder at the higher temperatures. This is shown graphically in Figures 28 and 29.

Figures 28 and 29 also show the remanent magnetization dependence on temperature in two nearly identical garnet materials measured in the one case with H_d/H_c constant and in the other case with the driving current constant. A marked difference is observed in the rate of decrease of the remanent magnetization with increasing temperature as determined by the two methods of measurement. Using a constant current drive, the remanence ratio is found to remain very nearly constant over this temperature range, while with the constant ratio of drive field to coercive field the remanence ratio continually decreases with increasing temperature. This may evidence

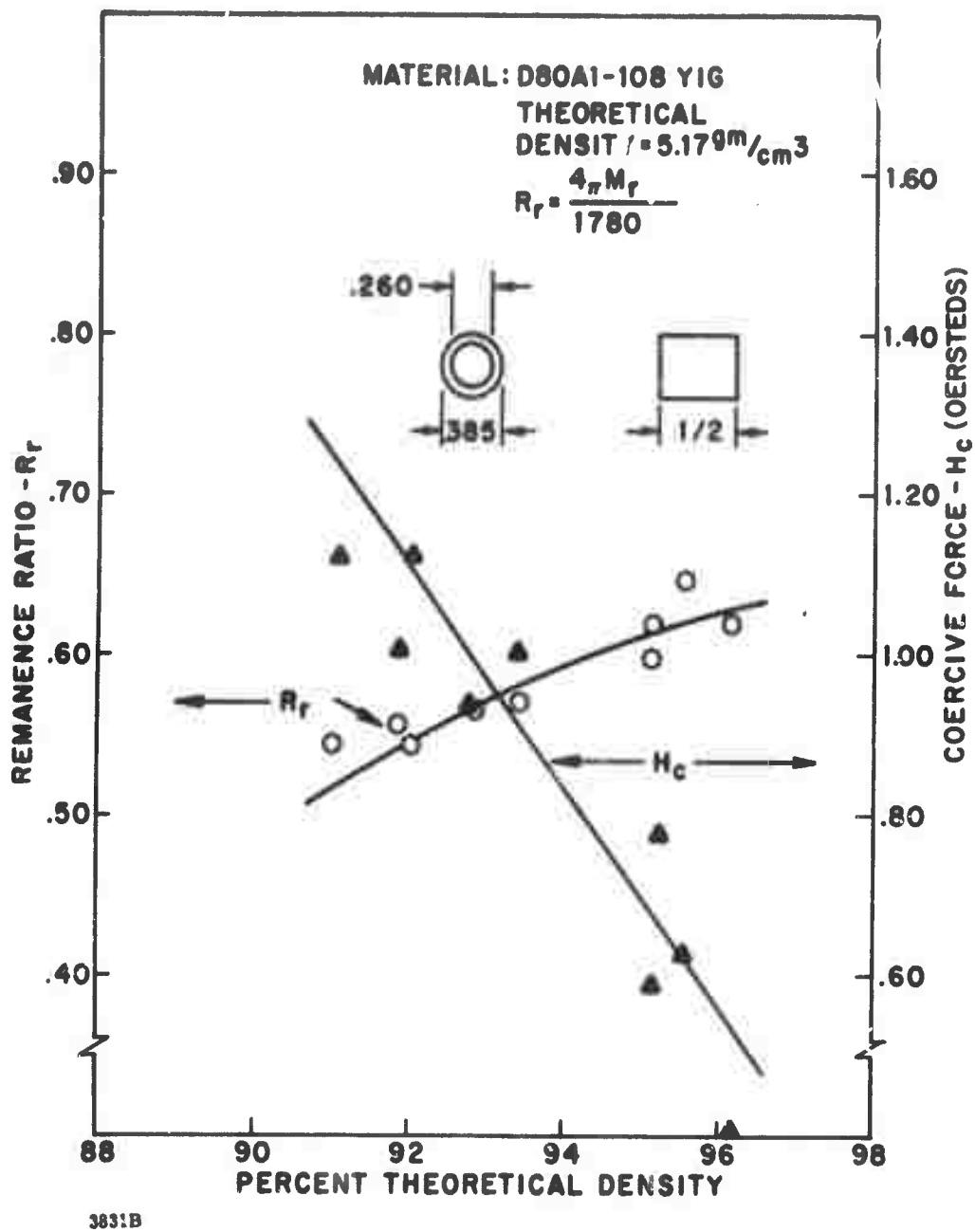


Figure 26. Remanent Magnetization and Coercive Force Dependence on Temperature with Drive Current (I_D) Constant

JU4002

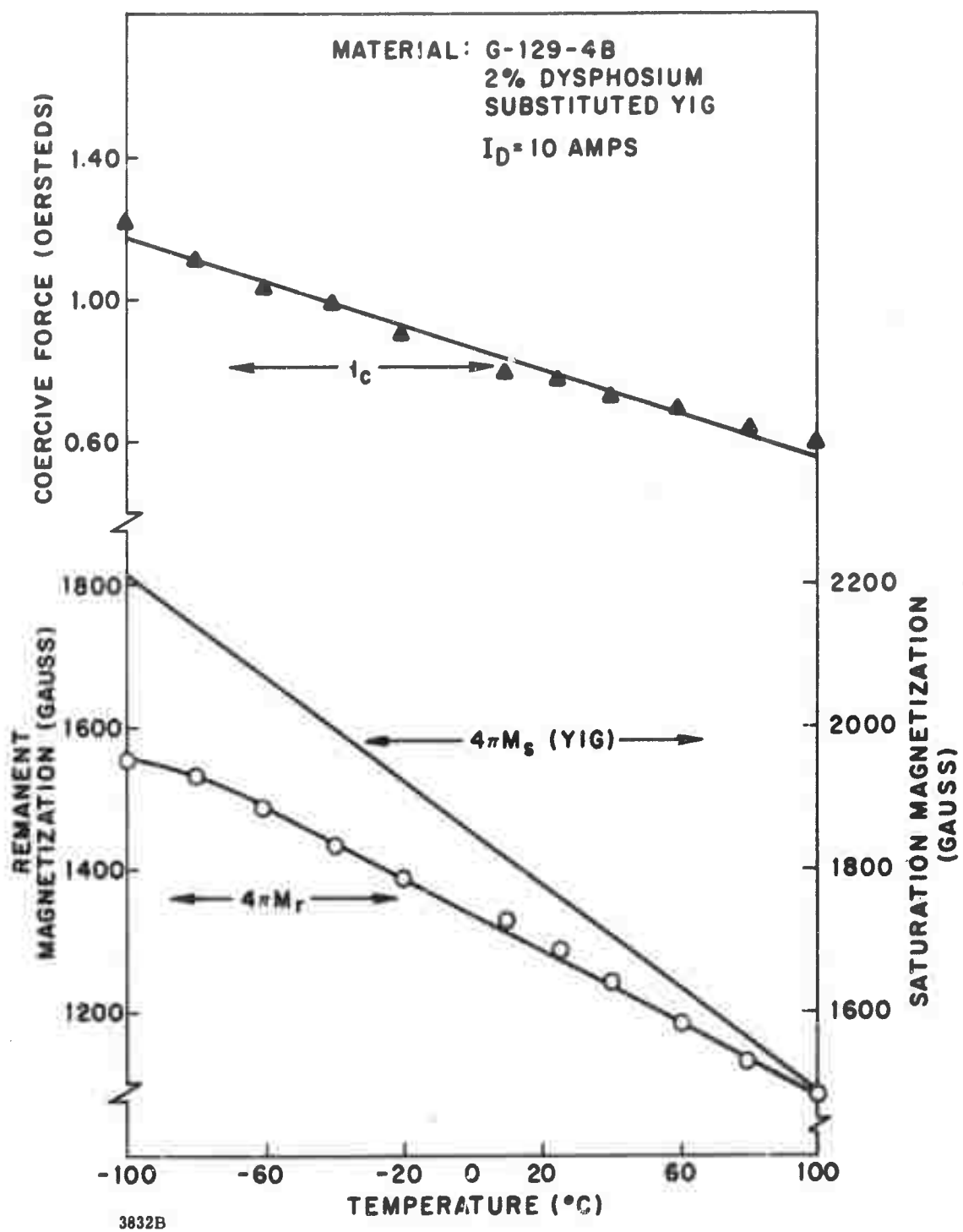
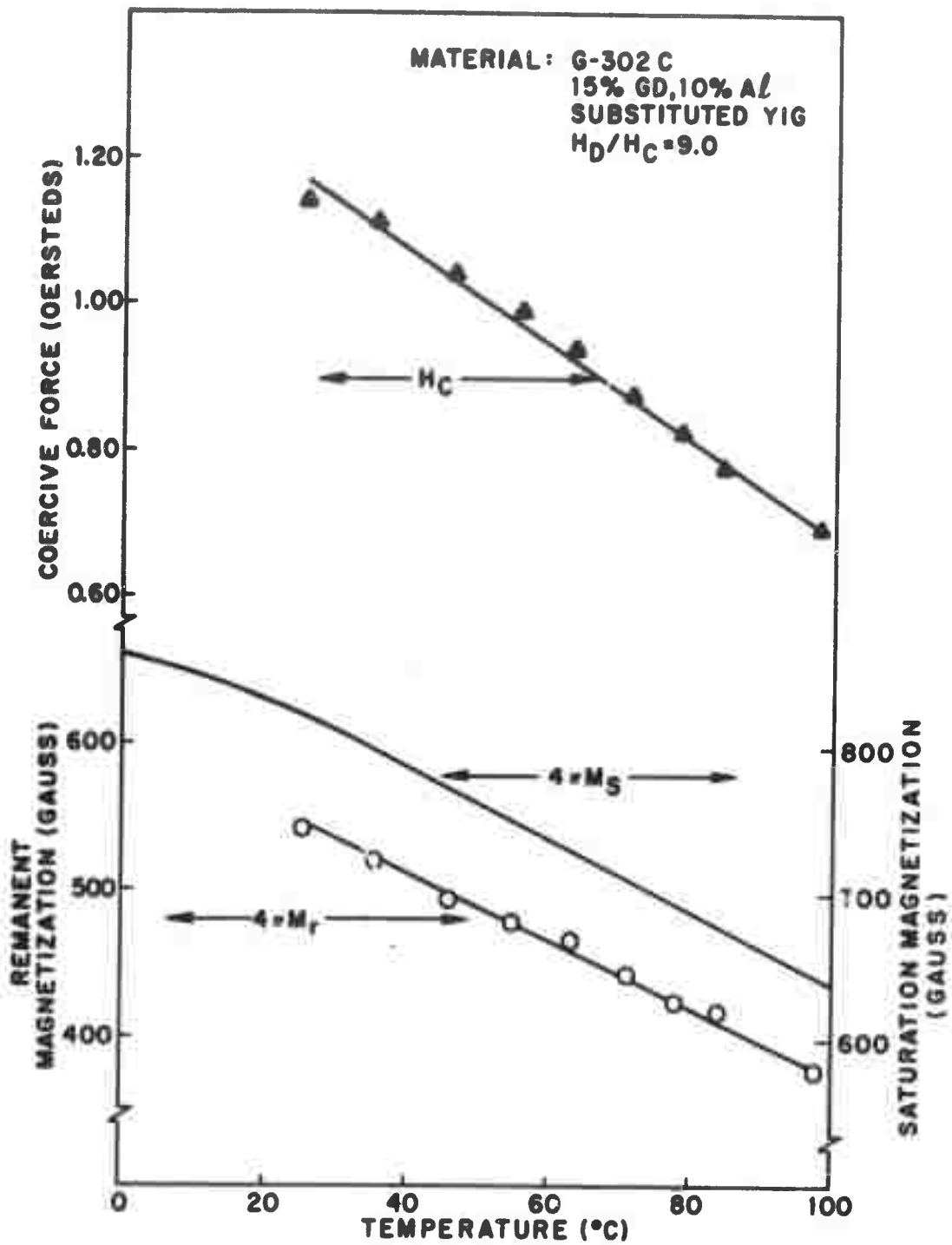


Figure 27. Remanence Ratio and Coercive Force Versus Temperature with Constant Drive Current L_D



3829B

Figure 28. Remanent Magnetization and Coercive Force Dependence on Temperature with H_D/H_C Constant

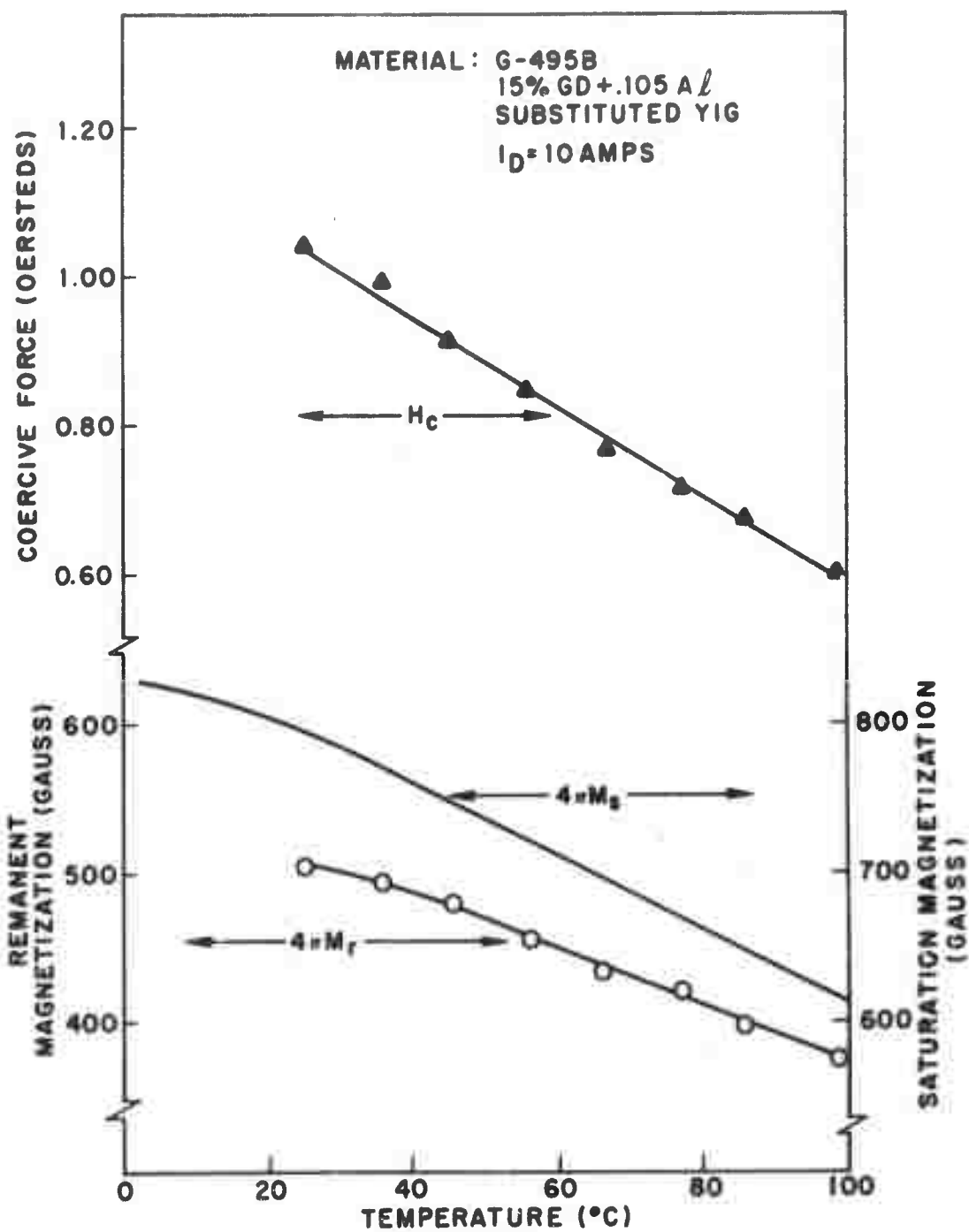


Figure 29. Remanent Magnetization and Coercive Force Dependence on Temperature with Drive Current (I_D) Constant

an inherent increase in remanence ratio with increasing anisotropy field. As stated earlier in Section 3.4, a very large anisotropy field should cause the remanence ratio to approach 0.87 in cubic materials.

Figure 30 shows the remanent magnetization and coercive force dependence on temperature in a round, thin walled toroid of 30% gadolinium substituted YIG. Also shown is the typical variation in saturation magnetization of this type material with temperature. The coercive field is again seen to decrease approximately linearly over the temperature range -100°C to $+100^{\circ}\text{C}$ from 1.19 oersteds to about 0.76 oersteds. The remanence magnetization varies approximately as the saturation magnetization over this temperature range, except that at the lower temperature extreme it is seen to flatten out. This flattening may be explained by the increased coercive force which has the effect of holding the remanence magnetization at a higher level. That is to say, the sample is less prone to demagnetize after the driving pulse by virtue of the increased anisotropy field which can help offset the effects of porosity, etc.

During these measurements, the ratio of H_d/H_c (the ratio of the driving field to the coercive field) has been allowed to vary and the driving current was held constant. This is approximately the situation found in an actual working device. If the current is varied so as to hold the ratio H_d/H_c constant, the remanent magnetization is again found to decrease more rapidly with increasing temperature.

The temperature characteristics of many materials from the yttrium-gadolinium-iron and the yttrium-gadolinium-aluminum-iron garnet families are presented in Figures 31, 32, 33, 34, 35 and 36. These results show the degree of temperature compensation possible and illustrate that materials possessing almost any value of magnetization up to a value of approximately 1200 can be prepared and temperature compensated.

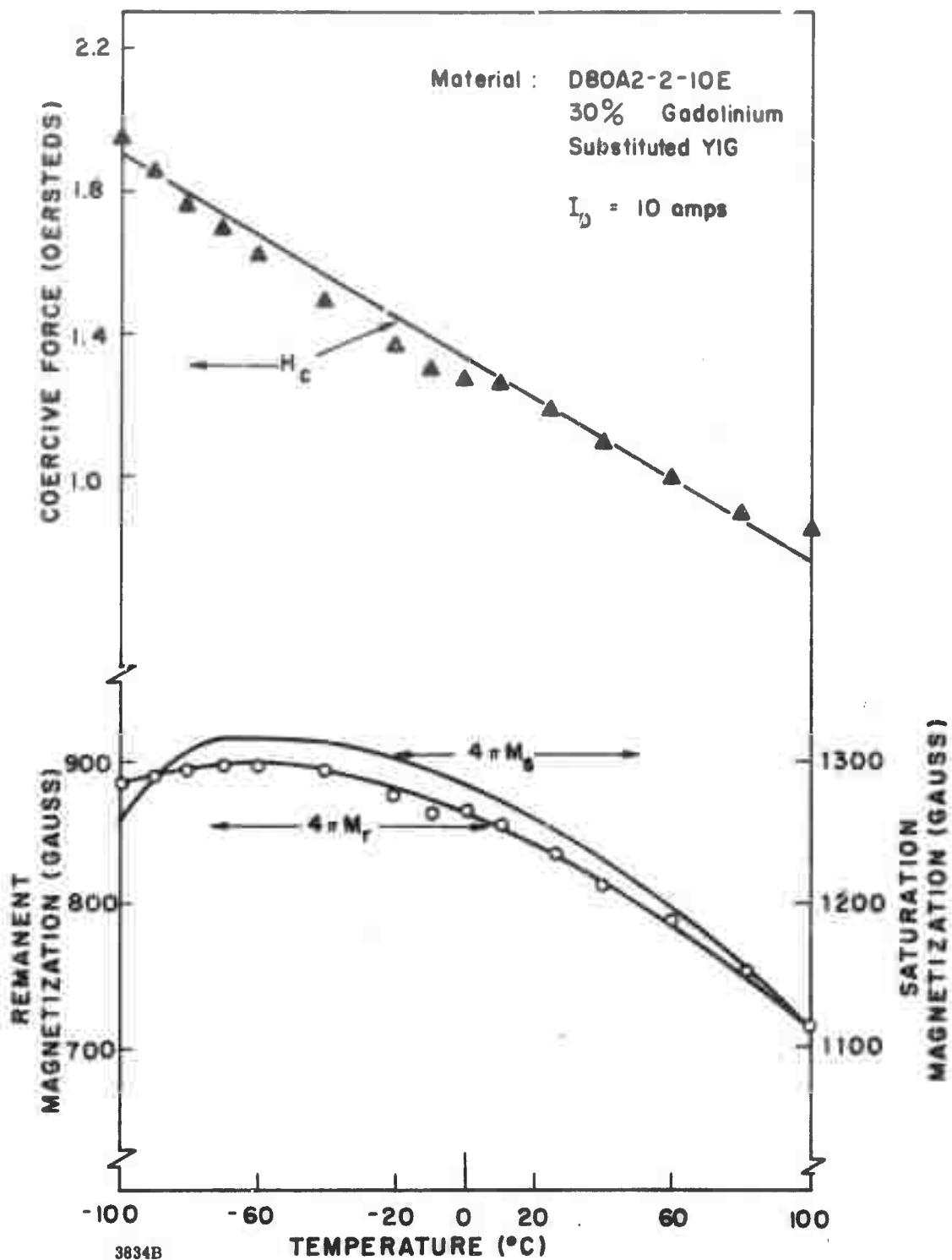


Figure 30. Remanent Magnetization and Coercive Force Versus Temperature with Constant Drive Current I_D

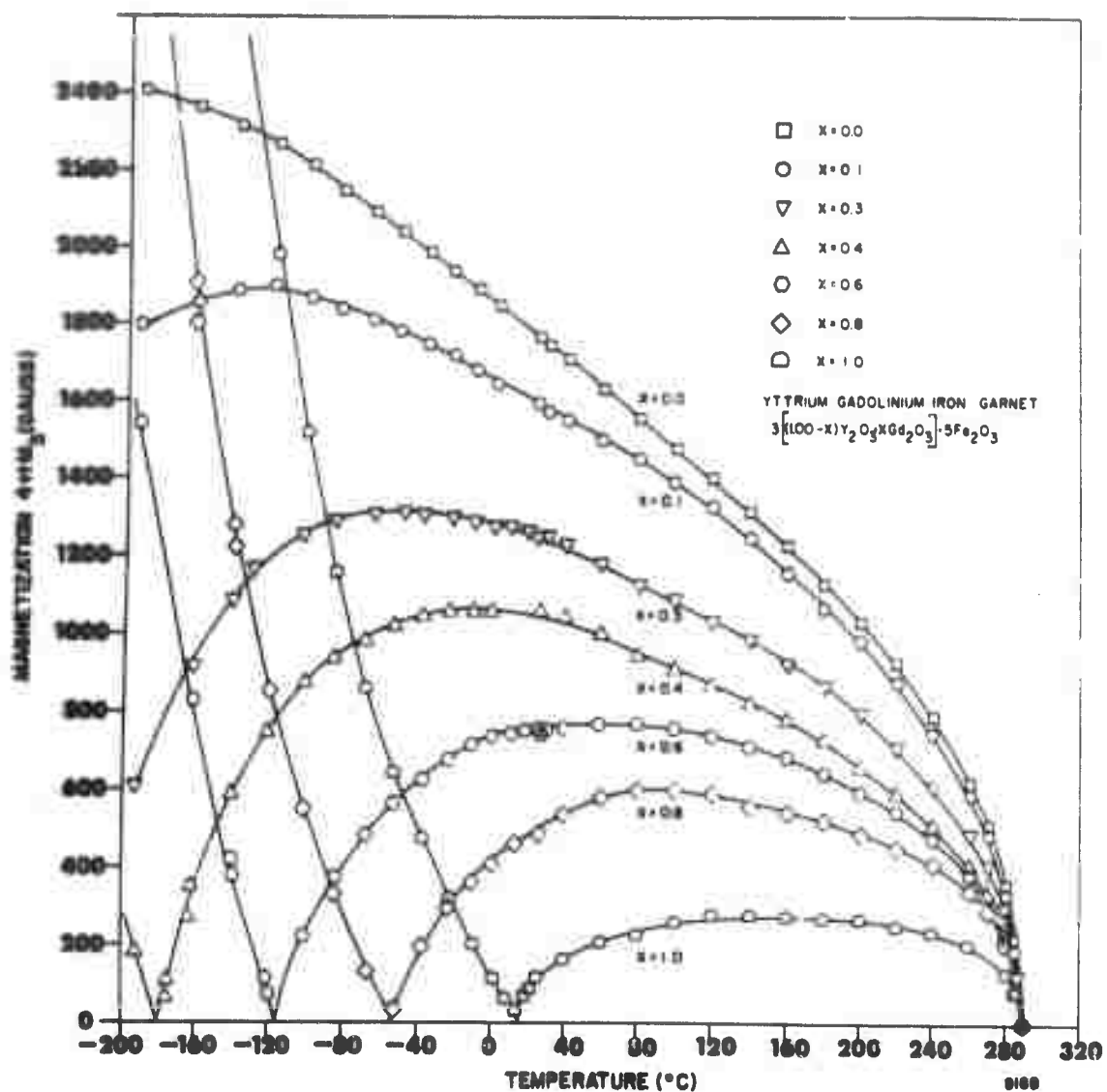


Figure 31. Variation of the Saturation Magnetization with Temperature for Yttrium Gadolinium Iron Garnet

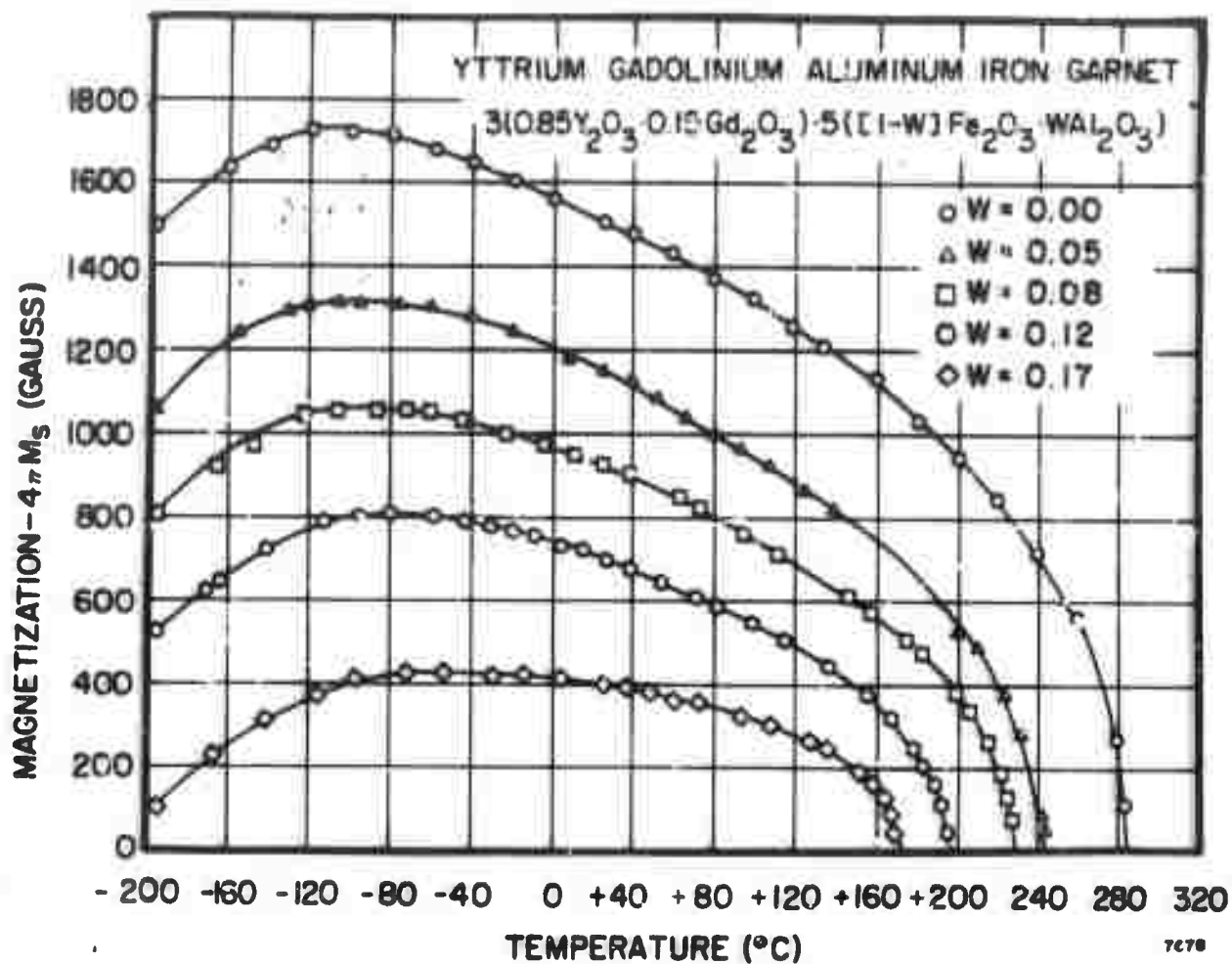


Figure 32. The Variation of Saturation Magnetization with Temperature for Aluminum Substituted 85% YIG · 15% GdIG

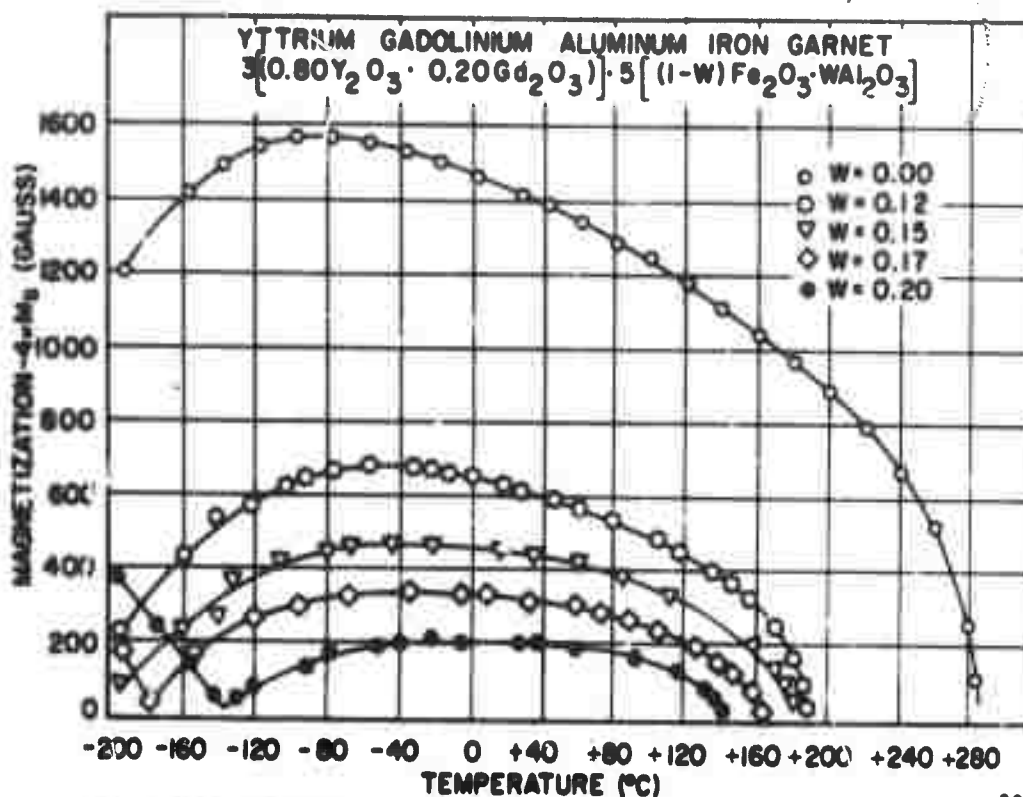


Figure 33. Variation of Saturation Magnetization with Temperature for Aluminum Substituted 80% YIG 20% GdIG

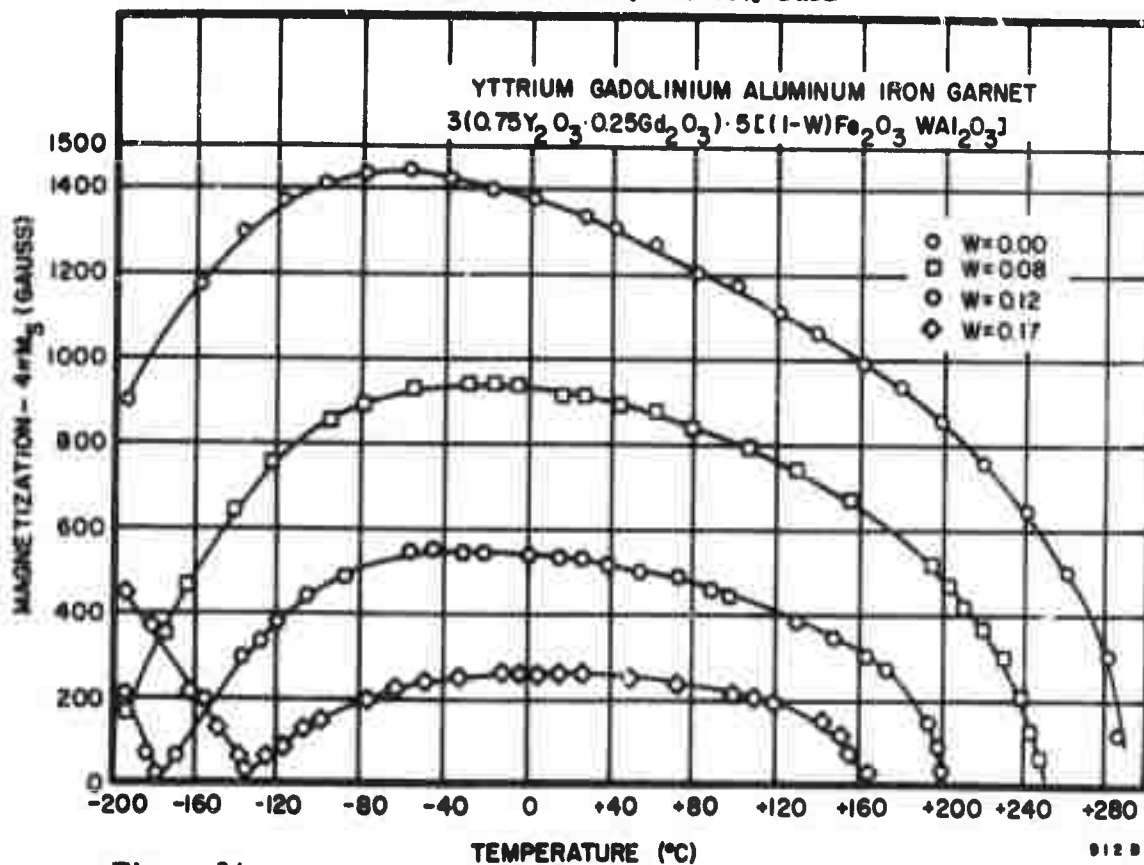


Figure 34. Variation of Saturation Magnetization with Temperature for Aluminum Substituted 75% YIG 25% GdIG

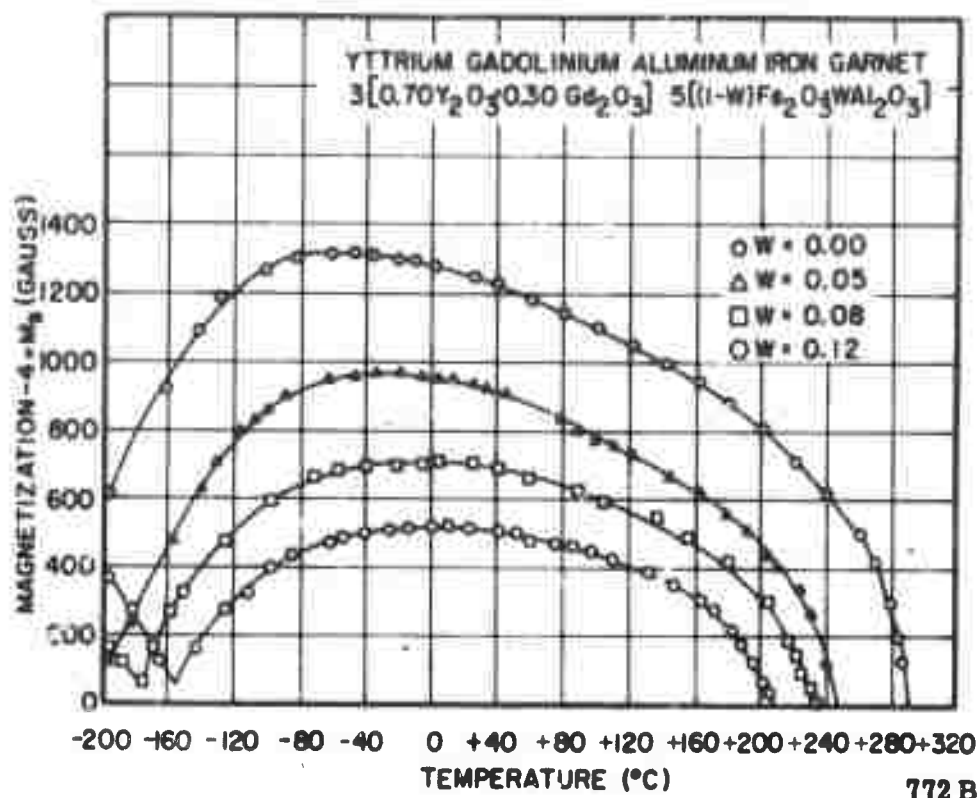


Figure 35. Variation of Saturation Magnetization with Temperature for Aluminum Substituted 70% YIG 30% GdIG

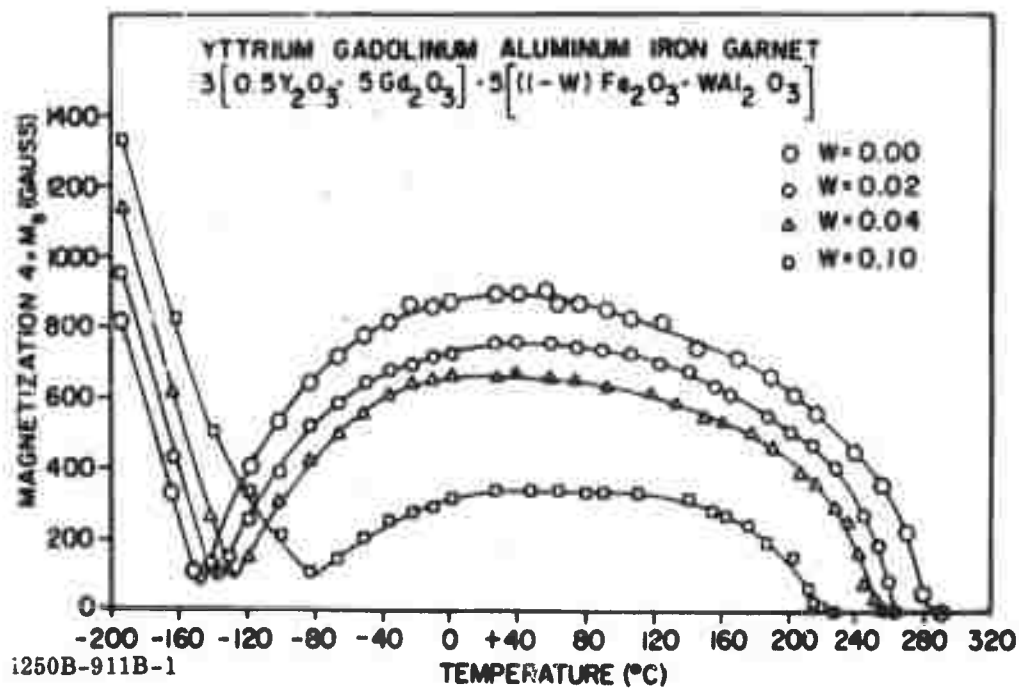


Figure 36. Variation of Saturation Magnetization with Temperature for Aluminum Substituted 50% YIG 50% GdIG

4.5 EVALUATION OF MATERIALS BY ANALYSIS AND MEASUREMENT OF DEVICE CHARACTERISTICS

Whether or not a given ferrite is satisfactory for a specified phase shifter application must ultimately be decided in the light of the performance characteristics required of the phase shifter. A true correlation of intrinsic ferrite properties with device performance is highly desirable and the ultimate goal of this study is to be able to take a device performance specification and accurately predict the required intrinsic material parameters (and, hence, select the appropriate ferrite).

To study the relationship of dimensional and material parameters to the performance characteristics of FDPS a computer-aided analysis of the exact boundary value problem has been carried out for several phase shifter configurations. The solution to each boundary value problem yields the differential phase shift and loss characteristics for the appropriate configuration. This analysis has been supported and guided by an extensive set of experimental measurements on a variety of FDPS configurations and a wide array of material parameters. The propagation constant equation for each configuration was established utilizing the analysis techniques outlined in Section 3.3. The magnetic properties of the ferrite were represented via the "averaged" tensor permeability developed in Section 3.2.1. Numerical computations were carried out on a digital computer.

The correlation obtained between experimental data and calculated values of both magnetic loss and phase shift has permitted the development of a rather complete picture of the mechanisms and phenomena involved in the operation of FDPS. Optimum device configurations have been developed for the materials used. These configurations provide a maximum figure of merit in terms of differential phase shift per unit loss. The ability to calculate meaningful numbers with a high degree of accuracy permits the practical design of a device with a minimum of the cut and try measures usually necessary.

4.5.1 Low Power Characteristics of Waveguide FDPS

The nonreciprocal waveguide FDPS is the device on which both experimental and analytical studies have been concentrated. A cutaway view of a laboratory model phase shifter is shown in Figure 37. The phase shift element is a single ferrite toroid

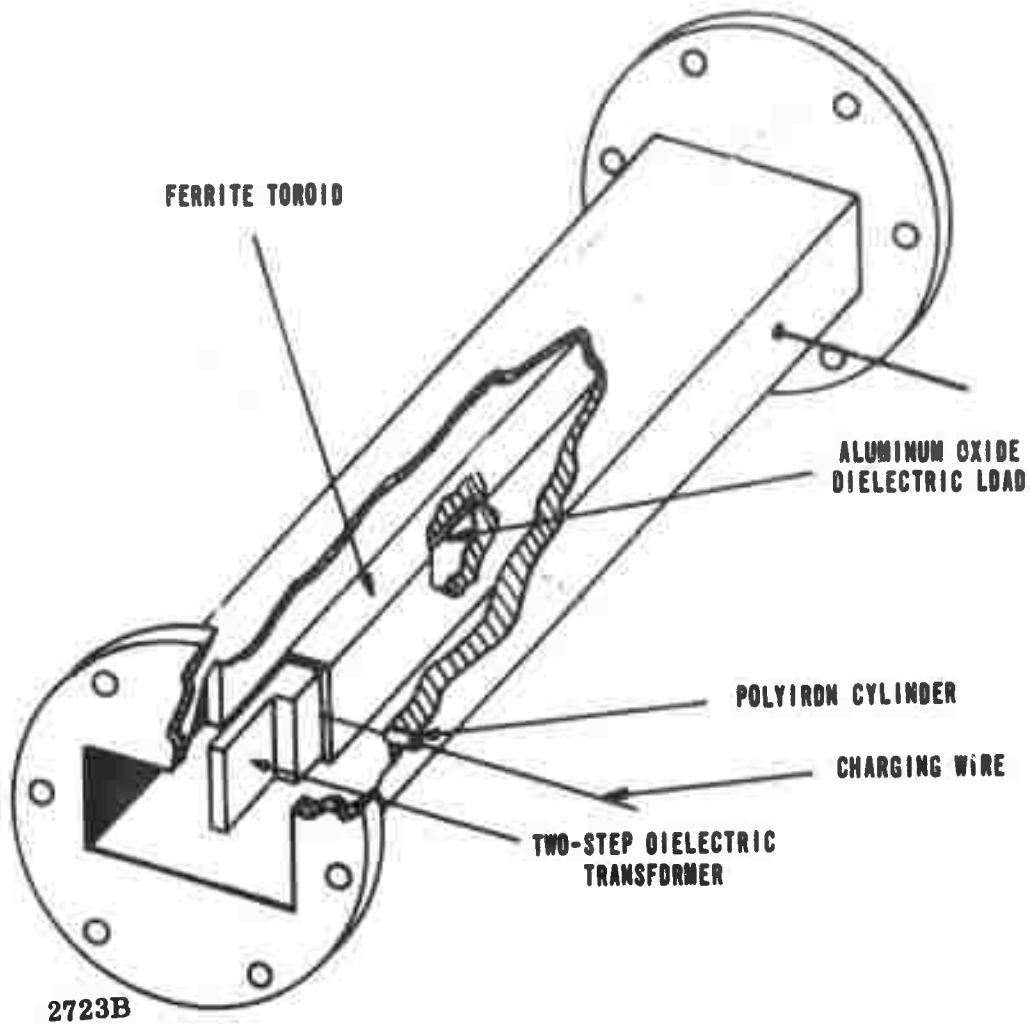


Figure 37. Cutway Illustration of a Typical Nonreciprocal Digital Phase Shifter Structure

contained wholly within the waveguide. Two-step dielectric transformers were used for matching into the ferrite-loaded section of waveguide. A single turn of wire coaxial to the toroid provides a path for the current pulses which magnetize the ferrite to either of two remanent magnetization states ($+M_r$ or $-M_r$).

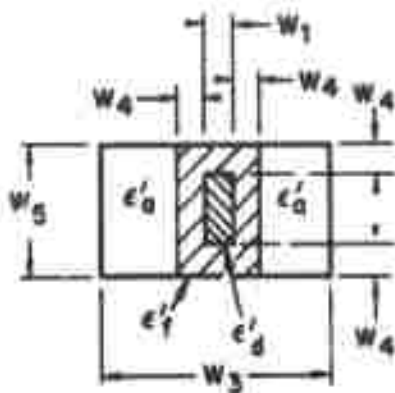
A simplified cross-sectional view of the phase shifter of Figure 37 is shown in Figure 38. As discussed in Section 3.2.3, in the normal operational mode of this phase shifter (i.e., the fundamental TE mode), the rf magnetic field is entirely in the plane parallel to the top and bottom of the waveguide. The magnetization in the top and bottom "crossbars" of the toroid is principally in the direction parallel to the top and bottom of the waveguide, while in the vertical legs the magnetization tends to be perpendicular to that direction. To first order, when the incident rf magnetic field and the direction of magnetization of a sample are mutually parallel, there is no

interaction between the field and the magnetization. Therefore, the crossbars of the toroid "look" approximately like pieces of dielectric to the incident rf field. In the vertical legs the magnetization is normal to the rf magnetic field and a strong interaction takes place. From these observations, it is apparent that the single toroid latching phase shifter can be represented by the twin slab model shown in Figure 39. When the dielectric core and the ferrite toroid of the practical device have the same dielectric constant, that value is, of course, used for the dielectric constant of the dielectric load of the model. If the dielectric constants of the dielectric core and the ferrite are different, an "effective" dielectric constant is used for the dielectric load of the model. A simple procedure for computing the effective values of dielectric constant and dielectric loss tangent which leads to quite accurate results is to use volume ratios. That is

$$\epsilon'_{\text{effective}} = \epsilon'_f \left(\frac{2W_4}{W_5} \right) + \epsilon'_d \left(\frac{W_5 - 2W_4}{W_5} \right)$$

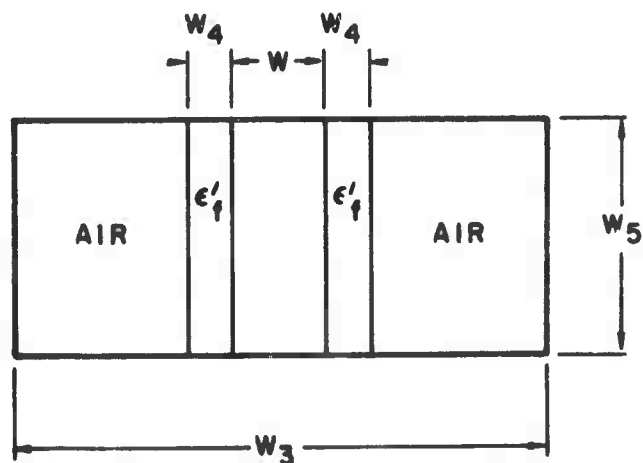
$$\tan \delta_{\text{effective}} = \tan \delta \left(\frac{2W_4}{W_5} \right) + \tan \left(\frac{W_5 - 2W_4}{W_5} \right)$$

The propagation constant equation for the twin slab model of Figure 39 is given as equation 27 in Section 3.2.1. This equation has been solved numerically with the aid of a digital computer. The numerical solutions for a number of interesting situations are presented below with corroborating experimental data. Both the theoretical and the experimental data are presented in normalized form. Physical dimensions are normalized with respect to the free space wavelength at the center operating frequency. Frequency and the frequency equivalents of static magnetic fields and of remanence and saturation magnetizations are normalized with respect to the center operating frequency. Differential phase shift is given in degrees per GHz-cm. To unnormalize this quantity with respect to frequency, multiply by the center frequency in GHz. Losses are given either as decibels per 360° of differential phase shift or decibels per centimeter.



3862B

Figure 38. An Internal Toroid Latching Phase Shifter



3863B

Figure 39. Twin Slab Model

The parameters used in the numerical analysis are

$$\omega_c = 2\pi f_c = \text{center frequency}$$

$$\omega = 2\pi f = \text{operating frequency}$$

$$M_s = \frac{\gamma 4\pi M_s}{\omega_c} = \text{normalized saturation magnetization}$$

$$M_r = \frac{\gamma 4\pi M_r}{\omega_c} = \text{normalized remanent magnetization}$$

$$TC = \frac{\gamma \Delta H}{\omega_c} = \text{time constant}$$

$$R_r = \frac{4\pi M_r}{4\pi M_s} = \text{remanence ratio}$$

$$FR = \frac{f}{f_c} = \text{frequency ratio}$$

$$4\pi M_s = \text{saturation magnetization}$$

$$4\pi M_r = \text{remanence magnetization}$$

$$\gamma = \text{gyromagnetic ratio}$$

$$\Delta H = \text{intrinsic linewidth}$$

Dielectric constants ϵ'_a , ϵ'_d and ϵ'_f , dielectric loss tangents $\tan \delta_a$, $\tan \delta_d$, and $\tan \delta_f$ apply to the air, dielectric and ferrite regions, respectively. Normalized dimensions W_1 , W_3 , W_4 and W_5 apply to the slot width, waveguide width, toroid wall thickness and waveguide height respectively.

Because the digital phase shifter operates in a remanence state, the effective internal field H_1 is determined entirely by the magnetocrystalline anisotropy field and the rf demagnetizing factors of the domain within the toroid. To establish a reasonable value for H_1 requires some understanding of the domain structure of the material. For material geometries which lead to an appreciable remanence ratio (0.5 or greater), the domain structure of the ferrite will most likely consist of a few large domains and some smaller domains in "unmagnetized" parts of the material. Each domain may have different demagnetizing factors, and in each domain the magnetization will exhibit precessional resonance at a characteristic frequency determined by the anisotropy field of the material and the demagnetizing fields.

It is important to observe that, although the rf demagnetizing factors at the surfaces of the ferrite are accounted for by the applied boundary conditions in the solution of the boundary value problems, the rf demagnetizing factors of the various internal domains are not included by that procedure and must be accounted for in the average effective field H_i . In this model, the major portion of the resonance losses will be determined by the effective field of the largest domains whose magnetizations are oriented orthogonal to the rf magnetic field. The geometry of these major domains should be related to the overall sample dimensions.

Based on this thought, H_i can be estimated using Kittel's equation and the estimated demagnetizing factors of the major domain. Because the applied dc magnetic field is identically zero Kittel's equation can be written as

$$H_i = \left[\left(N_x^a + N_x^a - N_z \right) 4\pi M_s \right] \left[\left(N_y^a + N_y^a - N_z \right) 4\pi M_s \right]^{1/2}$$

where N_x^a , N_y^a are the effective demagnetizing factors arising from anisotropy effects and are given by:

$$N_x^a = \frac{K_1}{4\pi M_s^2} \left[2 - \sin^2 \theta - 3 \sin^2 2\theta \right]$$

$$N_y^a = \frac{2K_1}{4\pi M_s^2} \left[1 - 2 \sin^2 \theta - \frac{3}{8} \sin^2 2\theta \right]$$

Here θ is the angle the magnetization makes with a $\langle 100 \rangle$ direction of the crystallites as measured in a $\langle 110 \rangle$ plane. If the magnetization is assumed to lie along the easy direction of a negative anisotropy material, the resonance equation reduces to:

$$H_i = \left[\left(\frac{4}{3} \frac{K_1}{M_s} + N_x 4\pi M_s \right) \left(\frac{4}{3} \frac{K_1}{M_s} + N_y 4\pi M_s \right) \right]^{1/2}$$

where N_z has been set equal to zero in accordance with the toroidal geometry.

The parameter K_1 is the first order magnetocrystalline anisotropy constant.

For a typical garnet toroid with $\frac{K_1}{M_s} \approx 60$ oe., $4\pi M_s = 1200$ gauss, and a length to width ratio of 10 to 1 for the toroid legs, the estimated effective field for the major domain is

$$H_1 = \sqrt{(80 + 120)(80 + 1080)}$$

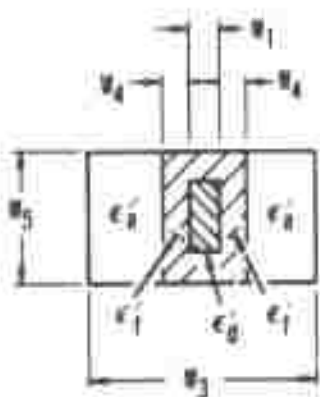
$$H_1 \approx 480 \text{ oe.}$$

The damping parameter associated with these domain resonances is of the conventional form and is included in the resonance equation in normalized form as a damping time constant

$$TC \sim \frac{\gamma \Delta H}{f_c},$$

where ΔH is the intrinsic linewidth and f_c is the center operating frequency. Since the intrinsic linewidth appears to vary directly with frequency (as will be discussed later), the damping term is in fact a constant independent of frequency, and the calculated results are applicable at any frequency.

4.5.1.1 Effects of Internal Field and Magnetization on Phase Shifter Performance. The experimental data, used in plotting the various curves which follow, are presented in Tables V and VI of this report and Tables XII and XIV of the Final Report on RADC Contract No. AF-30(602)-3490. In Figures 40 and 41, the theoretical differential phase shift and loss per 360° of differential phase shift for a latching phase shifter are shown for three different values of the normalized effective internal field as functions of the width of the waveguide. In addition, the experimentally observed loss and differential phase shift for the same structure are given. It is encouraging to note that as the effective field approaches the value predicted by the simple arguments given above, both the predicted loss and differential phase shift for the structure approach the observed values more closely. The theoretical predictions and the experimental results are in fact in excellent agreement. Figures 42 and 43 illustrate the effect on loss and differential phase shift of variations in H over a small range of values when all other parameters are fixed. It can be seen that loss increases more rapidly than differential phase shift as H_1 increases.



$$m_s = \frac{\gamma 4\pi M_s}{\omega_c} = 0.38$$

$$f_c = 9 \text{ GC}$$

$$m = \frac{\gamma 4\pi M_f}{\omega_c} = 0.19$$

$$FR = 1.0$$

$$w_1 = 0.023 \lambda_c$$

$$w_3 = \text{VARIABLE}$$

$$w_4 = 0.04 \lambda_c$$

$$w_5 = 0.294 \lambda_c$$

$$R_f = 0.5$$

$$\epsilon'_s = 1.0$$

$$\epsilon'_d = 16.0$$

$$\epsilon'_f = 16.0$$

$$\tan \delta_s = 0$$

$$\tan \delta_d = 0.0005$$

$$\tan \delta_f = 0.0007$$

$$\lambda_c = 3.33 \text{ cm}$$

$$HF = \text{PARAMETER}$$

$$\Delta H = 65 \text{ Oe.}$$

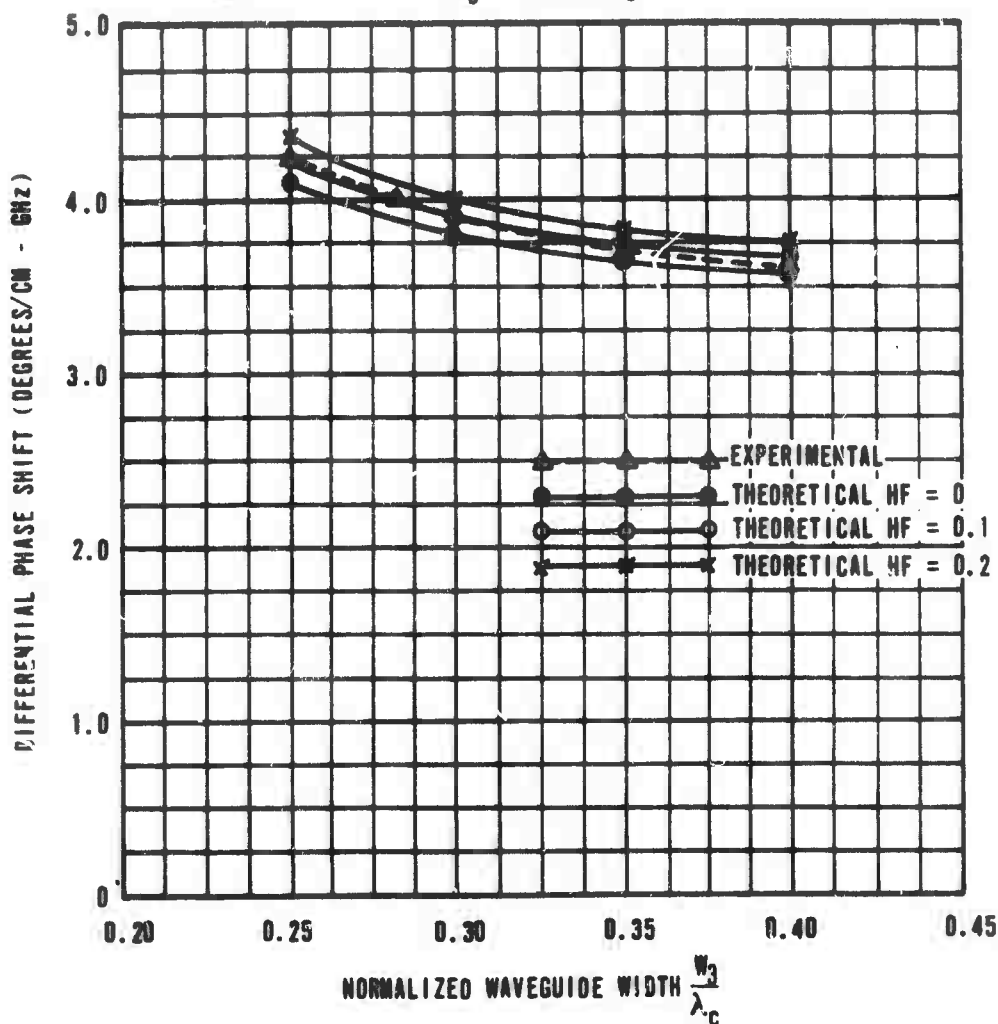
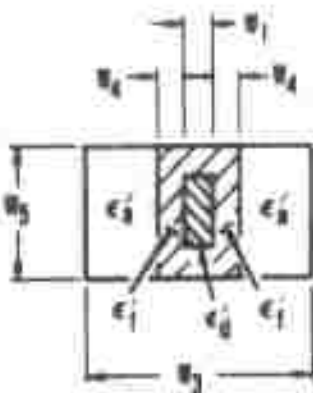


Figure 40. Differential Phase Shift vs Normalized Waveguide Width For A Latching Phase Shifter With Effective Internal Field As A Parameter



$$m_s = \frac{\gamma_4 \pi w_s}{\omega_c} = 0.38$$

$$f_c = 2 \text{ Gc}$$

$$m = \frac{\gamma_4 \pi w_r}{\omega_c} = 0.19$$

$$FR = 1.0$$

$$w_1 = 0.023 \lambda_c$$

$$w_3 = \text{VARIABLE}$$

$$w_4 = 0.04 \lambda_c$$

$$w_5 = 0.294 \lambda_c$$

$$R_r = 0.5$$

$$\epsilon_s = 1.0$$

$$\epsilon_d = 18.0$$

$$\epsilon_f = 18.0$$

$$\tan \delta_s = 0$$

$$\tan \delta_d = 0.0005$$

$$\tan \delta_f = 0.0007$$

$$\lambda_c = 3.33 \text{ cm}$$

$$HF = \text{PARAMETER}$$

$$\Delta H = 85 \text{ Oe.}$$

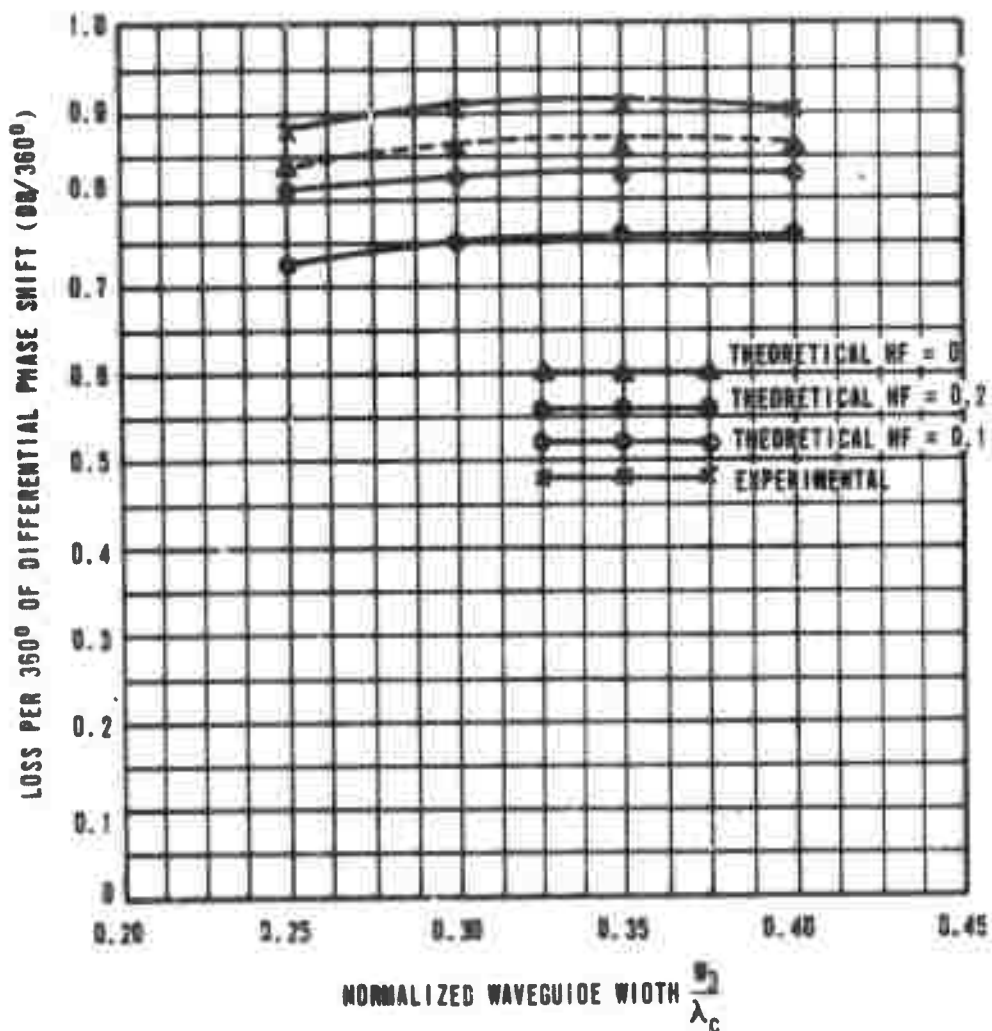


Figure 41. Loss Per 360° Of Differential Phase Shift vs Normalized Waveguide Width For A Latching Phase Shifter With Effective Internal Field As A Parameter

TABLE V. C-BAND AND S

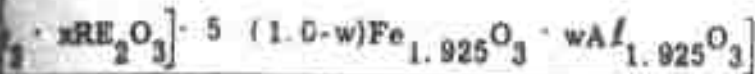
$$3 \left[(1.0-x) Y_2 O_3 \right]$$

SHEET NO.	COMPOSITION		BATCH SIZE	WAXING TIME (HRS)	FIRING SCHEDULE °C/hr	DENSITY (g/cc)	PARTICLE SIZE (microns)	DILUTION
G-260-5H		0.25	757	16	1500 5	4.82	NM	0.
G-293-5D		0.15	1412	16	1475 5	4.84	NM	0.
G-455-C	0.10 Dy	0.12	755	16	1475 5	5.14	NM	0.
G-454-C	0.04 Dy	0.12	757	16	1475 5	5.06	NM	0.
G-292-2D		0.12	1420	16	1475 5	4.91	NM	0.
G-453-D	0.02 Dy	0.12	752	16	1475 5	5.07	NM	0.
G-452-E	0.45 Gd		753	16	1475 5	5.74	NM	0.
G-451-C	0.04 Dy		749	16	1475 5	5.72	NM	0.
G-287-6C	0.45 Gd		745	16	1475 5	5.69	NM	0.
G-291-2D		0.08	1431	16	1475 5	5.00	NM	0.
G-387-2A	0.30 Gd		750	16	1475 5	5.45	NM	0.
G-404-3D	0.01 Dy		1440	16	1475 5	5.08	NM	0.
G-232-73D		0.05	1454	24	1475 5	5.10	NM	0.
G-250-5B		0.25	757	16	1500 5	4.82	NM	0.
G-457-C	0.02 Dy	0.15	748	16	1475 5	5.02	NM	0.
G-461-C	0.45 Gd	0.06	755	16	1475 5	5.64	NM	0.
G-459-C	0.02 Dy	0.15	766	16	1475 5	5.06	NM	0.
G-462-C	0.45 Gd	0.06	752	16	1475 5	5.69	NM	0.
G-460-C	0.04 Dy	0.06	751	16	1475 5	5.63	NM	0.
G-456-C	0.45 Gd	0.06	754	16	1475 5	5.60	NM	0.
G-293-5E		0.15	1412	16	1475 5	4.84	NM	0.
G-292-2E		0.12	1420	16	1475 5	4.91	NM	0.
G-291-2E		0.08	1431	16	1475 5	5.00	NM	0.
G-404-3E		0.05	1440	16	1475 5	5.08	NM	0.

A

J04002

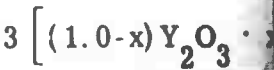
BAND DEVICE TEST RESULTS ON MATERIALS FROM THE FAMILY



LINE NO.	DIELECTRIC CONSTANT (ε BAND)	ε FACTOR	LINE WIDTH (μm) ε BAND	ΔT (K) (CAUSE)	z _c	COHERENT FIELD E _c (V) (Å ⁻¹)	$\frac{E_{\text{coh}}}{E_g}$	P _{STT} (W)	h _{STT} (Å)	1000 T _{90%} (K)	ΔH (mK)
0005	14.1	2.03	36	208	0.71	1.11	0.10	>400	>110	2.50	10
0005	14.3	2.03	42	640	0.55	1.76	0.31	>400	>110	0.82	37
0006	15.4	NM	461	768	0.68	1.42	0.38	>400	>110	5.00 3.50	33
0006	15.3	NM	192	815	0.68	0.85	0.40	>400	>110	2.65 2.20	43
0006	14.7	NM	47	830	0.58	1.76	0.41	NM		0.73	41
0011	15.5	NM	77	860	0.63	0.88	0.43	100	55.2	1.30 1.10	45
0000	15.4	1.94	375	825	0.42	1.24	0.46	>400	>110	3.80 3.07	49
0014	16.3	1.99	192	970	0.67	0.99	0.48	250	87	4.40 3.80	51
0006	16.2	NM	100	980	0.63	1.54	0.49	25	26	1.60 1.50	48
0005	15.3	2.02	55	1115	0.60	1.18	0.56	NM		0.62	53
1	NM	NM	75	1250	0.63	0.90	0.62	46	48	1.40 1.15	68
0006	15.5	2.02	55	1325	0.55	1.29	0.66	NM		0.46	78
0005	16.0	NM	40	1780	0.72	0.41	0.88	NM		0.43	97
0005	14.1	2.03	36	208	0.58	0.88	0.10	>300	>63	1.74	14
0018	15.8	1.95	138	560	0.18	0.67	0.42	>300	>63	5.00 3.60	50
0005	15.9	1.97	296	570	0.58	1.73	0.43	>300	>63	3.50 2.40	35
0006	14.8	1.80	470	572	0.59	1.25	0.43	>300	>63	5.75 3.90	31
0005	16.1	1.91	412	575	0.38	1.67	0.44	>300	>63	3.95 2.73	47
0004	16.1	NM	120	600	0.50	1.51	0.45	110	38	1.70 1.28	43
0005	15.1	1.91	212	625	0.67	1.05	0.47	>300	>63	3.15 2.30	34
0005	14.3	2.03	42	840	0.43	1.43	0.48	10	11	0.62	46
0005	14.7	NM	47	900	0.38	1.37	0.68	6	9	0.46	64
0005	15.3	2.02	55	1115	0.51	0.87	0.91	3	6	0.51	70
0007	15.5	2.02	55	1525	0.45	0.93	1.00	NM		NM	NM

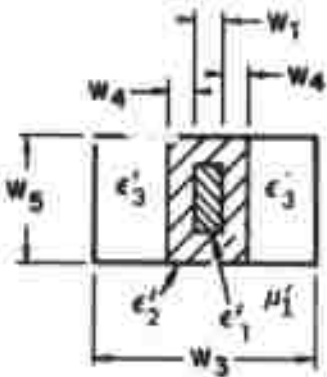
B

TABLE V. X-BAND DEVICE



SMEC NO.	COMPOSITION		BATCH SIZE (gms)	WAXING TIME (HRS)	FIRING SCHEDULE °C/hr	DENSITY gms/cm ³	PARTICLE SIZE (MICRONS)	DIELECTRIC LOSS TAN (X BAND)
G-293-5C		0.15	1412	16	1475 / 5	4.84	NM	<0.0005
G-292-2C		0.12	1420	16	1475 / 5	4.91	NM	<0.0005
G-450-C	0.10 Dy	0.08	753	16	1475 / 5	5.23	NM	0.0007
G-297-7F	0.45 Gd		745	16	1475 / 5	5.69	NM	0.0008
G-287-3C	0.04 Dy	0.08	751	16	1475 / 5	5.13	NM	0.0004
G-286-7C	0.02 Dy	0.08	750	16	1475 / 5	5.07	NM	<0.0005
G-296-41J	0.30 Gd		3111	24	1475 / 5	5.47	NM	<0.0005
G-404-3C		0.05	1440	16	1475 / 5	5.08	NM	<0.0005
G-232-73C			1454	24	1475 / 5	5.10	NM	<0.0005

- 1 - Estimated Value
- 2 - Normalized to $R_r = 0.50$
- 3 - Value calculated by method shown in Appendix A

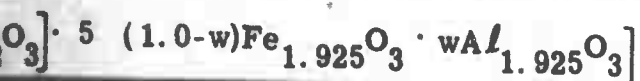


3862B

$$\begin{aligned} W_1 &= 0.060 \lambda_c & \epsilon'_1 &= 16 \\ W_3 &= 0.382 \lambda_c & \epsilon'_2 &= \epsilon'_F \\ W_4 &= 0.040 \lambda_c & \epsilon'_3 &= 1 \\ W_5 &= 0.294 \lambda_c & m_s &= \gamma 4 \pi \epsilon'_1 \\ \mu'_1 &= 1 & m_p &= \gamma 4 \pi \epsilon'_1 \end{aligned}$$

A

TEST RESULTS ON MATERIALS FROM THE FAMILY



LINE FREQ MHz	WAVELENGTH cm	LINE WIDTH MHz	SWR (dB)	f_c	COLLECTIVE FIELD mV/cm (100°)	$\frac{P_{max}}{P_0}$	P_{max} (dBm)	P_{max}^2 (dBm)	LOSS COEFF. α	LOSS COEFF. β
3	2.03	42	640	0.48	1.27	0.19	>150	>113	1.17	39
7	NM	47	200	0.38	1.21	0.27	>150	>113	0.68	57
7	NM	379	850	0.55	0.93	0.39	>150	>113	4.10	45
2	NM	100	280	0.60	0.94	0.31	55	68	1.55	53
7	NM	163	1120	0.57	0.79	0.33	>150	>113	1.72	54
4	NM	99	1100	0.60	0.61	0.33	>150	>113	1.30	58
1	2.02	60	1240	0.53	0.90	0.36	42	60	1.15	68
5	2.02	55	1325	0.40	0.85	0.40	5	21	0.52	87
0	NM	NM	1280	0.64	0.49	0.53	2	12	0.55	106

f_c = the center frequency of the low power test range
 = 3.7 GHz, 5.65 GHz and 9.0 GHz at S band, C band and X band respectively

f_p = high power test frequencies
 = 3.7 GHz, 5.60 GHz and 9.375 GHz at S band, C band and X band respectively

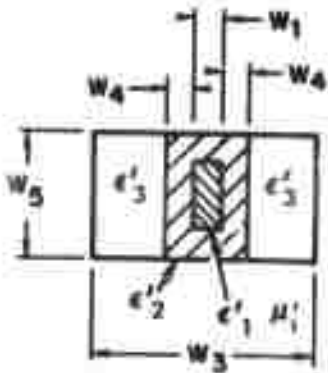
B

TABLE VI. X

SMEC NO.	COMPOSITION	BATCH SIZE (gms)	WAXING TIME (HRS)	FIRING SCHEDULE °C/hr	DENSITY gms/cm ³	PARTICLE SIZE (MICRONS)	
16-20F	Ni _{1.0} Mn _{0.02} Fe _{1.9} O ₄	1700	4	1400 / 7	4.86	NM	
78-4F	Ni _{0.97} Zn _{0.03} Mn _{0.02} Fe _{1.9} O ₄	1700	4	1275 / 7	4.92	NM	
77-3F	Ni _{0.824} Zn _{0.176} Mn _{0.02} Fe _{1.9} O ₄	1750	4	1275 / 7	5.02	NM	
61-4F	Ni _{0.325} Zn _{0.675} Mn _{0.02} Fe _{1.9} O ₄	1750	4	1250 / 7	5.13	NM	
83-8F	0.58MgO · 0.06MnO · 0.36Fe ₂ O ₃	1750	4	1320 / 7	4.20	NM	
64-4E	Li _{1.0} Fe ₅ O	1750	4	1250 / 7	4.34	NM	>0
91-3F	Ni _{0.44} Zn _{0.56} Mn _{0.02} Fe _{1.9} O ₄	2800	4	1250 / 7	5.04	NM	

TABLE VI. C

SMEC NO.	COMPOSITION	BATCH SIZE (gms)	WAXING TIME (HRS)	FIRING SCHEDULE °C/hr	DENSITY gms/cm ³	PARTICLE SIZE (MICRONS)	
16-20F	Ni _{1.0} Mn _{0.02} Fe _{1.9} O ₄	1700	4	1400 / 7	4.86	NM	
78-4F	Ni _{0.97} Zn _{0.03} Mn _{0.02} Fe _{1.9} O ₄	1700	4	1275 / 7	4.92	NM	
77-3F	Ni _{0.824} Zn _{0.176} Mn _{0.02} Fe _{1.9} O ₄	1750	4	1275 / 7	5.02	NM	
61-4F	Ni _{0.325} Zn _{0.675} Mn _{0.02} Fe _{1.9} O ₄	1750	4	1250 / 7	5.13	NM	
83-8F	0.58 MgO · 0.06MnO · 0.36Fe ₂ O ₃	1750	4	1320 / 7	4.20	NM	
64-4E	Li _{1.0} Fe ₅ O ₈	1750	4	1250 / 7	4.34	NM	>0
91-3F	Ni _{0.44} Zn _{0.56} Mn _{0.02} Fe _{1.9} O ₄	2800	4	1250 / 7	5.04	NM	



3862B-1

$$W_1 = 0.025\lambda_c$$

$$W_3 = 0.365\lambda_c$$

$$W_4 = 0.045\lambda_c$$

$$W_5 = 0.280\lambda_c$$

$$\mu'_1 = 1$$

$$\epsilon'_1 = 16$$

$$\epsilon'_2 = f$$

$$\epsilon'_3 = 1$$

$$m_s = 74\pi$$

$$m_p = 74\pi$$

004002

A

AND (8.0-10.0 Ghz) DEVICE TEST RESULTS

RIC (AN. SD)	DIELECTRIC CONSTANT (X BAND)	Q FACTOR	LINE WIDTH ΔN (mil) X BAND	477 Ms (GAUSS)	μ_r	COERCIVE FIELD H_c (OE) (60~)	$\frac{75ms}{F_o}$	P_{crit} (mW)	h_{crit}^* (OE)	LOSS/360°	Δφ/INCH
0	12.6	2.44	520	2815	0.48	NM	0.88	NM	NM	>10 db	
6	12.7	2.38	486	2965	0.57	NM	0.92	NM	NM	8.0 to 10.0 Ghz	
5	13.2	2.27	270	3820	0.65	NM	1.19	NM	NM	>10 db	
1	14.9	2.07	107	2770	0.37	NM	0.86	17	18	8.0 to 10.0 Ghz	
1	12.9	2.13	512	2065	0.67	NM	0.64	3	8	NM	NM
	NM	2.23	595	3365	0.65	NM	1.50	NM	NM	See fig	
16	13.7	2.13	115	3770	0.67	NM	1.17	NM	NM	0.57	101
										>30 db	
										8.0 to 10.0 Ghz	
										>30 db	
										8.0 to 10.0 Ghz	

AND (5.0-6.5 Ghz) DEVICE TEST RESULTS

RIC (AN. SD)	DIELECTRIC CONSTANT (X BAND)	Q FACTOR	LINE WIDTH ΔN (mil) X BAND	477 Ms (GAUSS)	μ_r	COERCIVE FIELD H_c (OE) (60~)	$\frac{75ms}{F_o}$	P_{crit} (mW)	h_{crit}^* (OE)	LOSS/360°	Δφ/INCH
0	12.6	2.44	520	2815	0.44	NM	1.40	NM	NM	>30 db	
3	12.7	2.38	485	2965	0.47	NM	1.47	NM	NM	4.5 to 6.5 Ghz	
5	13.2	2.27	270	3820	0.54	NM	1.90	NM	NM	>30 db	
8	14.9	2.07	107	2770	0.49	NM	1.38	NM	NM	>30 db	
1	12.9	2.13	512	2065	0.66	NM	1.03	NM	NM	4.5 to 6.5 Ghz	
	NM	2.23	595	3365	0.53	NM	1.67	NM	NM	See fig	
16	13.7	2.13	115	3770	0.56	NM	1.87	NM	NM	20	115
										>30 db	
										4.5 to 6.5 Ghz	
										>30 db	
										4.5 to 6.5 Ghz	

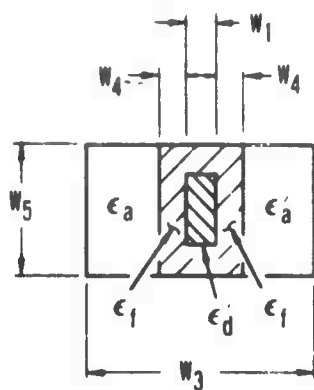
f_c = 1.35 GHz, 5.65 GHz and 9.0 GHz at L band, C band and X band

f_p = high power test frequencies

= 5.60 GHz, and 9.375 GHz at C band and X band

* Value calculated by method shown in Appendix A

B



$$m_s = \frac{\gamma 4 \pi W_s}{\omega_c} = 0.38$$

$$f_c = 9 \text{ Gc}$$

$$m = \frac{\gamma 4 \pi W_r}{\omega_c} = 0.19$$

$$FR = 1.0$$

$$W_1 = 0.023 \lambda_c$$

$$W_3 = 0.3 \lambda_c$$

$$W_4 = 0.04 \lambda_c$$

$$W_5 = 0.294 \lambda_c$$

$$R_r = 0.5$$

$$\epsilon_a = 1.0$$

$$\epsilon_d = 16.0$$

$$\epsilon_f = 16.0$$

$$\tan \delta_a = 0$$

$$\tan \delta_d = 0.0005$$

$$\tan \delta_f = 0.0007$$

$$\lambda_c = 3.33 \text{ cm}$$

$$HF = \text{VARIABLE}$$

$$\Delta H = 65 \text{ Oe.}$$

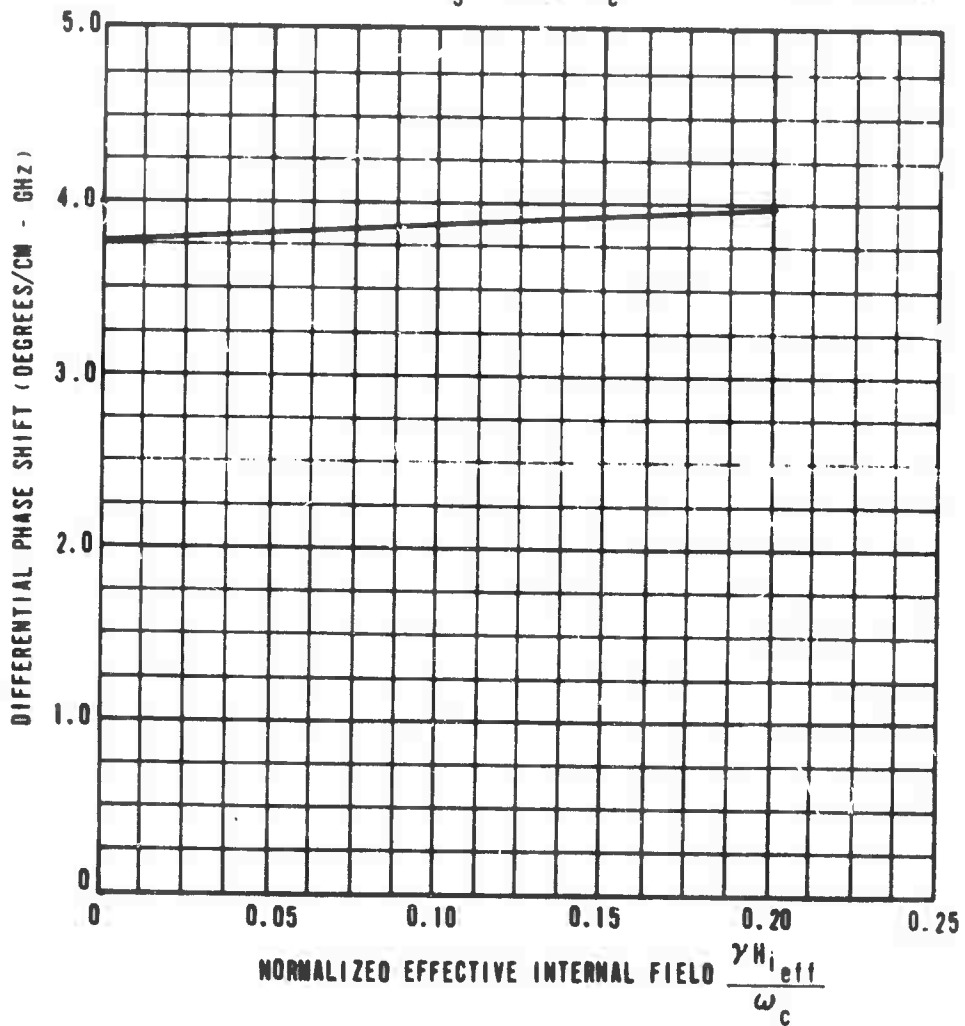
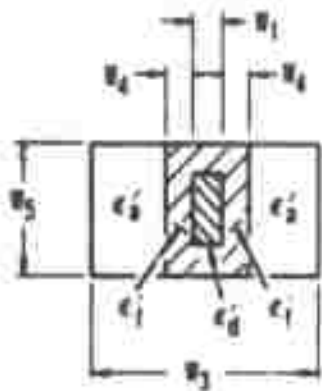


Figure 42. Differential Phase Shift vs Effective Internal Field For A Latching Phase Shifter



$$n_s = \frac{\gamma 4 \pi w_s}{\omega_c} = 0.30$$

$$f_c = 9 \text{ Gc}$$

$$n = \frac{\gamma 4 \pi w_l}{\omega_c} = 0.19$$

$$FR = 1.0$$

$$w_1 = 0.023 \lambda_c$$

$$w_3 = 0.3 \lambda_c$$

$$w_4 = 0.04 \lambda_c$$

$$w_5 = 0.294 \lambda_c$$

$$R_l = 0.5$$

$$\epsilon_s = 1.0$$

$$\epsilon_d = 16.0$$

$$\epsilon_i = 16.0$$

$$\tan \delta_s = 0$$

$$\tan \delta_d = 0.0005$$

$$\tan \delta_i = 0.0007$$

$$\lambda_c = 3.33 \text{ cm}$$

$$HF = \text{VARIABLE}$$

$$\Delta H = 65 \text{ Oe.}$$

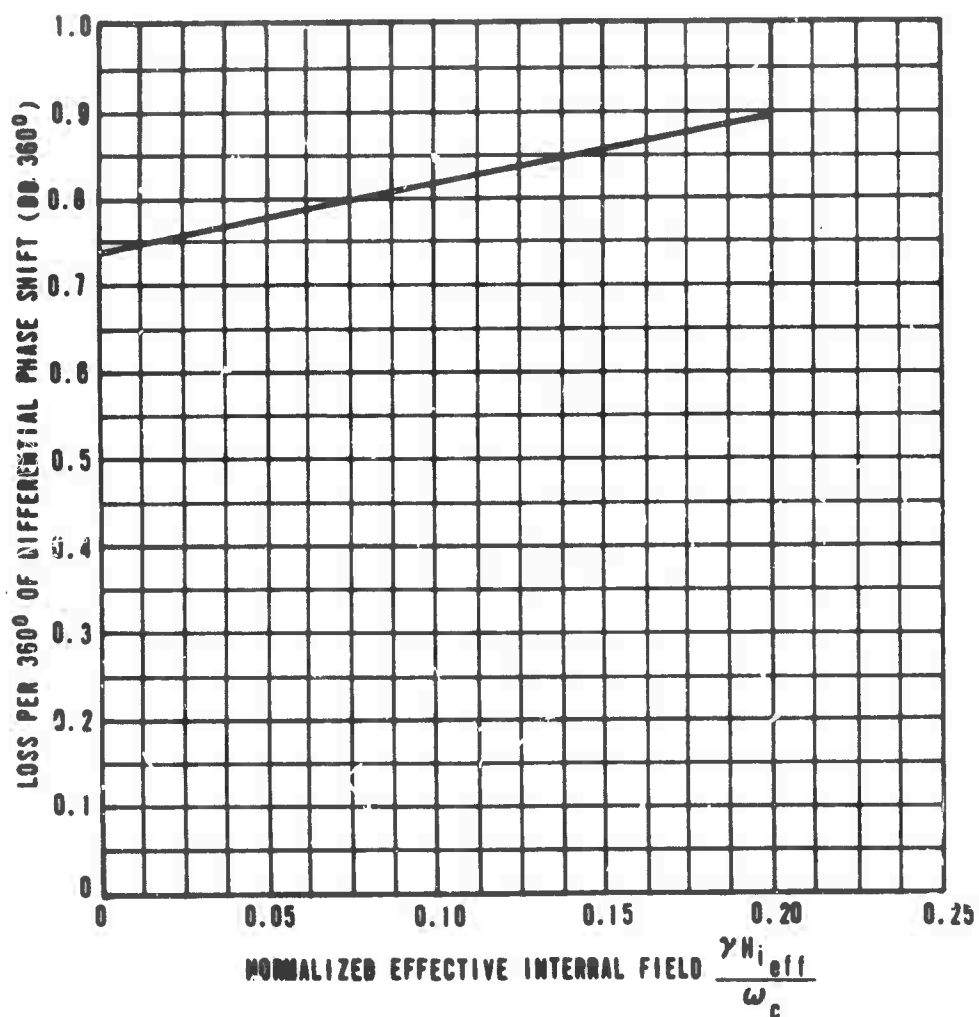
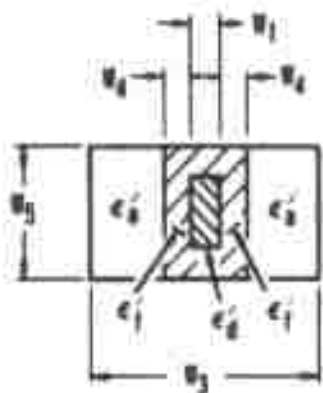


Figure 43. Loss Per 360° Of Differential Phase Shift vs Effective Internal Field For A Latching Phase Shifter

While it appears from the results shown in Figures 40 and 41 that to obtain the smallest loss per 360° of differential phase shift one would prefer a waveguide width of less than $0.25\lambda_c$, it will be shown later that for such small waveguide widths it is difficult to obtain a flat response of differential phase shift with frequency.

Figure 44 shows the calculated contributions to the total loss for three different sources -- waveguide wall losses or copper losses, dielectric losses, and theoretical magnetic losses. These add up to a total theoretical loss of approximately 0.84 db per 360° differential phase shift. This compares with approximately 0.95 db per 360° of phase shift as shown in the experimental curve for a thirty percent gadolinium substituted YIG. It is seen that the theoretical waveguide losses are approximately 0.06 db, the dielectric losses are approximately 0.22 db and the theoretical magnetic losses are approximately 0.54 db. The ability to predict accurately these various losses separately enables us not only to predict what the total loss will be but also to study the influence of the different parameters on the separate loss mechanisms. For this particular set of parameters, it would indicate that reducing the magnetic loss should be the primary goal. This would be accomplished by reducing linewidth or improving other contributors to the magnetic losses.

Figure 45 presents calculated values of loss per 360° of differential phase shift for a typical configuration as a function of the normalized saturation magnetization. The anisotropy field of the material is a parameter in this figure. These computed curves indicate that for large values of normalized saturation magnetization the loss for 360° of phase shift increases rapidly as we approach ferromagnetic resonance in the material. The proximity to ferromagnetic resonance is influenced by the value of the effective internal field and hence anisotropy field of the material. This dependence on anisotropy field is quite marked as evidence by the variation of loss with this parameter seen in the curves of Figure 45. At low values of normalized saturation magnetization loss per 360° also increases rapidly. This increase is due to the fact that the differential phase shift per unit lengths obtained for small values of m_s is low (proportional to $R_r m_s$), while the insertion loss per unit length is relatively constant, since, for low m_s values, the loss is primarily determined by dielectric and copper losses.



$$n_s = \frac{\gamma 4\pi w_s}{\omega_c} = 0.38$$

$$f_c = 9 \text{ Gc}$$

$$n = \frac{\gamma 4\pi w_f}{\omega_c} = 0.19$$

$$FR = 1.0$$

$$w_1 = 0.023 \lambda_c$$

$$w_3 = \text{VARIABLE}$$

$$w_4 = 0.04 \lambda_c$$

$$w_5 = 0.294 \lambda_c$$

$$R_f = 0.5$$

$$\epsilon'_d = 1.0$$

$$\epsilon'_d = 16.0$$

$$\epsilon'_f = 16.0$$

$$\tan \delta_d = 0$$

$$\tan \delta_d = 0.0005$$

$$\tan \delta_f = 0.0007$$

$$\lambda_c = 3.33 \text{ cm}$$

$$HF = 0.1$$

$$\Delta H = 85 \text{ Oe.}$$

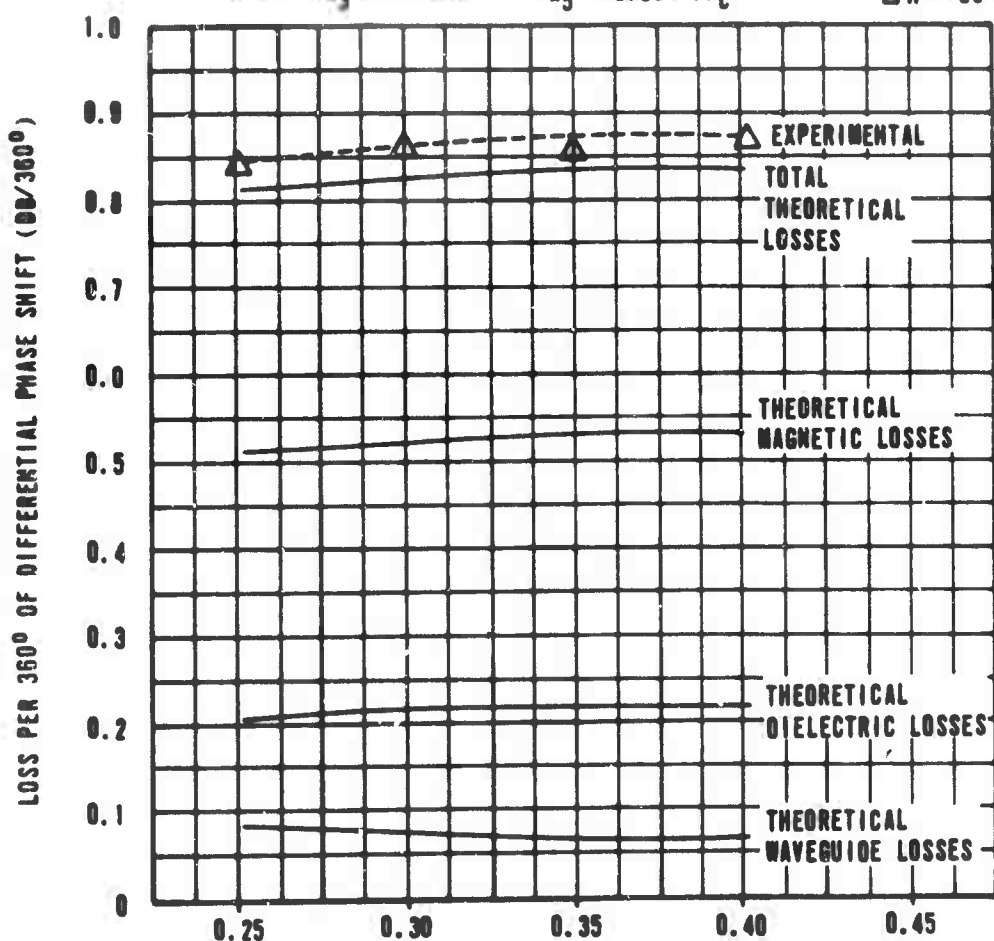
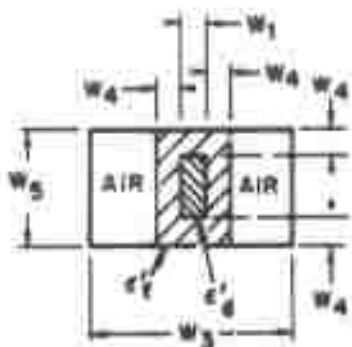


Figure 44. Separation of Losses In A Latching Phase Shifter



$m_s = \text{VARIABLE}$
 $HF = \text{FUNCTION OF } m_s \text{ \& } H_{anis}$
 $W_1 = 0.023 \lambda_c$
 $W_3 = 0.35 \lambda_c$
 $W_4 = 0.04 \lambda_c$
 $W_5 = 0.294 \lambda_c$
 $\epsilon'_d = 18.0$
 $\tan \delta_d = 0.0005$

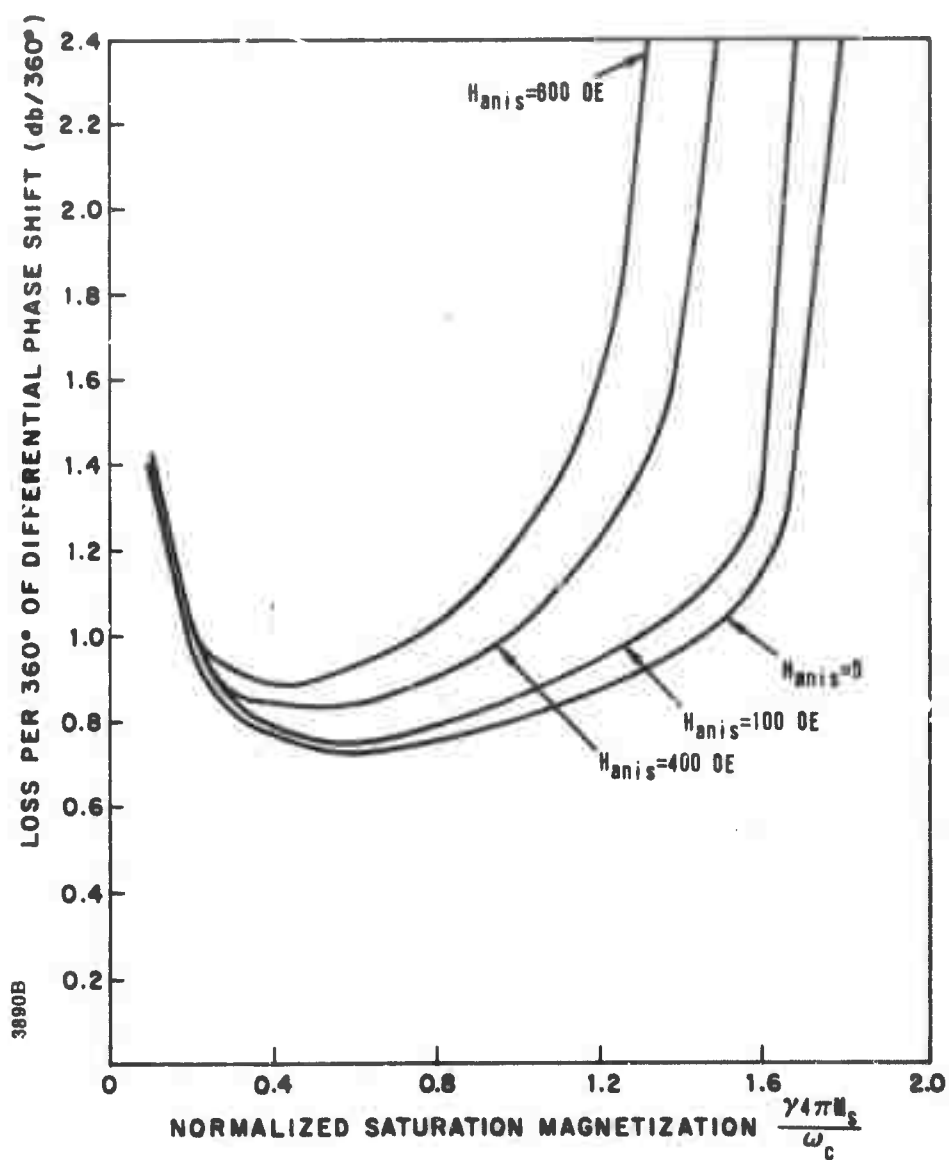


Figure 45. Loss/360° Versus Frequency Normalized Magnetization with Anisotropy Field as Parameter

Figure 46 is a plot of experimentally measured values of loss per 360° of differential phase shift as a function of the normalized saturation magnetization m_s for low m_s values. These results can be compared to the calculated curves in Figure 45. The minimum in LP360 in the vicinity of $m_s = 0.6$ agrees reasonably well with the data for the 100 oersted anisotropy field of Figure 45. The principal feature noted, i. e., the rather sharp increase in loss at normalized saturation magnetization values less than 0.4 is obviously in agreement with the results of Figure 45. The data presented in Figure 46 are the results of measurements taken in three different frequency bands. Figure 47 illustrates the variation of loss with frequency in C and X band for a magnesium manganese ferrite having a $4\pi M_s$ of 2064 gauss. The sharp rise of loss with decreasing frequency in C band is due to the proximity of resonance.

These data are replotted in Figure 48 in a form more nearly equivalent to that of Figure 45. The similarity between the shapes of these curves is obvious. The more gradual up turn in the curves of Figure 45 is probably due to the vastly different scale of loss. This magnesium manganese ferrite has an anisotropy field greater than 600 oersteds and therefore the loss curve of Figure 48 lies above any of those of Figure 45.

The variation of differential phase shift (for a typical configuration) as a function of normalized saturation magnetization for a remanence ratio of 0.5 and an anisotropy field of 100 oersteds is shown in Figure 49.

004002

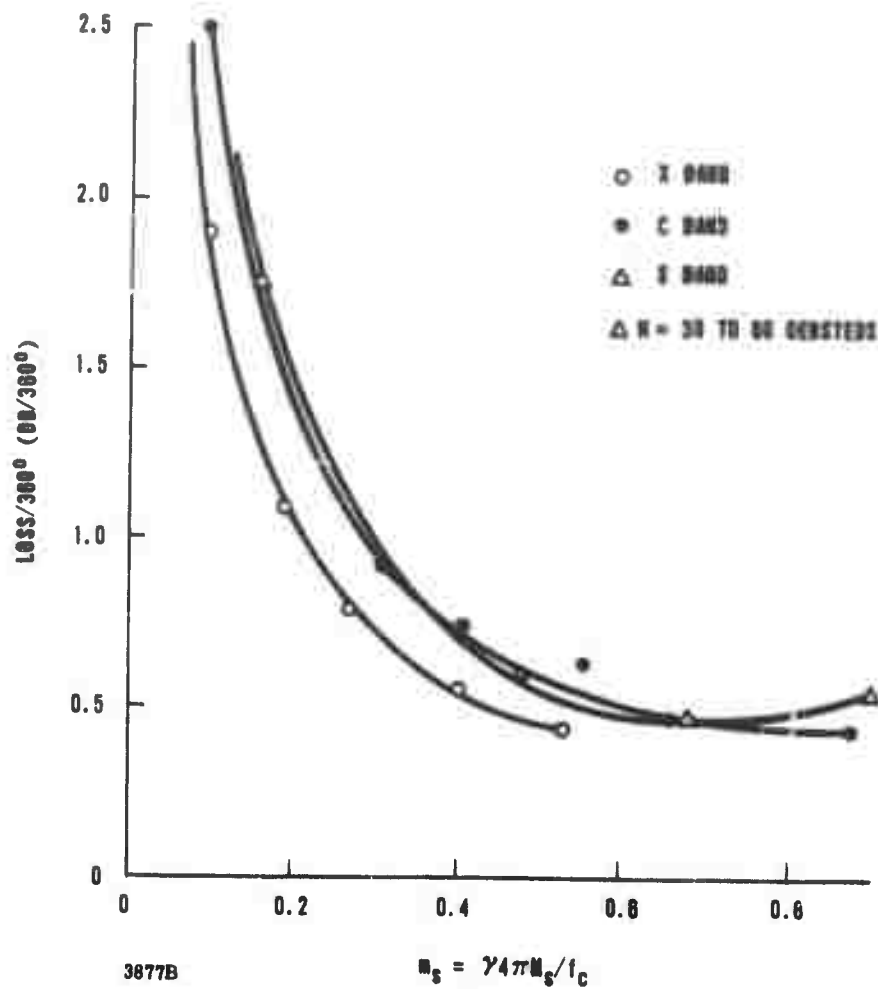


Figure 46. Variation of Loss/360° with Saturation Magnetization in Aluminum-Doped YIG. Experimental Data obtained in Configuration shown in Table V

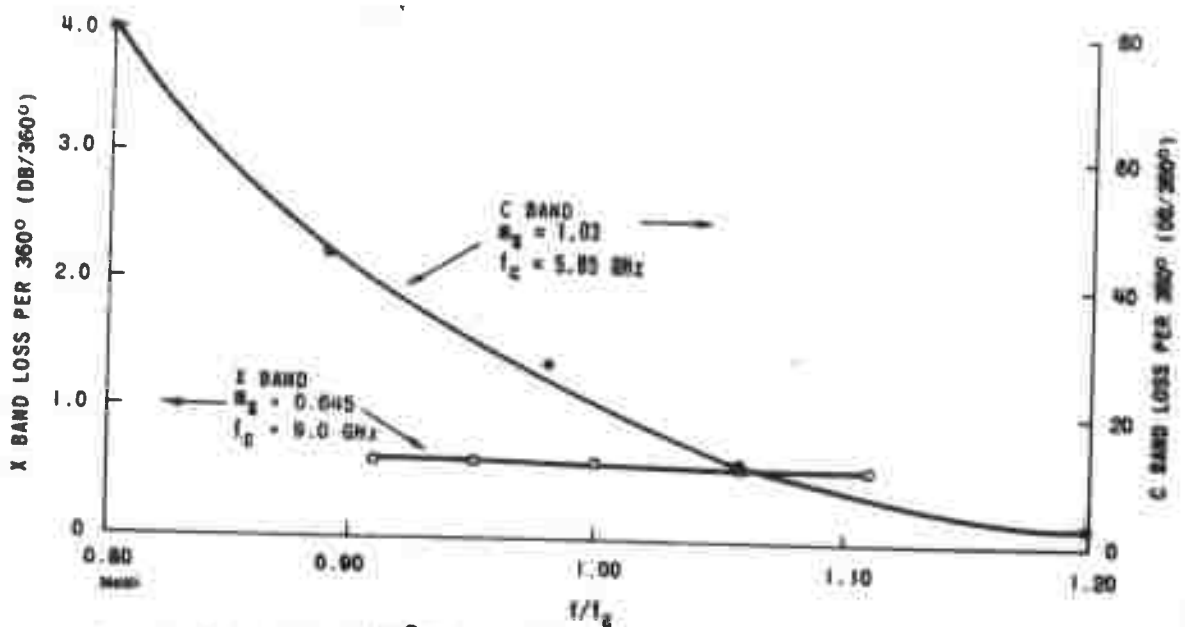
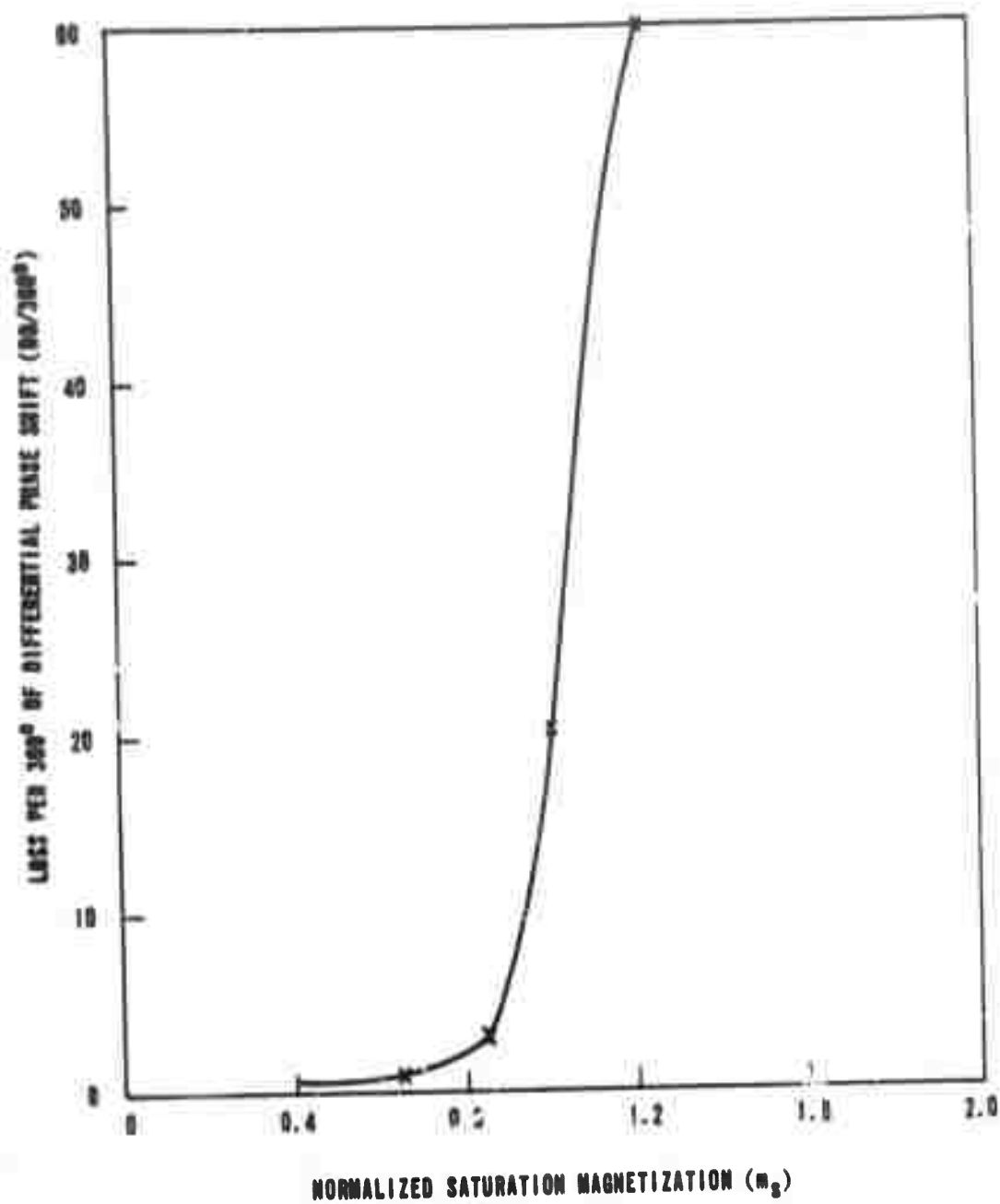
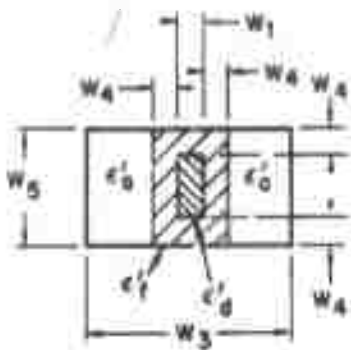


Figure 47. Loss /360° Versus Frequency for Ferrite 83-8 in X Band and C Band Phase Shift Structures. Structure Shown in Table VI



3872B
 Figure 48. Loss Per 360° Versus Magnetization for Ferrite 83-8.
 Configuration Shown in Table VI



$m_s = \text{VARIABLE}$

$f_c = 9 \text{ Gc}$

$\lambda_c = 3.33 \text{ Cm}$

$$m = \frac{\gamma 4\pi M_s}{\omega_c} = R_r m_s$$

HF = FUNCTION OF M_s & H_{anis}

$\Delta H = 0.5 \text{ OERSTEES}$

FR = 1.0

$W_1 = 0.023 \lambda_c$

$W_3 = 0.35 \lambda_c$

$W_4 = 0.04 \lambda_c$

$W_5 = 0.294 \lambda_c$

$H_{anis} = 100 \text{ OERSTEES}$

$R_r = 0.5$

$\epsilon'_d = 18.0$

$\epsilon'_f = 18.0$

$\epsilon'_a = 1.0$

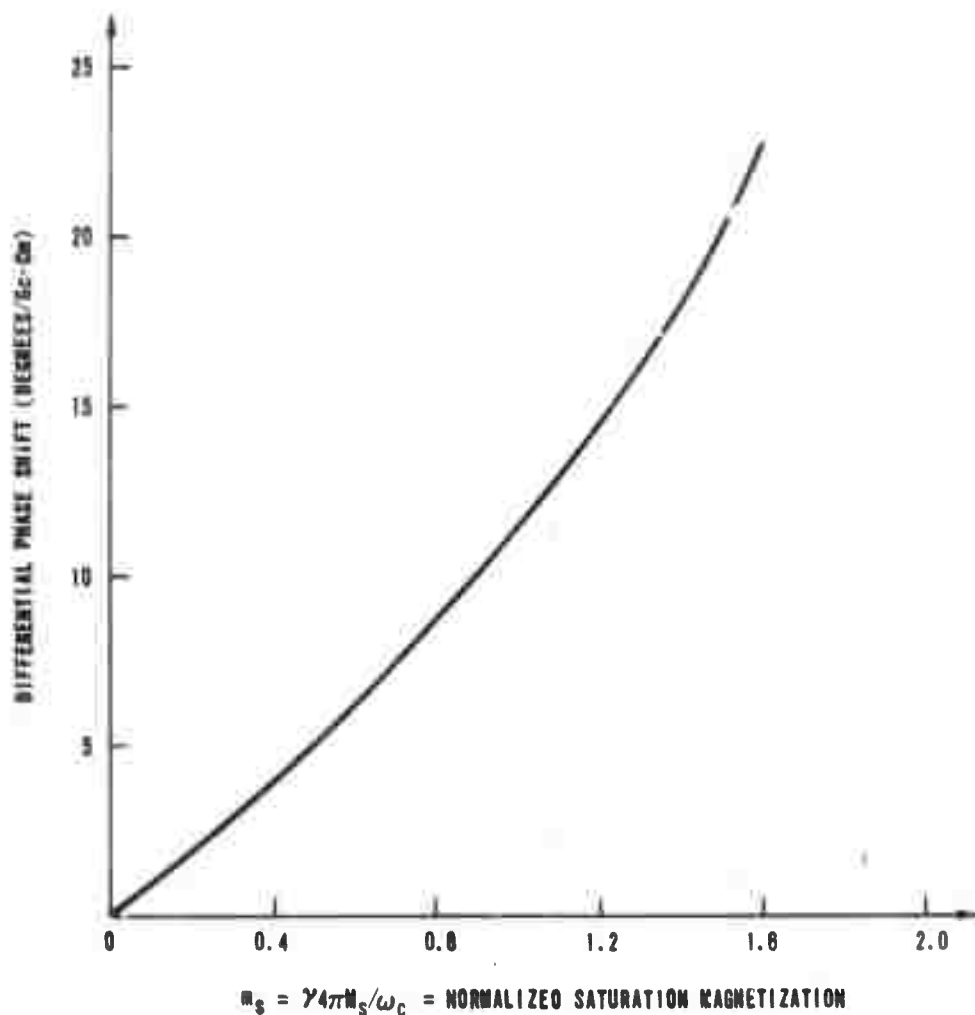
$\tan \delta_d = 0.0005$

$\tan \delta_f = 0.0007$

$\tan \delta_a = 0$

$W_x = 0.9$

$W_y = 0.1$



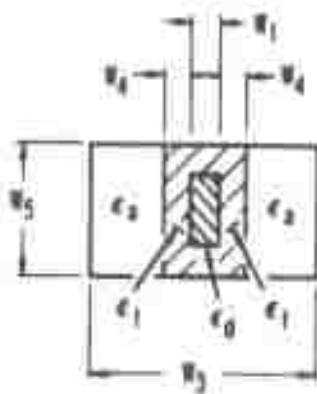
2979B

Figure 49. Variation of Differential Phase Shift as a Function of Normalized Saturation Magnetization

4.5.1.2 Effects of Linewidth On Loss. Figures 50, 51, and 52 highlight the results of a study of magnetic loss as a function of resonance linewidth. The results of this study have shown that magnetic loss in a remanent state ferrite is directly related to the intrinsic linewidth of the materials. In Figure 50 both calculated and experimental results are presented showing the X band loss for each of the two remanent states as a function of intrinsic linewidth ΔH . The loss for both states is seen to increase linearly with linewidth. The differential loss between remanent states also increases with increasing ΔH . For ΔH greater than about 100 oersteds the differential loss in this configuration is large enough to be bothersome in phase shifter applications. The materials used to obtain the experimental data shown in Figure 50 were yttrium dysprosium aluminum iron garnet:

(8% Al, 10% Dy, $\Delta H \approx 380$ oe.), yttrium dysprosium aluminum iron garnet
(8% Al, 4% Dy, $\Delta H \approx 160$ oe.), yttrium dysprosium aluminum iron garnet
(8% Al, 2% Dy, $\Delta H \approx 100$ oe.), yttrium gadolinium iron garnet (30% Gd, $\Delta H \approx 70$ oe.), yttrium aluminum iron garnet (5% Al, $\Delta H \approx 15$ oe.). The data points have been normalized to correspond to a remanence ratio of one-half. For these materials excellent correlation is obtained between experimental losses and those calculated using the intrinsic resonance linewidth. However, the linewidth normally measured for polycrystalline materials is the inhomogeneously broadened linewidth, not the intrinsic linewidth per se. What then is the relationship of the intrinsic linewidth to the polycrystalline linewidth?

The linewidth observed on polycrystalline ferrimagnetic materials arises from several different sources. The various line broadening mechanisms can be categorized as intrinsic damping, porosity broadening, and anisotropy broadening. Obviously, all damping mechanisms are line broadening mechanisms since, in the absence of damping, the resonance line is infinitely narrow.



$$m_s = \frac{\gamma 4 \pi W_s}{\omega_c} = 0.38$$

$$l_c = 9.6c$$

$$m = \frac{\gamma 4 \pi W_l}{\omega_c} = 0.19$$

$$FR = 1.0$$

$$W_1 = 0.08 \lambda_c$$

$$W_2 = 0.382 \lambda_c$$

$$W_4 = 0.04 \lambda_c$$

$$W_5 = 0.294 \lambda_c$$

$$R_l = 0.5$$

$$\epsilon'_d = 1.0$$

$$\epsilon'_d = 18.0$$

$$\epsilon'_l = 18.0$$

$$\tan \delta_d = 0$$

$$\tan \delta_d = 0.0005$$

$$\tan \delta_l = 0.0007$$

$$\lambda_c = 3.33 \text{ cm}$$

$$HF = 0.1$$

$$\Delta H = \text{VARIABLE}$$

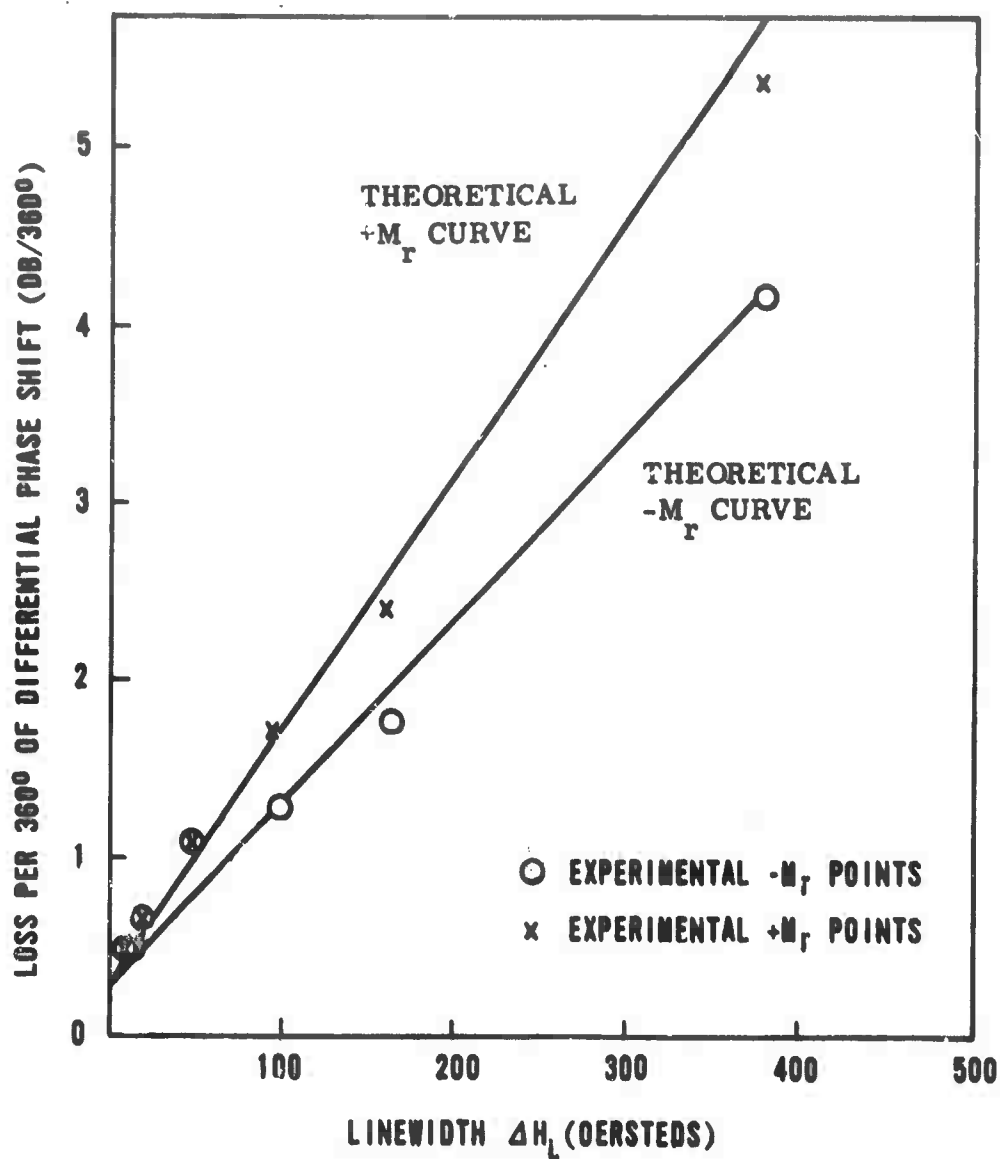


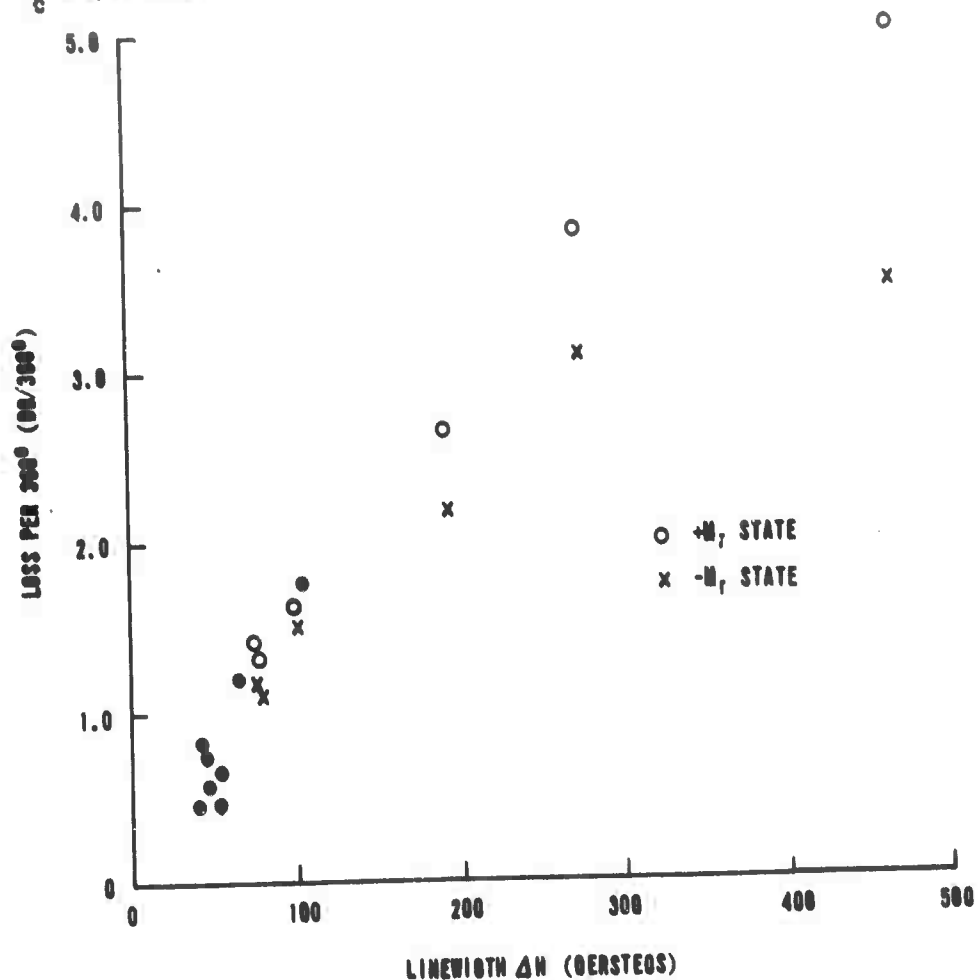
Figure 50. Loss Per 360° Of Differential Phase Shift vs Intrinsic Linewidth

SMEC No.	$4\pi M_B$	ΔH (X Band)	$\tan \delta$	R_r
G-293-5D	640	42	.0005	.58
G-455C	768	461	.0006	.68
G-302-9C	805 *	52 *	.0005	.50
G-454C	815	192	.0006	.68
G-292-2D	830	47	<.0005	.58
G-453D	860	71	.0011	.63
G-452E	925	276	.0005	.42
G-297-6C	980	100	.0008	.63
G-291-2D	1115	55	<.0005	.60
G-288-2C	1150 *	105 *	NM	.51
G-367-2H	1250	75 *	NM	.63
G-404-3D	1325	55	<.0005	.55
G-232-73D	1780 *	40 *	<.0005	.72

* Estimated Value

NM - Not Measured

$f_c = 5.65$ GHz



3873B

Figure 51. C Band Loss/360° Versus Polycrystalline Line-width. Experimental Data obtained in the Configuration shown in Table V

SMEC No.	$4\pi M_s$	ΔH (X Band)	$\tan \delta$	R_r
G-300U	520	80 *	NM	.40
G-461C	570	296	.0005	.58
G-459C	572	470	.0006	.59
G-462C	575	412	.0006	.38
G-460C	600	170	.0004	.50
G-405-3E	610	130	NM	.50
G-458C	625	212	.0005	.67
G-293-5E	640 *	42	<.0005	.43
G-270-3D	690	67	NM	.61
G-292-2E	900 *	47	<.0005	.38
G-291-2E	1200 *	55	<.0005	.51

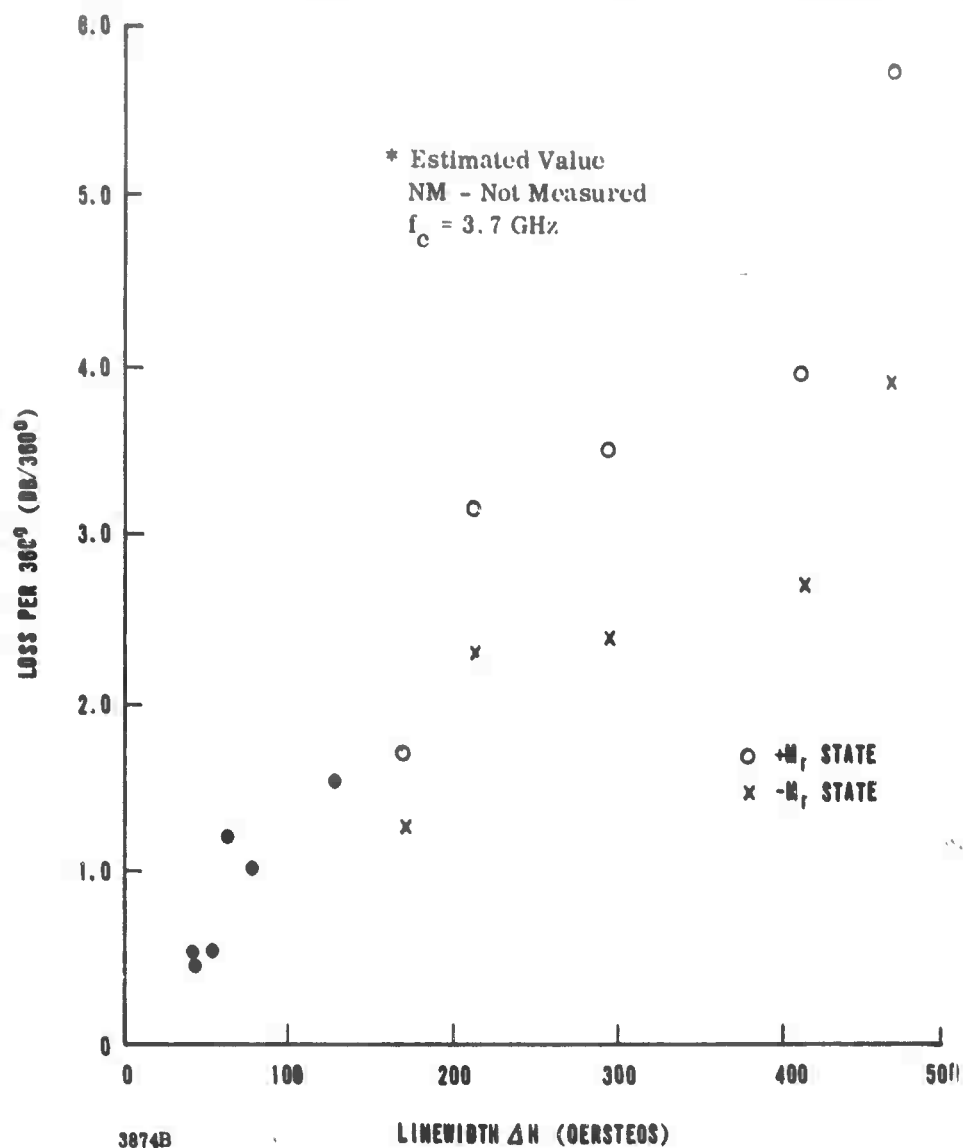


Figure 52. S Band Loss Per 360° Vs Polycrystalline Linewidth.
Experimental data obtained in the configuration shown in Table V

Intrinsic damping contributes to the linewidth that is observed on pure single crystals, free from surface effects and so forth. This certainly represents a lower limit on polycrystalline linewidth, as all other effects will broaden this intrinsic resonance linewidth. The intrinsic linewidth of a polycrystalline sample is the same as the intrinsic linewidth of a single crystal sample of the same material and of equal purity. The equal purity should be kept in mind since lower purity oxides (99.9) are normally used in polycrystalline materials than are used in single crystal work (99.9999). Intrinsic linewidth is rather intimately related to the spin wave linewidth, ΔH_K . In fact, as a good approximation, one can take ΔH_K to be equal to the intrinsic ΔH at the same frequency. A frequency dependence of intrinsic linewidth has been observed on many single crystal samples and some polycrystals. The observed shape of the loss curve and the frequency dependence of linewidth for losses due to intrinsic damping are in excellent agreement with the predictions of the Landau-Lifshitz loss formulation.

Intrinsic linewidths vary widely. Prime examples are found in the garnet family. For example, pure yttrium iron garnet single crystals may have linewidths of a few tenths of an oersted, while the yttrium dysprosium iron garnets may have linewidths of several thousands of oersteds. In fact in the rare earth garnets, intrinsic linewidths are so broad that the single and polycrystalline samples exhibit essentially the same linewidth --- all other contributing factors being almost negligible. This dominance of the intrinsic damping also manifests itself in the observed frequency dependence of the polycrystalline linewidth of rare earth and even of rare earth doped garnets. Thus, the linewidth of a heavily dysprosium doped yttrium iron garnet may show a marked frequency dependence. When intrinsic damping is dominant, X band linewidths may actually be several times larger than L or S band linewidths.

Corruption or porosity broadening occurs in all polycrystalline samples to some extent. The more porous or less dense a polycrystalline sample is, the broader will be its resonance linewidth. Porosity broadening will contribute

a line broadening proportional to the percent porosity and to the saturation magnetization. Porosity broadening seems to be independent of frequency.

Anisotropy broadening has long been recognized as a source of linewidth in polycrystalline materials. Since each grain or crystallite may have its crystallographic axes aligned different from its neighbor, the effective anisotropy field varies from one grain to the next. Thus, each grain will resonate at slightly different field values, and this spread in effective field values gives rise to a spreading out of the resonance loss. This type of line broadening is independent of frequency and is the dominant mechanism in many common ferrites and garnets.

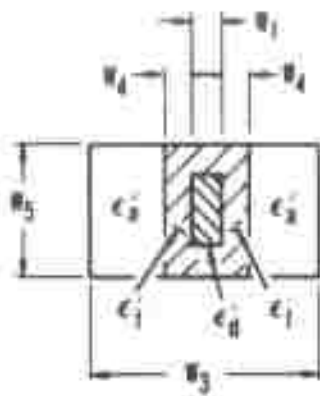
In summary, polycrystalline linewidth of many ferrites and garnets is determined predominately by anisotropy broadening and is rather independent of frequency. In very porous samples, porosity broadening may be the dominant mechanism. It, too, is independent of frequency. In some rare earth doped garnets (or single crystals of other materials), intrinsic damping may be the dominant mechanism, and this linewidth will vary almost linearly with frequency. The appropriate linewidth to use in calculating magnetic losses far from resonance appears to be the intrinsic linewidth. As pointed out above, for some materials, such as the rare earth doped garnets, the polycrystalline linewidth is almost identical to the intrinsic linewidth. In particular, this is true for the dysprosium and gadolinium doped garnets whose test results are compared in Figure 50, i. e., $\Delta H_{\text{polycrystalline}} \approx \Delta H_{\text{intrinsic}}$ for these materials. The two materials, which have no rare earth doping, have polycrystalline linewidths of 30 to 40 oersteds and intrinsic linewidths of 10 to 15 oersteds. Thus, in Figure 50 the apparent correlation between computed and measured values would have been equally as good if the losses had been plotted as a function of polycrystalline rather than intrinsic linewidth. On the other hand, materials such as magnesium manganese ferrite have polycrystalline linewidths of the order of 500 oersteds and intrinsic linewidth of the order of 10 oersteds. With such large differences between the two types of linewidth it is easy to distinguish which linewidth is proper to use in calculating losses. For example, a magnesium manganese ferrite (83-8F) with a polycrystalline linewidth of 512 oersteds and an estimated intrinsic linewidth of 10 oersteds has been tested in X band (see Table VI and Figure 48). The measured loss per 360° of differential phase shift was about 0.6 db/ 360° . The calculated loss based on the polycrystalline linewidth of 512 oersteds is about 8 db/ 360° , while the calculated loss based on an intrinsic linewidth of 10 oersteds is about 0.45 db/ 360° . Dielectric and waveguide copper

losses are included in the calculated values but not losses due to reflections, charging wire, glue, etc. Obviously, the computation based on intrinsic linewidth again is in very good agreement with measured results, while the computation based on polycrystalline linewidth leads to losses much higher than those measured. Thus, the conclusion is that magnetic loss in remanent state ferrimagnetic materials is directly related to intrinsic linewidth and can be accurately predicted from that and other material parameters utilizing the models and analysis techniques presented in Section 3.

The data presented in Figures 51 and 52 show the dependence of loss on linewidth for several materials as measured in C and S bands, respectively. These results can be compared with the data shown in Figure 50. Again, in every case, an approximate linear dependence of loss on linewidth is observed. These materials are all garnets and in the broad linewidth cases have considerable dysprosium doping. In the intermediate linewidth range they contain both small dysprosium and gadolinium dopings. It is interesting to note that these curves are very nearly equal for the three frequency bands. The linewidth axis in Figures 51 and 52 is the X band measured polycrystalline linewidth. For many of these materials the intrinsic and polycrystalline linewidths are essentially identical. However, these data will later be replotted as a function of the proper intrinsic linewidth for each frequency band. The experimental data shown in Figures 50, 51, and 52 of loss versus linewidth were taken for normalized saturation magnetization values between 0.4 and 0.8 when the dependence on magnetization is relatively insignificant (see Figure 45).

4.5.1.3 Effects of Dimensional Changes and Dielectric Loading. For a given set of intrinsic ferrite parameters, the other parameters of a phase shifter structure can be selected to optimize performance in terms of maximum phase shift per unit loss, maximum phase shift per unit length, minimum change in phase shift with frequency, etc. The following figures illustrate how the configurational parameters affect performance characteristics. Both calculated and measured data are given where available. Excellent correlation of experimental and analytical results is obtained.

Figure 53 presents the variation of differential phase shift with dielectric core thickness for several values of core dielectric constant. It can be seen that by proper choice of core width and dielectric constant it is possible to maximize the differential



$$m_s = \frac{\gamma 4 \pi w_s}{\omega_c} = 0.386$$

$$f_c = 9 \text{ Gc}$$

$$m = \frac{\gamma 4 \pi w_l}{\omega_c} = 0.193$$

$$FR = 1.0$$

$$w_1 = \text{VARIABLE}$$

$$w_3 = 0.382 \lambda_c$$

$$w_4 = 0.04 \lambda_c$$

$$w_5 = 0.294 \lambda_c$$

$$R_f = 0.5$$

$$\epsilon_d = 1.0$$

$$\epsilon_d' = \text{PARAMETER}$$

$$\epsilon_f = 18.0$$

$$\tan \delta_d = 0.0007$$

$$\tan \delta_f = 0$$

$$\tan \delta_f = 0.0005$$

$$\lambda_c = 3.33 \text{ cm}$$

$$HF = 0.1$$

$$\Delta H = 65 \text{ Oe.}$$

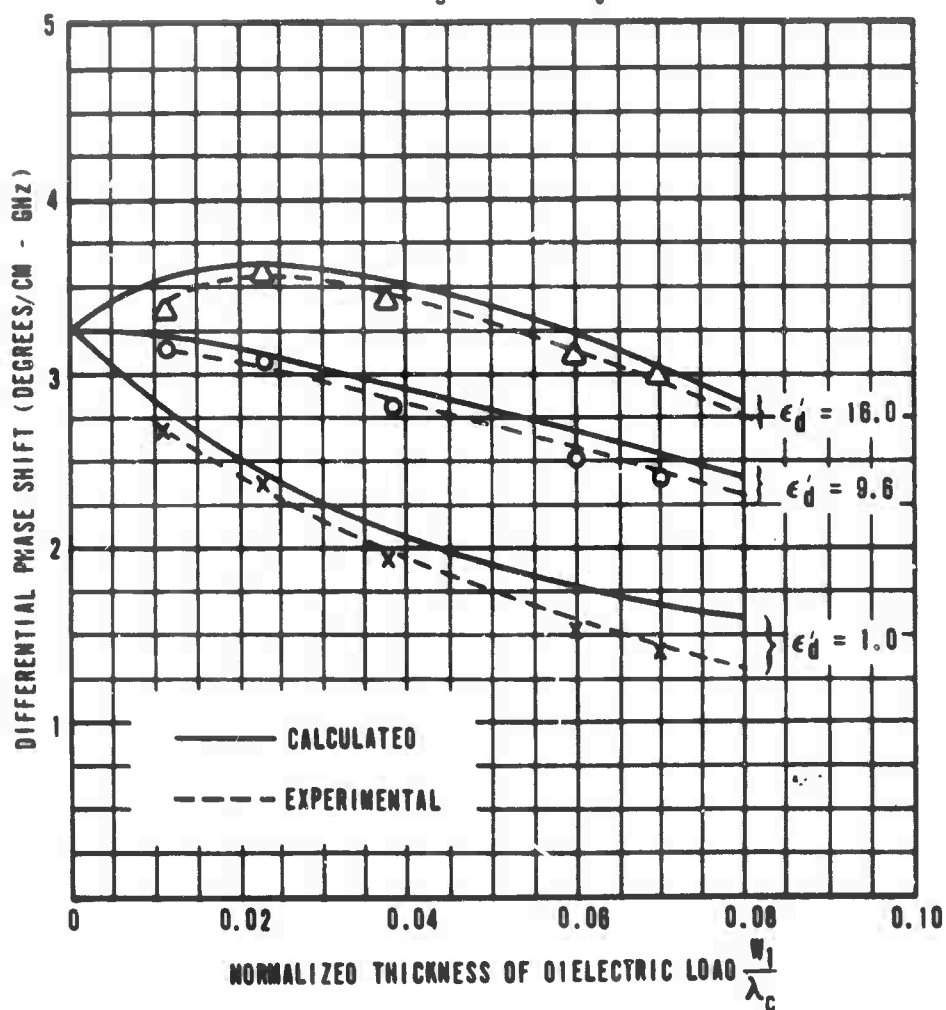


Figure 53. Differential Phase Shift vs Normalized Thickness Of Dielectric Load With Load Dielectric Constant As A Parameter

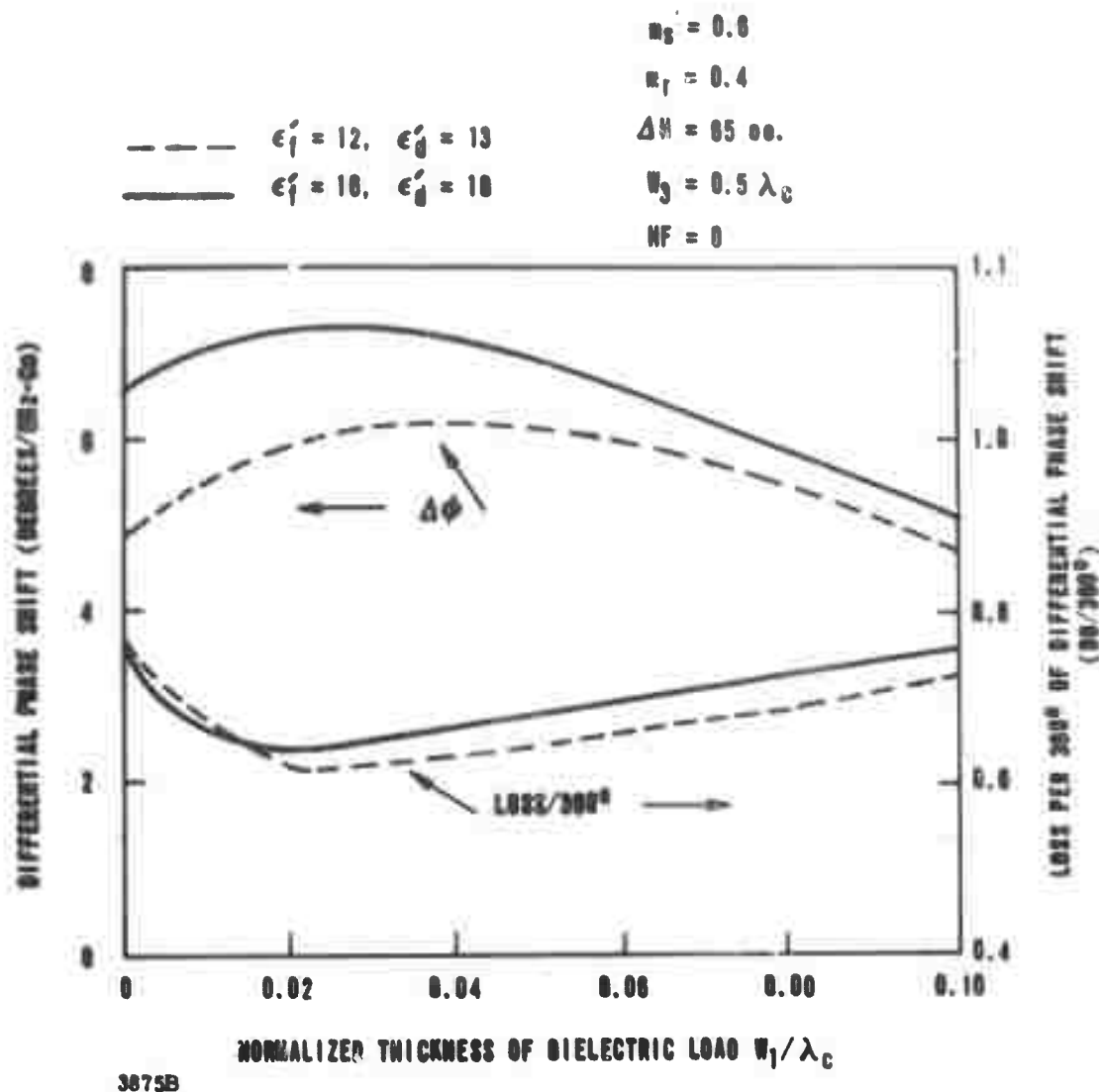


Figure 54. Comparison of Performance of a Typical Ferrite and a Typical Garnet in a FDPS

phase shift per unit length. For the example shown, this maximum occurs with a dielectric constant of 16 and a normalized core width of 0.025.

Figure 54 compares a typical ferrite material to a typical garnet material. The dielectric constant of the load is 13 for the ferrite case and 16 for the garnet case. Differential phase shift and loss per 360° are plotted as a function of slot width W_1 with waveguide width $W_3 = 0.5 \lambda_c$. It is seen that, although the garnet material produces more differential phase shift, its loss per 360° is also slightly more than in the case of the ferrite. It is also seen that differential phase shift in the garnet material peaks

out of a value of $W_1 = 0.025 \lambda_c$, while $W_1 = 0.04 \lambda_c$ gives maximum phase shift in the case of the ferrite. However, minimum loss per 360° is achieved with a value of $W_1 = 0.020 \lambda_c$ in both the garnet and the ferrite, which yields 0.64 db for the garnet and 0.62 db for the ferrite.

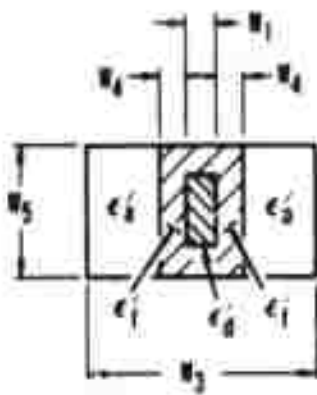
The variation of differential phase shift with frequency can be controlled to some extent by proper selection of waveguide width and dielectric load thickness. Figures 55 and 56 show the frequency variation of differential phase shift for several values of waveguide width and of dielectric load thickness, respectively. It can be seen that in either case there are values of W_3 and W_1 that yield a differential phase shift which is essentially independent of frequency over a wide band of frequencies. For example, from Figure 55 a waveguide width of $0.3 \lambda_c$ and core thickness of $0.023 \lambda_c$ leads to a flat phase shift with frequency when the other parameters of the structure are as shown.

The slope of the phase shift curve is quite important in many applications. Phase slope is defined as the change in differential phase shift over a 0.1 increment in normalized frequency centered at the operating frequency. Figures 57 and 58 show phase slope as a function of waveguide width with core thickness as a parameter. Comparing the two figures, it can be seen that other factors remaining constant, increasing the dielectric constant of the core means that smaller waveguide widths must be used to obtain zero phase slope. For example, if the core dielectric constant is 1.0, then a waveguide width of $0.41 \lambda_c$ and a core thickness of $0.038 \lambda_c$ will yield flat phase with frequency. If the core dielectric constant is increased to 16.0 and the core thickness is maintained at $0.038 \lambda_c$, then the waveguide width must be reduced to $0.32 \lambda_c$ to obtain zero phase slope.

From the data contained in the above figures it is possible to derive a configuration which will have a maximum phase shift per unit loss with the added constraint that the phase slope be zero. For a typical garnet material having a dielectric constant of 16, this optimum configuration would be:

$$\begin{aligned} \text{Waveguide width } W_3 &= 0.365 \lambda_c \\ \text{Dielectric core thickness } W_1 &= 0.025 \lambda_c \\ \text{Toroid wall thickness } W_4 &= 0.045 \lambda_c \\ \text{Core dielectric constant } \epsilon_d &= 16 \end{aligned}$$

This basic configuration is the one now used in the experimental evaluation of materials.



$$m_s = \frac{\gamma 4 \pi M_s}{\omega_c} = 0.38$$

$$f_c = 9 \text{ Gc}$$

$$m = \frac{\gamma 4 \pi M_f}{\omega_c} = 0.19$$

FR = VARIABLE

$$w_1 = 0.023 \lambda_c$$

$$w_3 = \text{PARAMETER}$$

$$w_4 = 0.04 \lambda_c$$

$$w_5 = 0.294 \lambda_c$$

$$R_f = 0.5$$

$$\epsilon'_a = 1.0$$

$$\epsilon'_d = 16.0$$

$$\epsilon'_f = 16.0$$

$$\tan \delta_a = 0$$

$$\tan \delta_d = 0.0005$$

$$\tan \delta_f = 0.0007$$

$$\lambda_c = 3.33 \text{ cm}$$

$$HF = 0.137 = \gamma |\vec{H}_i| / \omega_c$$

$$\Delta H = 65 \text{ Oe.}$$

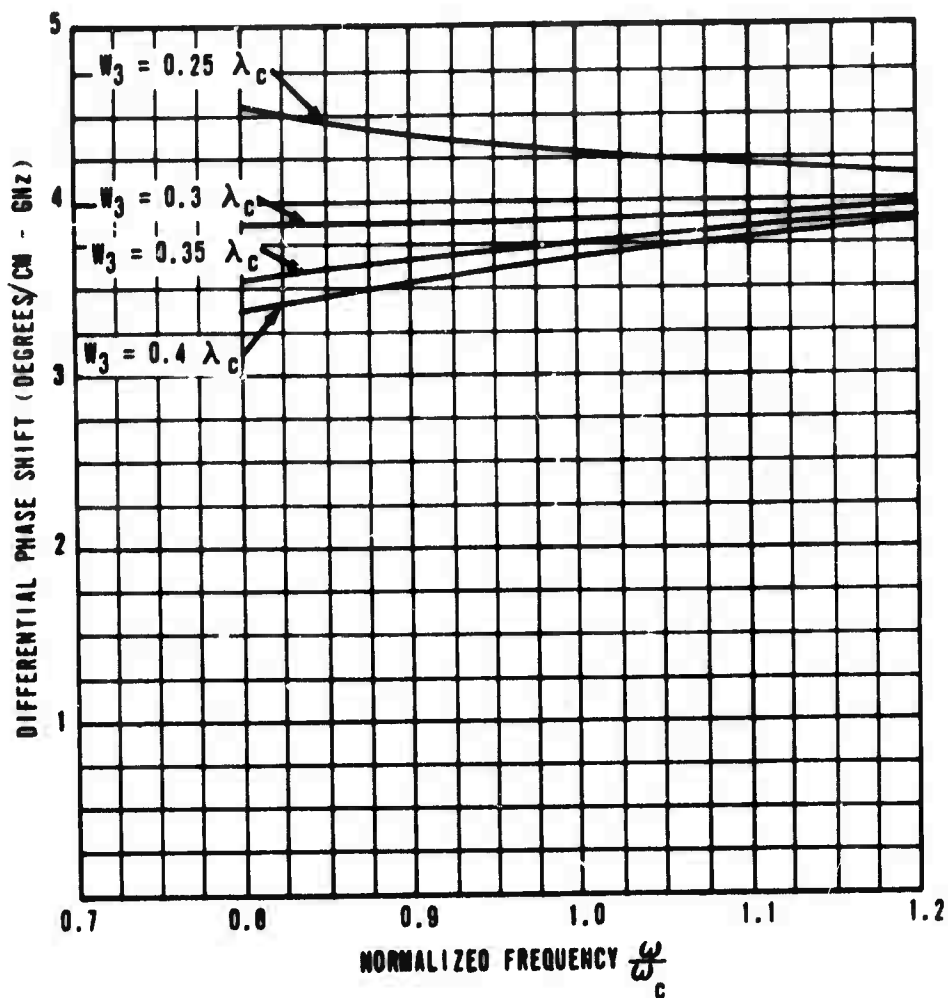
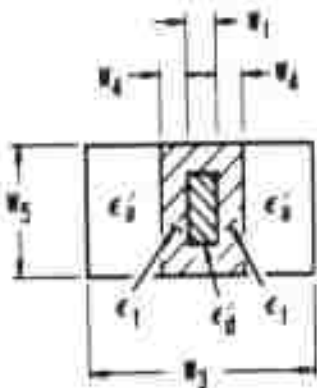


Figure 55. Differential Phase Shift vs Normalized Frequency
With Waveguide Width As A Parameter



$$m_s = \frac{\gamma 4 \pi W_s}{\omega_c} = 0.388$$

$$f_c = 9 \text{ Gc}$$

$$m = \frac{\gamma 4 \pi W_r}{\omega_c} = 0.193$$

FR = VARIABLE

W1 = PARAMETER

$$W_3 = 0.382 \lambda_c$$

$$W_4 = 0.04 \lambda_c$$

$$W_5 = 0.294 \lambda_c$$

$$R_r = 0.5$$

$$\epsilon'_a = 1.0$$

$$\epsilon'_d = 1.0$$

$$\epsilon'_f = 16.0$$

$$\tan \delta_a = 0$$

$$\tan \delta_d = 0.0005$$

$$\tan \delta_f = 0.0007$$

$$\lambda_c = 3.33 \text{ cm}$$

$$HF = 0.1$$

$$\Delta H = 65 \text{ Oe.}$$

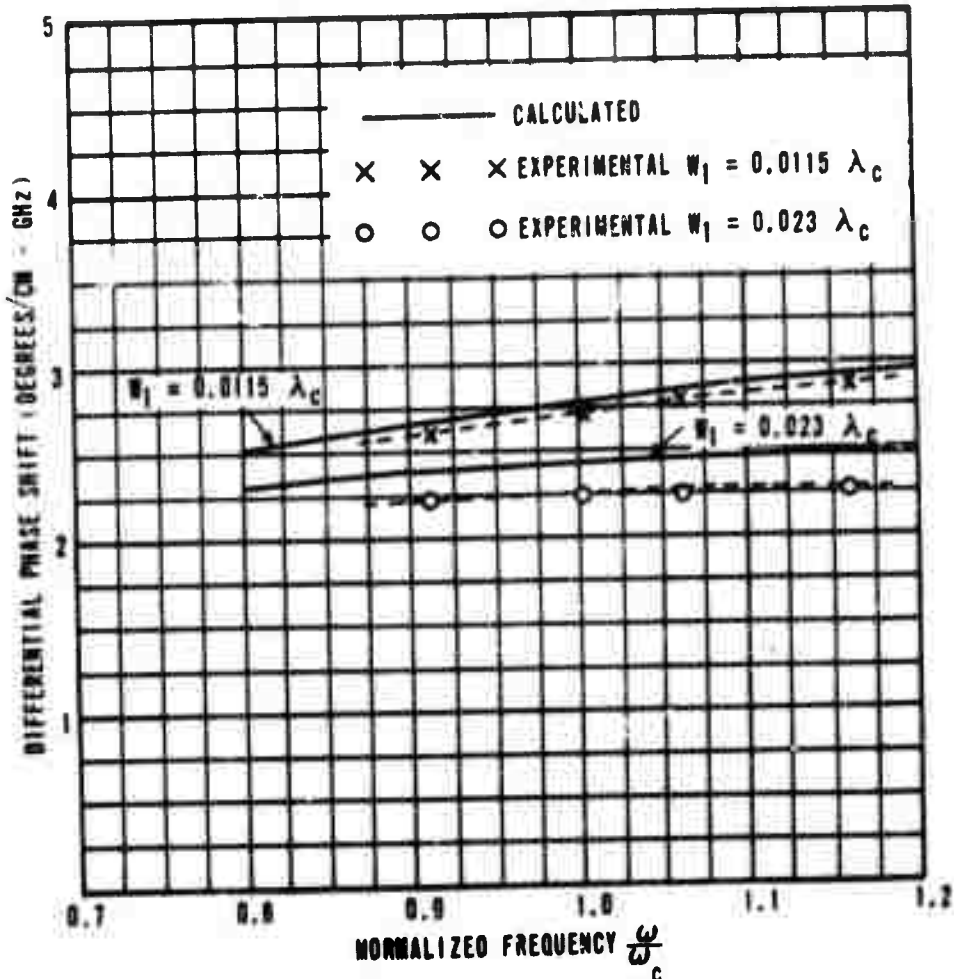
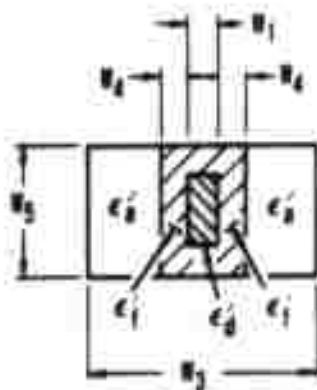


Figure 56. Differential Phase Shift vs Normalized Frequency With Dielectric Load Thickness As A Parameter



$$n_s = \frac{\gamma 4\pi W_s}{\omega_c} = 0.386$$

$$l_c = 0.0c$$

$$n = \frac{\gamma 4\pi W_l}{\omega_c} = 0.193$$

W_1 = PARAMETER
 W_3 = VARIABLE
 $W_4 = 0.04 \lambda_c$
 $W_5 = 0.294 \lambda_c$

$$\gamma_f = 0.5$$

$$\epsilon'_a = 1.0$$

$$\epsilon'_d = 1.0$$

$$\epsilon'_f = 16.0$$

$$\tan \delta_a = 0$$

$$\tan \delta_d = 0.0005$$

$$\tan \delta_f = 0.0007$$

$$\lambda_c = 3.33 \text{ cm}$$

$$HF = 0$$

$$\Delta H = 65 \text{ Oe.}$$

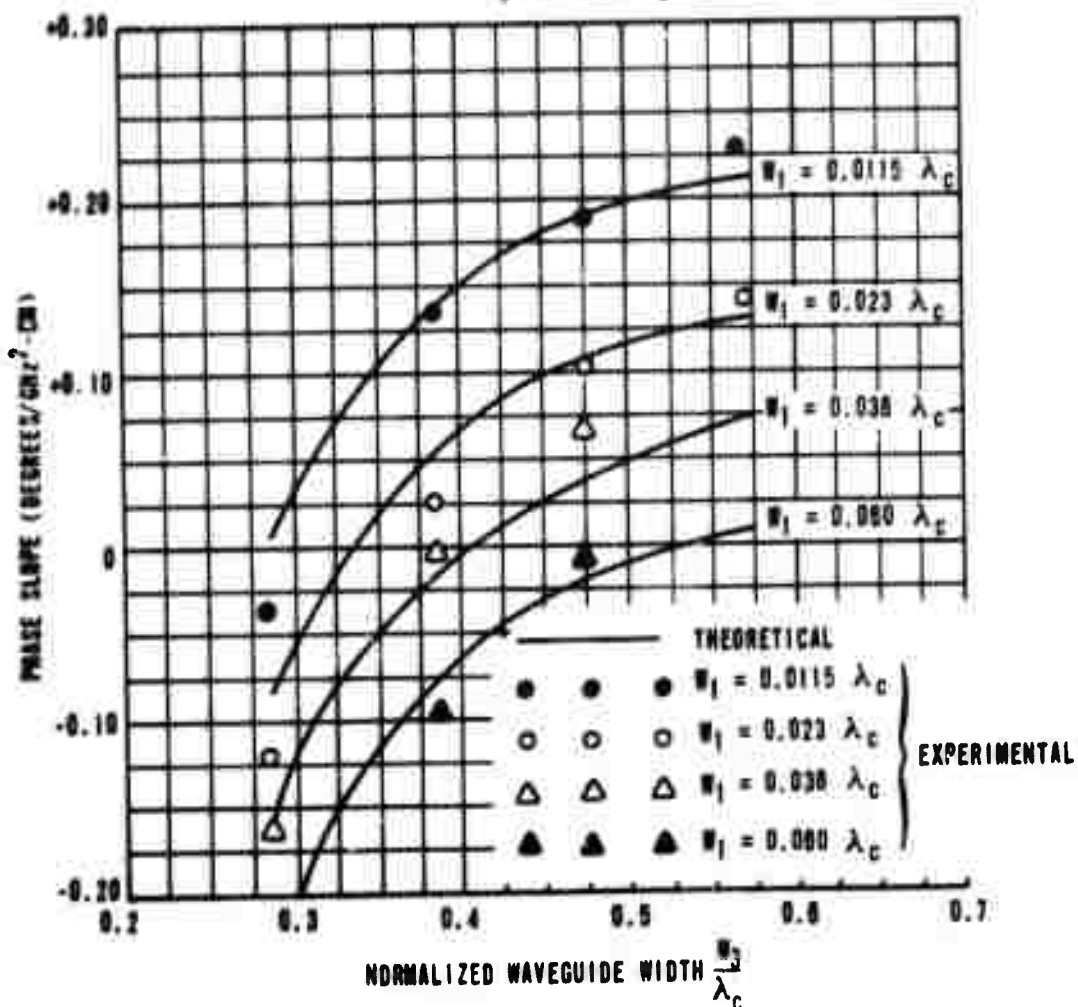
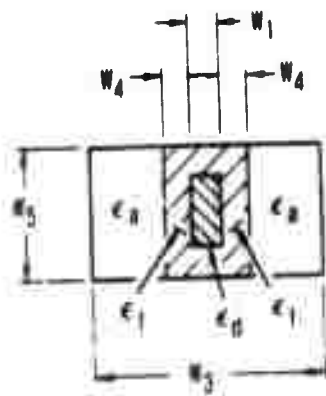


Figure 57. Phase Slope vs Normalized Waveguide Width With Dielectric Load Thickness As A Parameter



$$m_s = \frac{\gamma 4 \pi M_s}{\omega_c} = 0.386$$

$$f_c = 9 \text{ Gc}$$

$$m = \frac{\gamma 4 \pi M_r}{\omega_c} = 0.193$$

$$W_1 = \text{PARAMETER}$$

$$W_3 = \text{VARIABLE}$$

$$W_4 = 0.04 \lambda_c$$

$$W_5 = 0.294 \lambda_c$$

$$R_l = 0.5$$

$$\epsilon_a = 1.0$$

$$\epsilon_d = 16.0$$

$$\epsilon_1 = 16.0$$

$$\tan \delta_a = 0$$

$$\tan \delta_d = 0.0035$$

$$\tan \delta_1 = 0.0007$$

$$\lambda_c = 3.33 \text{ cm}$$

$$HF = 0$$

$$\Delta H = 65 \text{ Oe.}$$

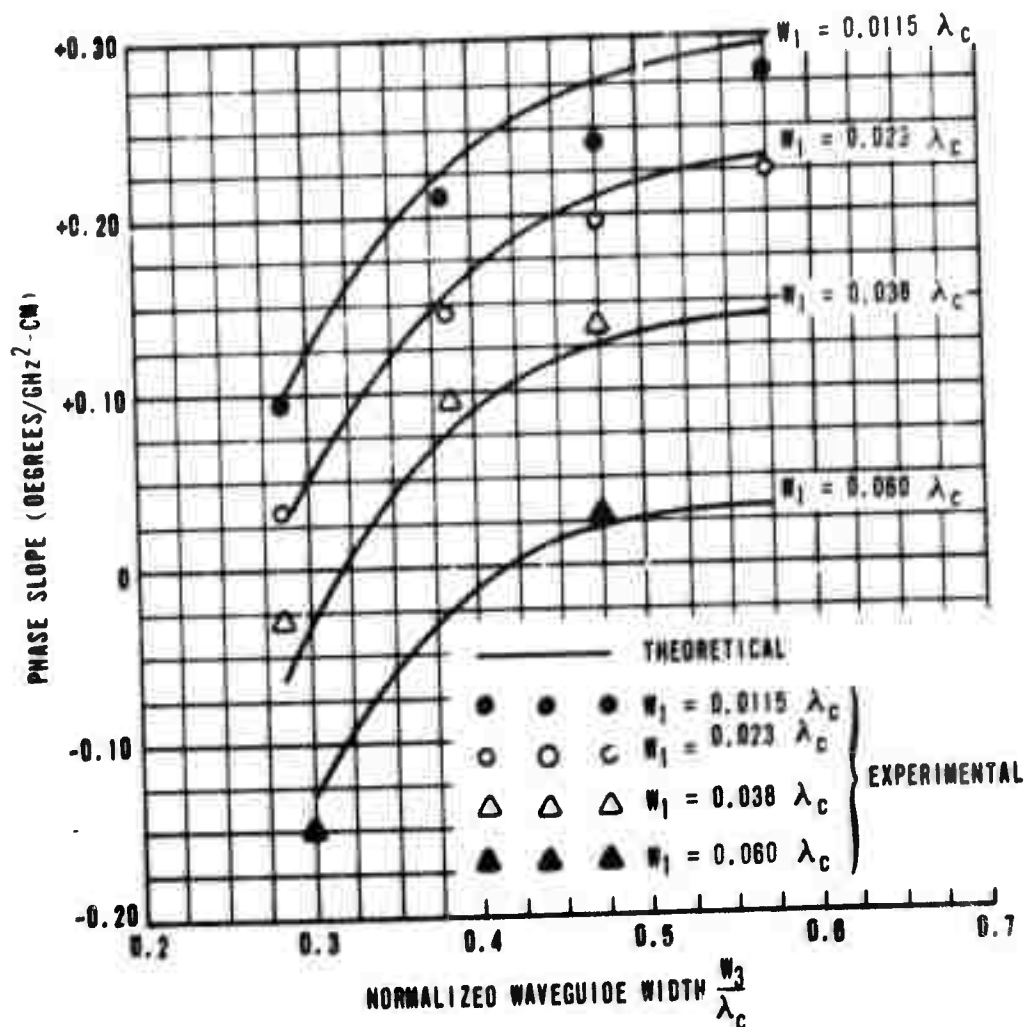


Figure 58. Phase Slope vs Normalized Waveguide Width With Dielectric Load Thickness As A Parameter

4.5.2 Below Resonance Operation of FDPS

A helical line phase shifter on loan from Mr. D. H. Temme of MIT Lincoln Laboratories, is shown in Figure 59. A cutaway has been made to show a portion of the circuit including the helix, ferrite toroid and the toroid charging wire. A more complete description of this device is given elsewhere.¹⁶

Three aluminum substituted YIG materials were tested in this structure in the latched condition:

G-289-6J	YIG
G-290-R	0.03 Al + YIG
G-404-J	0.05 Al YIG

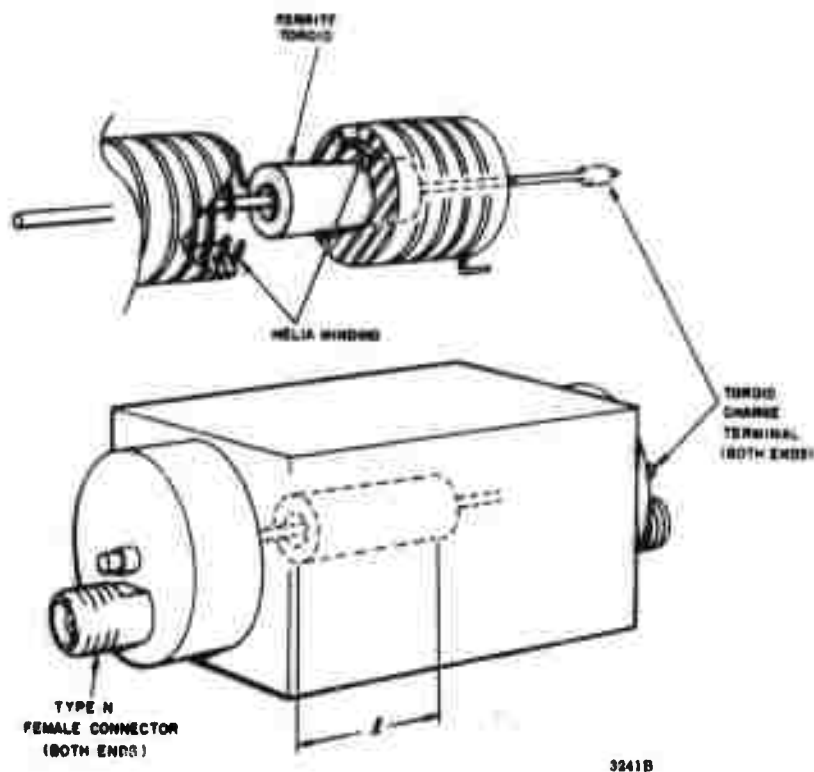


Figure 59. Helical Phase Shifter Structure used for Magnetic Loss Measurements

¹⁶ Final Report "Development of Helical Phase Shifters", prepared for MIT Lincoln Laboratories on Subcontract No. 250, Prime Contract No. AF19(628)-500, December 1964, Pg. 71.

Figure 60 shows the magnetic loss corresponding to the two remanent states $+M_r$ and $-M_r$ in a YIG toroid ($4\pi M_s \approx 1780$ gauss). The toroid length was 0.470 inches. Resonance occurs at about 2400 MHz and 2500 MHz in the two states, respectively. The increases in loss seen at 3800 MHz and the scattering of the data points near resonance cannot be explained at this time but may be due to structural anomalies.

Figure 61 shows the losses corresponding to $+M_r$ and $-M_r$ in a 1-inch long sample of 3 percent aluminum substituted YIG ($4\pi M_s \approx 1600$). The material resonates at 2050 MHz and 2200 MHz respectively in the two states, and the losses decrease smoothly to about 2 db at 3800 MHz.

Figure 62 shows the $+M_r$ and $-M_r$ losses for a 1-inch long toroid made from 5 percent aluminum substituted YIG with a $4\pi M_s \approx 1325$ gauss. The resonance frequencies are 2000 MHz and 1950 MHz respectively.

In both Figures 61 and 62 it is clearly seen that the losses designated $+M_r$ are greater than those designated $-M_r$ at resonance but, at frequencies below resonance, they cross and the $-M_r$ losses are greater than the $+M_r$ losses. The $+M_r$ line is seen to tail out more gradually at the high frequency side of resonance, while the $-M_r$ line tails out more gradually at the low frequency side. This basic difference in the shapes of the resonance lines may be related to the difference in the effective permeability of the two remanent states. The effective permeability corresponding to $+M_r$ and $-M_r$ would be expected to give rise to different degrees of loading in the structure.

Figure 63 shows the below resonance (frequency) nonreciprocal differential phase shift per inch measured on the three materials, YIG, 3 percent aluminum substituted YIG, and 5 percent aluminum substituted YIG (G-289, G-290 and G-404 respectively). The respective phase shifts of these materials are seen to be roughly 40 degrees/inch, 50 degrees/inch and 55 degrees/inch. Whether this differential phase shift is due to differences in the field displacements associated with $+M_r$ and $-M_r$, which is the usual cause, or to possible differences in H_i is not clear at this time. It should also be noted that the measured differential phase shift here decreases with increasing magnetization. This may follow from the fact that differential phase shift in this mode of operation depends on the proximity of the resonance frequency to the operating frequency, and the resonance frequency in turn is a function of $4\pi M_s$.

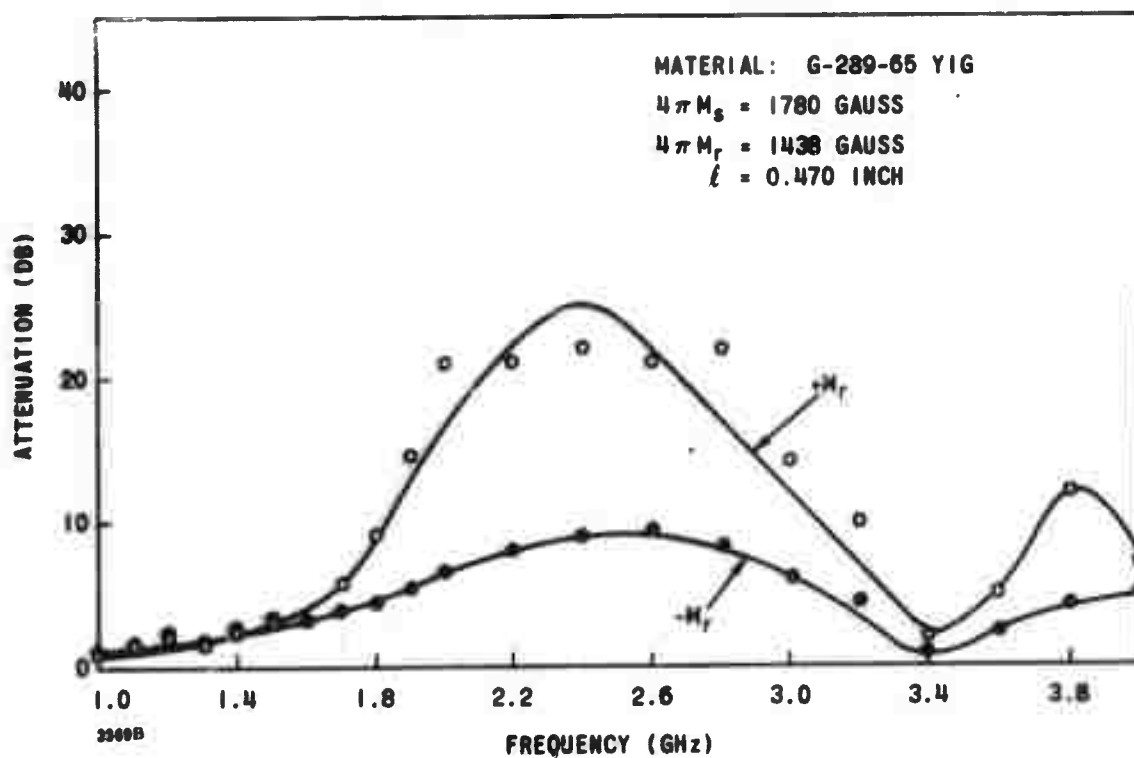


Figure 60. Magnetic Loss Versus Frequency for G-289-6J in the Helix Structure

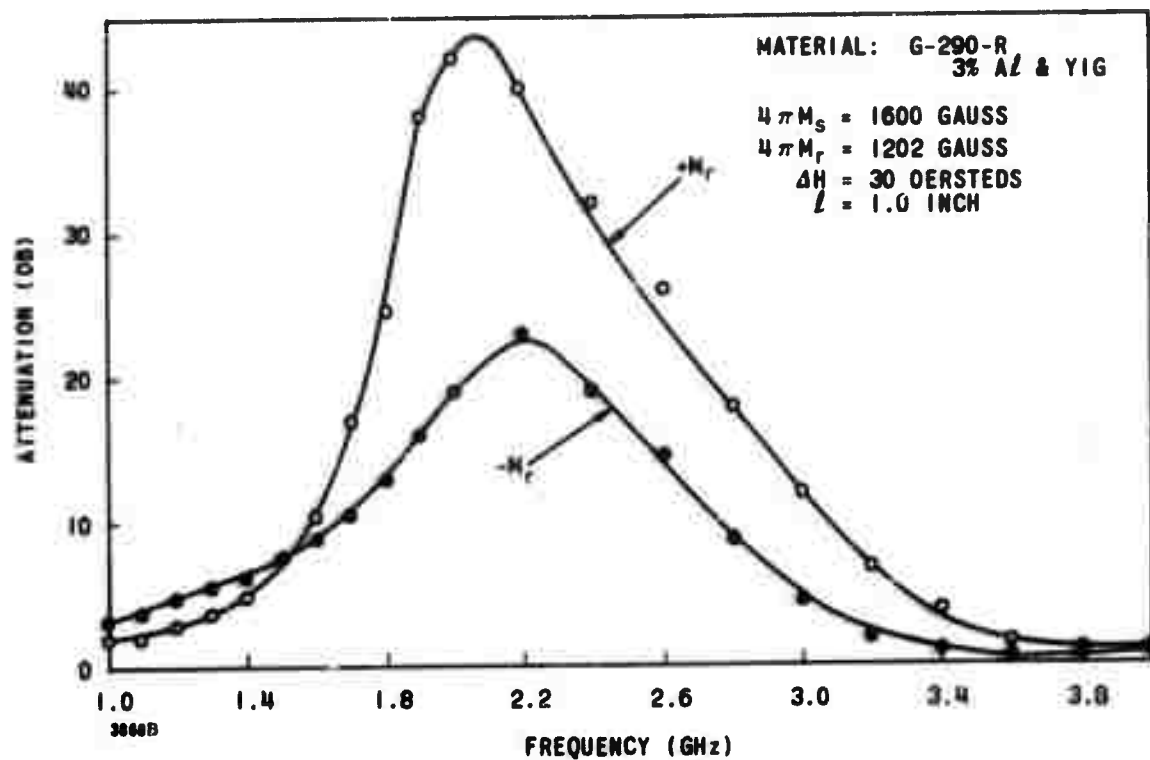


Figure 61. Magnetic Loss Versus Frequency for G-290R in the Helix Structure

004002

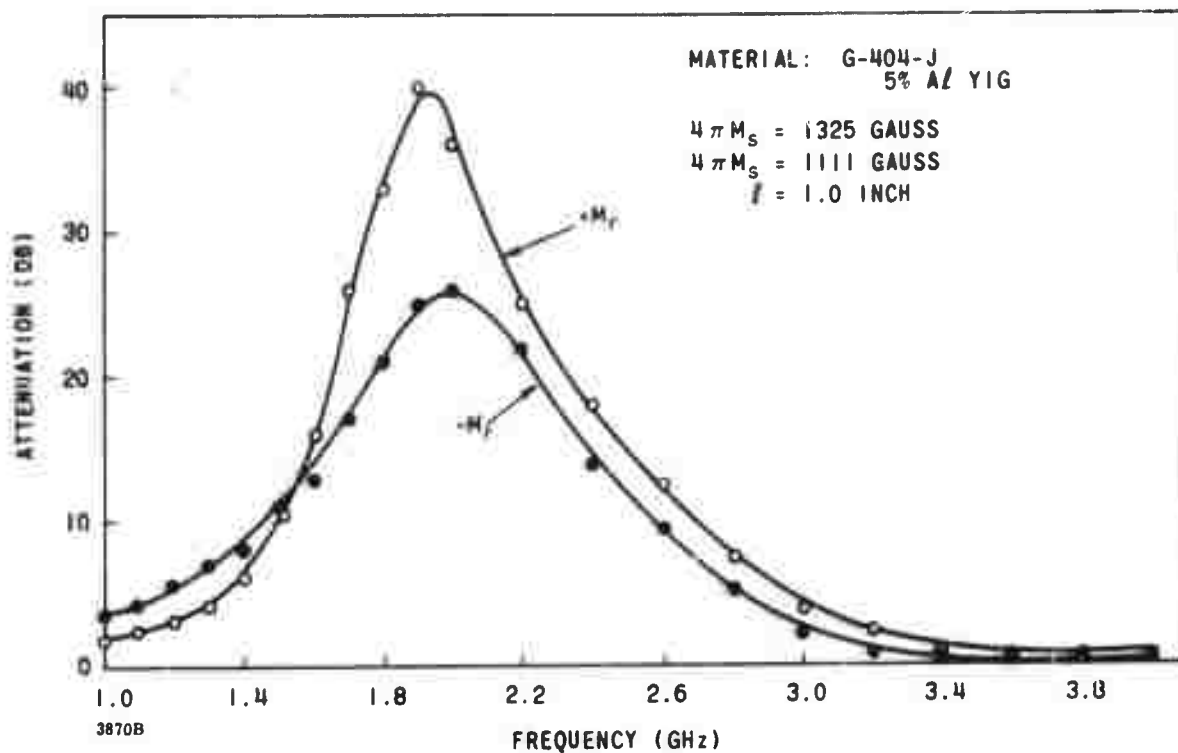


Figure 62. Magnetic Loss Versus Frequency for G404J in the Helix Structure

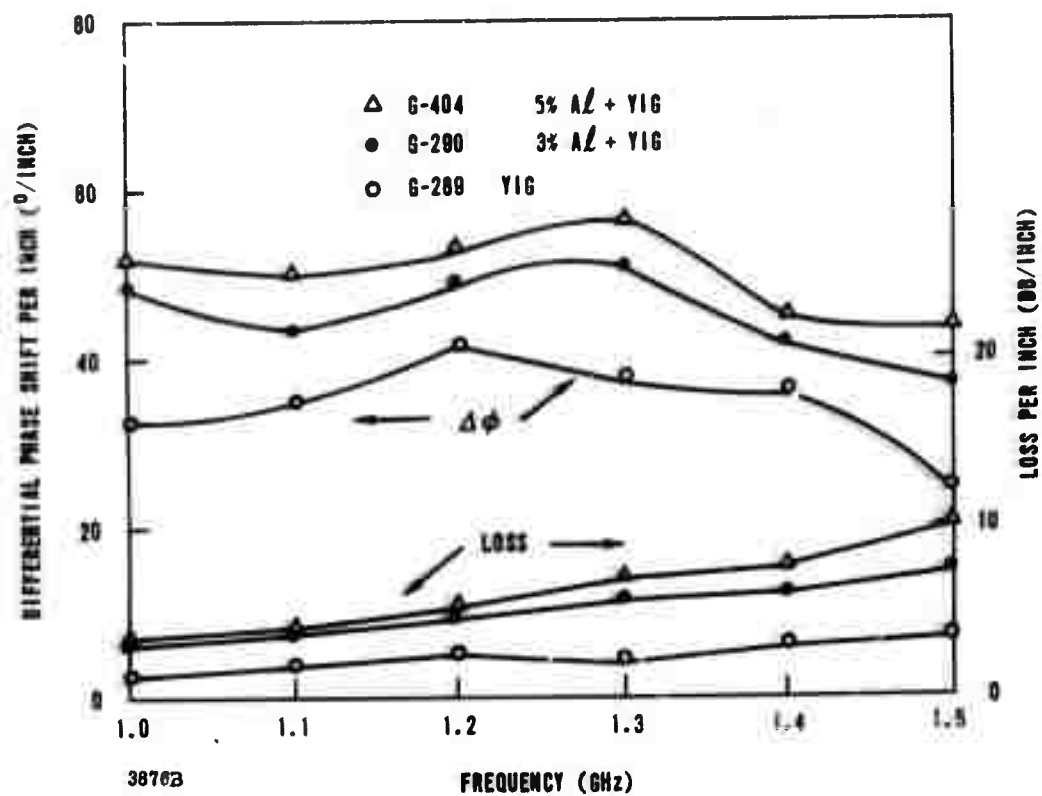


Figure 63. Differential Phase Shift and Loss Versus Frequency in the Helix Structure

The observed slight decrease in phase shift with increasing frequency is probably connected with the fact that maximum nonreciprocal phase shift in a helix structure occurs when the length of the helix turns is an odd multiple of $\lambda/4$. Since the length of the helix turns in this case was chosen to be $3\lambda/4$ at 3000 MHz, then maxima in the nonreciprocal phase shift should occur at 1000 MHz, 3000 MHz, 5000 MHz, etc., while minima should occur at 2000 MHz, 4000 MHz, etc. Thus, phase shift due solely to the helix should decrease with frequency from 1000 MHz to 2000 MHz. This decrease is, of course, offset to some extent by the increase that occurs as the resonance in the material is approached. The cyclic variation in phase shift is felt to be due to dimensional effects.

The losses shown in Figure 63 are those corresponding to $-M_r$, representing, therefore, the maximum loss over the range for which phase shift could be measured. The preliminary data shown here leave much room for improvement before below resonance operation can be extended to a device development state. The results are certainly encouraging, however, and because of the potential improvement this type of operation may yield in high power applications, it will be further pursued. Further investigations of this type of operation will be made in the waveguide structures shown in Section 4.4.

4.5.3 High Power Characteristics of FDPS

The conclusions drawn from the discussion of peak power effects in remanent state ferrites (Section 3.2.2) are that the peak power handling capacity of a material at a given frequency can be increased by increasing the spinwave linewidth ΔH_k (perhaps by rare earth doping) or by decreasing the saturation magnetization (perhaps by aluminum doping). With these conclusions as a guide, materials have been selected for evaluation which should lead to a good understanding of the material properties required for obtaining high peak power thresholds in L, S, C and X bands. Tables V and VI provide a list of high power data on a number of materials tested in X, C, and S bands. The tables also give microwave and square loop properties of the materials listed and low power phase shifter performance data on the material. The configuration used in the testing are also shown in the tables.

Figure 64 presents a graphical summary of the currently available results of high power measurements performed on a variety of materials. The left-hand ordinate gives the threshold values of the rf magnetic field, h_{crit} . These values were calculated from the measured threshold power levels. The four right-hand ordinates specify the corresponding threshold power levels in L, S, C and X bands. These threshold power levels are the calculated values of peak power levels required to generate the given rf critical field value in a typical waveguide nonreciprocal phase shifter.

The data given in Figure 64 is in good agreement with the results expected from predictions based on the domain model for peak power effects presented in Section 3.2.2. The threshold field obviously increases with decreasing saturation magnetization.

The dotted curve illustrates the way in which h_{crit} would vary according to the equation

$$h_{crit} = \frac{\omega \Delta H_k}{\gamma 4 \pi M_s}$$

which assumes that low k spinwaves are always available at half the operating frequency. At low values of saturation magnetization, the dependence on m_s ($= \gamma 4 \pi M_s / f$) is clearly much stronger than this simple inverse relation. As pointed out in Section 3.2.2 for normalized saturation magnetization values less than about 0.3 the relative position of the spinwave manifold is such that (for even the most unfavorable domains) only high k half-frequency spinwaves are available (see Figure 5). Since the spinwave linewidth appears to vary as $\Delta H_k = A + Bk^2$, the restriction of scattering to high k spinwaves causes a rapid increase in ΔH_k (and h_{crit}) as the normalized magnetization m_s decreases in the vicinity of 0.3.

This increase in h_{crit} is observed to be sharper or more abrupt in the case of the aluminum doped YIG than for the rare earth doped garnets. This difference can be easily explained in terms of the A and B coefficients of the terms that make up ΔH_k or ΔH_{int} . For yttrium and aluminum doped garnets, the A term is very small so that the intrinsic linewidth, and hence h_{crit} is very sensitive to changes in the second of Bk^2 term. In the rare earth doped garnets, the A term is considerably larger so that the variation of the Bk^2 term with m_s is felt more gradually.

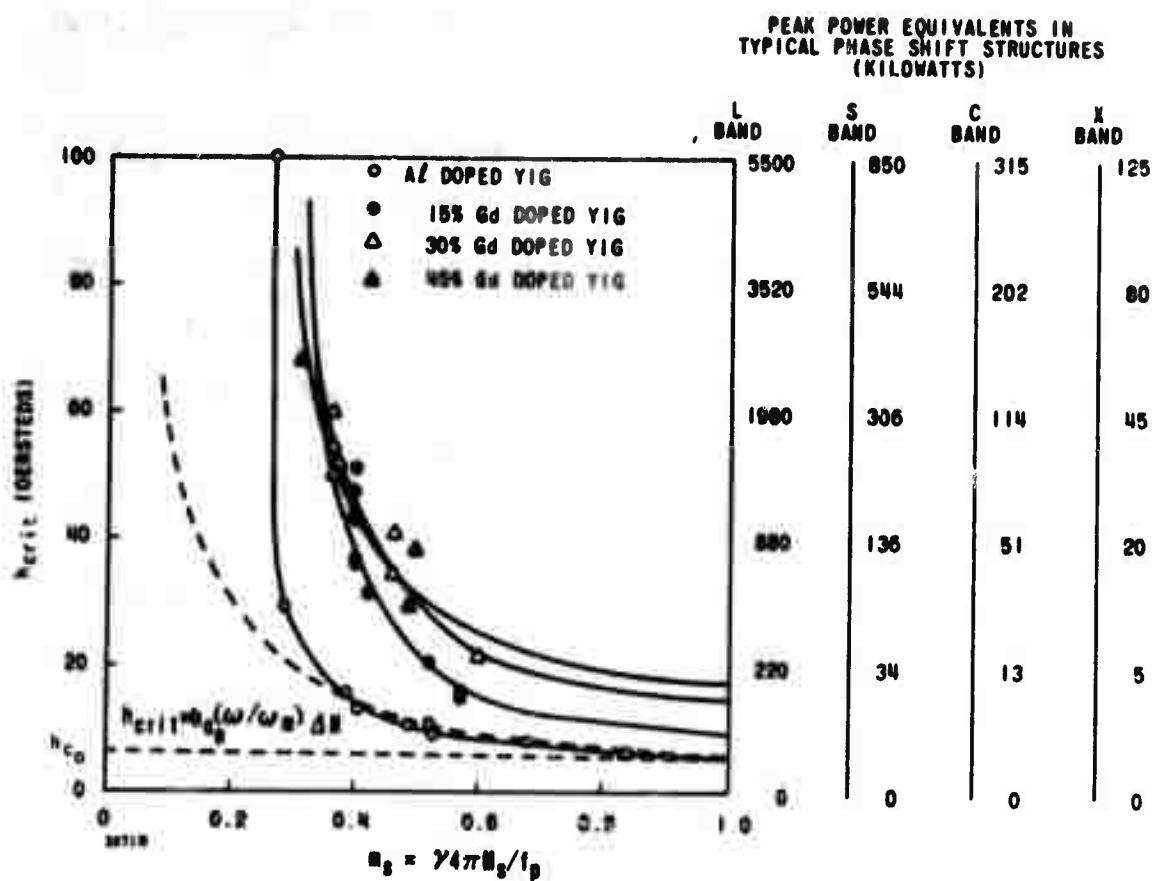


Figure 64. Ferrite Critical Field Dependence on the Frequency Normalized Saturation Magnetization for Aluminum and Gadolinium Substituted YIG. Experimental Data from the Configuration of Table V

For a fixed value of m_s (e. g. $m_s = 0.6$), the measured value of h_{crit} is seen to vary almost directly with ΔH_k or $\Delta H_{intrinsic}$. Thus, the threshold field varies almost directly with gadolinium (or any rare earth) substitution for all m_s values. It should be kept in mind that increasing ΔH_k (and therefore $\Delta H_{intrinsic}$) will also cause an increase in the insertion loss.

The data shown in Figure 65 were taken on a single dielectrically loaded ferrite slab. The configuration simulates a dielectrically loaded ferrite toroid where the ferrite slab represents one leg of the toroid. These data were taken to indicate the type of dependence of critical power level (P_{crit}) observed as a function of effective bias field.

In the initial region (for applied fields less than about 50 oersteds) the material is essentially unsaturated and as a result certain portions of it (Polder-Smit domains) have high effective bias fields which raise the spinwave manifold so that intermediate and low k spinwaves are degenerate with one-half the operating frequency. As the material is saturated and these Polder-Smit domains are wiped out, P_{crit} increases due to the fact that now the spinwave manifold for all regions of the ferrite has been lowered so that no intermediate or low k spinwaves are degenerate with one-half the operating frequency. This is the same operation region where the low $4\pi M_s$ digital phase shifters operate. As the applied field continues to increase the low k portion of the spinwave manifold is raised until it becomes degenerate with the operating frequency and at that point P_{crit} decreases. As the applied field is still further increased, eventually the point will be reached where the half-frequency point is below the entire spinwave manifold and then a very strong increase in P_{crit} would be observed with applied field. These measurements do not extend to sufficiently high applied fields to reach this final state.

Figure 66 shows the loss and phase shift versus applied field for the same dielectric loaded single slab configuration. It is seen that the differential phase shift, which is the difference in the two phase shift nulls shown, is approximately 150° at about 50 oersteds of applied dc magnetic field. This would be approximately the condition seen by a ferrite toroid in the remanent state. The phase shift is then seen to increase rapidly to a value of approximately 300° at an applied field of approximately 200 oersteds. For further increases in applied field, no appreciable increase in phase

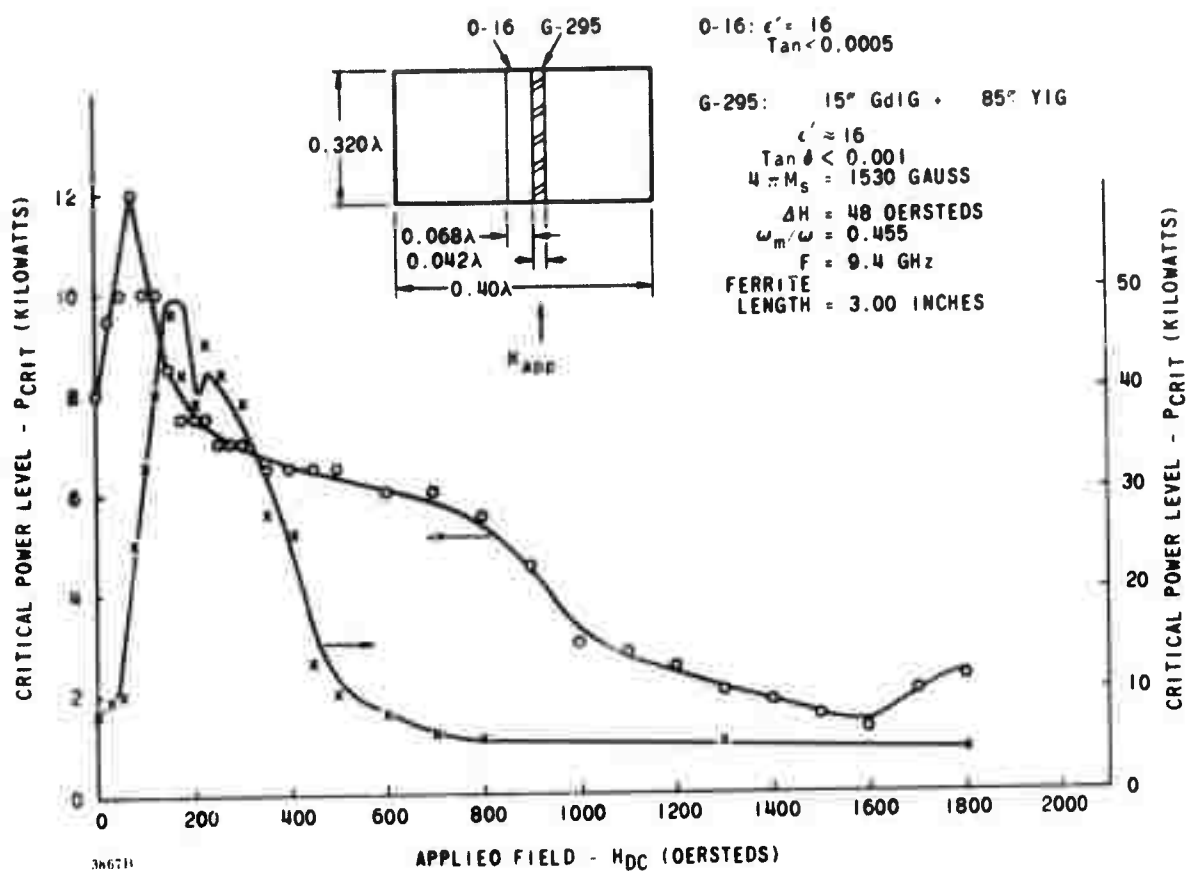


Figure 65. Critical Power Level Variation with Applied DC Magnetic Field in a Dielectrically Loaded Ferrite Slab Configuration.

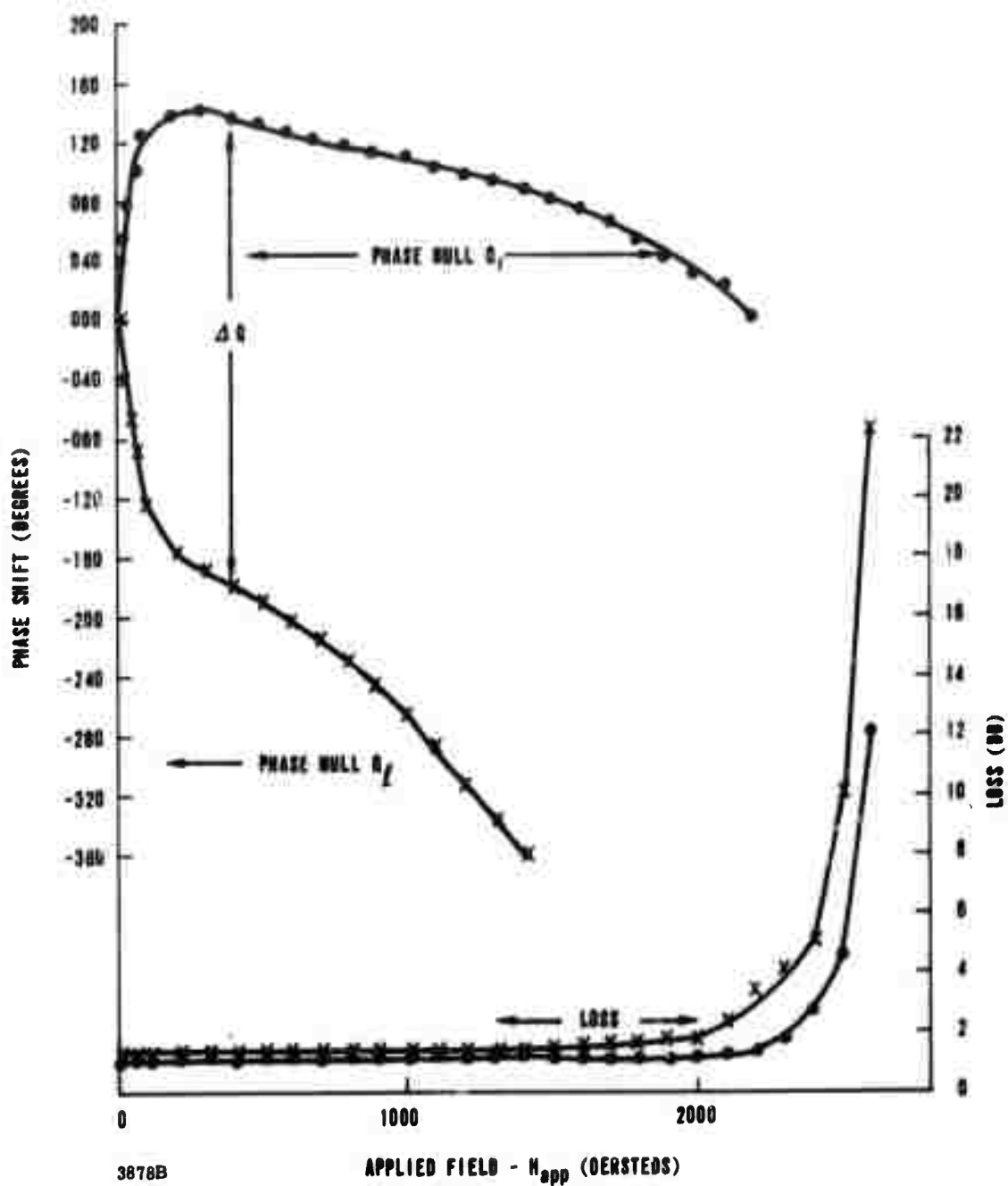


Figure 66. Loss and Phase Shift Versus Applied Field in the Dielectric-Loaded Ferrite Slab Configuration shown in Figure 65.

shift is seen over the range of dc magnetic field values shown. The loss shown here includes the loss, not only of the phase shifter, but also that due to the unbalance of the bridge used for these measurements. Since the latter loss amounts to approximately 0.40 db, loss of the phase shifter itself is seen to be approximately 0.7 db from approximately 0 to 1400 oersteds of applied dc magnetic field. Thus, this configuration would yield approximately 1.20 db per 360° of phase shift at 50 oersted applied field.

Considerable insight into the adjustment of ferrite material parameters to control peak power effects in digital phase shifters has been provided by the initial results of the experimental and theoretical studies discussed above. This insight has served as the basis for the synthesis of operational high peak power phase shifters in various frequency bands. For example, operational S band phase shifters have been synthesized having peak power capabilities of the order of 80 to 100 kw.

Operational high power phase shifters often have stringent constraints on physical length and low power insertion loss as well as the high power capability requirement. A price must always be paid to obtain high peak power capability. If the desired peak power threshold is obtained by using a low normalized saturation magnetization, the device will of necessity be longer than if a higher saturation magnetization material could be used, because for a given remanence ratio differential phase shift is directly proportional to the saturation magnetization. If the saturation magnetization is too low, the insertion loss per 360° of differential phase shift will increase drastically due to dielectric and waveguide copper losses (see Figure 45). On the other hand, if the desired peak power capability is obtained by rare earth doping to increase ΔH_k , the insertion loss will increase in direct proportion to the increase in ΔH_k (see Figure 50). In most operational designs compromises will obviously be required with the saturation magnetization decreased and ΔH_k increased somewhat. In any case, the data and guide lines presented in this report should permit the selection of material parameters for optimum performance under a known set of constraints. It should also be recognized that for a given input power the rf magnetic field in the ferrite element is a function of the geometry of the structure, the degree of dielectric loading, etc. Therefore, the peak power capability of a phase shifter can also be increased by optimizing the geometry. For example, increasing the height of a TE mode rectangular waveguide phase shifter has little effect on the phase shift or loss but appreciably decreases the rf field intensity

in the ferrite and hence increases the high power capability (it will of course ultimately lead to multi-moding difficulties).

In summary, it is felt that the experimental and theoretical results presented here represent a rather complete understanding of high power effects in remanent state ferrites. These results, together with the results of the low power studies, provide a basis for the design of material and structure for optimum high peak power digital phase shifters.

001002

BLANK PAGE

5 PRINCIPAL CONCLUSIONS

- The correlation obtained between theoretical predictions and measured values of both high and low power characteristics of remanent state devices indicates that ferromagnetic materials in the remanent state can be accurately represented as an assembly of magnetically saturated regions (domains) whose size and shape depend, among other things, upon the shape of the material sample.
- Peak power handling capability of a remanent state phase shifter is directly proportional to the spin wave linewidth ΔH_k of the material and inversely proportional to its normalized saturation magnetization $\frac{\omega_m}{\omega}$.
- At a given frequency, ω , peak power capacity can be increased by decreasing $\omega_m = \gamma 4\pi M_s$, e.g., by aluminum doping of garnets.
- $$\Delta H_k = \Delta H_{k/k=0} + B k^2$$

When the relative position of the spin wave manifold and the microwave frequency for a given domain is such that low k half-frequency spin waves are available, $\Delta H_k \approx \Delta H_{k/k=0}$.
- Peak power capacity of a remanent state phase shifter can be increased by increasing $\Delta H_{k/k=0}$ for all domains, e.g., by rare earth doping of garnets.
- When the relative position of the spin wave manifold and the microwave frequency for a given domain is such that no low k half-frequency spin waves are available, the Bk^2 term and, consequently, the threshold field of that domain, increase dramatically. For materials with low $\Delta H_{k/k=0}$ (such as YIG+Al) the spin wave linewidth becomes $\Delta H_k \approx Bk^2$. The principal control on the relative position of the different spin wave manifolds for the various domains of remanent state material is by variation of $\frac{\omega_m}{\omega}$ through its influence on the effective bias field of each domain. The multidomain model for these materials permits the calculation of the $\frac{\omega_m}{\omega}$ at which the abrupt increase in ΔH_k , caused by the nonavailability of low k spin waves, occurs. For domains having the lowest possible threshold field (i.e., Polder - Smit domains), the transition value of $\frac{\omega_m}{\omega}$ is found to be about 0.3.

In a given sample there may not be any domains of this type and as a result the abrupt increase in power handling capacity would occur at a larger value of $\frac{\omega_m}{\omega}$.

- Insertion loss at low peak power levels is directly proportional to the intrinsic linewidth of the material. Intrinsic linewidth at a given frequency is approximately equal to ΔH_k for that frequency. Thus, increasing peak power capacity by increasing ΔH_k necessarily means greater insertion loss at low peak power levels.
- Loss per 360° of differential phase shift increases rapidly for low ratios of $\frac{\omega_m}{\omega}$ due to dielectric and copper losses. Thus, adjusting $\frac{\omega_m}{\omega}$ to obtain high peak power capacity can lead to increased insertion loss, as well as requiring longer physical length to obtain 360° differential phase shift.
- The capability of the analytical procedure to separate and identify the source of the various loss components is of considerable utility in selecting optimum material and design to achieve a specified peak power handling capacity.
- High density materials appear to have the best overall properties for use in remanent state phase shifters.
- Remanence magnetization appears to vary with temperature in approximately the same manner as the saturation magnetization.
- Below resonance (in frequency) operation has been achieved in a helical line digital phase shifter. The shape of the resonance loss curve for the remanent state material is very much like the resonance curve of a saturated sample, only broader. A figure of merit of about 25 degrees/db has been achieved at 1 GHz. Operation at frequencies below resonance is of great interest for low frequency phase shifters because of the inherently high peak power capacity obtained.
- Table VII lists some possible tradeoffs in FDPS between peak power (P_p), average power (P_{avg}), loss per 360° and phase shift per inch. In each frequency band the first line of values is typical of a low peak, low average power configuration designed to have maximum phase shift per unit length and minimum loss per 360° . The second line of values represents a high peak, low average power configuration in which high peak power capability has been obtained by decreasing the ferrite magnetization. The loss per 360° increases and the phase shift per inch decreases because of the lower value of m_s . The third line of values represents a high peak,

004600

high average power phase shifter configuration. Rare earth doped (gadolinium) garnets would be used to achieve phase shift stability with average power variations and the loss per 360° would increase in proportion to the required doping.

Note that, in going from the low peak, low average power configuration to the high peak, high average power configuration by rare earth doping, the loss per 360° just about doubles while the phase shift per inch decreases by almost one-third. If it is desired only to increase the peak power capability, aluminum substitution only should be used since the increases in loss associated with this method of increasing the peak power capability are substantially less than with the rare earth doping.

In the above discussion the geometries of the ferrite and waveguide were fixed. By making certain adjustments in the ferrite geometry, both the peak and average power capability can be increased by approximately a factor of 10. The corresponding loss per 360° increases about 25 percent while the phase shift per inch decreases to about one-third its previous value. These sacrifices are acceptable in some applications.

TABLE VII. LOSS AND POWER TRADE-OFFS IN FERRITE PHASE SHIFTERS

Freq. Band	P _p (kw)	P _{avg} (watts)	m _s = $\gamma 4\pi M_s / F$	$\Delta H_k _{k=0}$ (Oe)	Loss / 360° ^① (db / 360°)	$\Delta \phi / \text{In.}$ ^② (Degrees / Inch)	Typical Material
X	1	5	0.63	5	0.40	150	Mg Mn Ferrite or YIG
X	50	5	0.25	5	0.70	67	Mg Mn Al Ferrite or Al substi- tuted YIG
X	50	50 ^(A)	0.35	50	0.75	92	Gd, Al substituted YIG
C	1	5	0.90	5	0.40	160	Mg Mn Ferrite or YIG
C	100	5	0.26	5	0.65	40	Mg Mn Al Ferrite or Al substi- tuted YIG
C	100	100 ^(A)	0.35	50	0.80	55	Gd, Al substituted YIG
S	1	20	0.60	5	0.40	57	Mg Mn Al Ferrite or YIG
S	500	20	0.26	5	0.70	23	Al substi- tuted YIG
S	500	400 ^(B)	0.30	50	0.95	28	Gd, Al substituted YIG

① LP 360° values shown are for operational devices at indicated power levels.

② $\Delta \phi / \text{inch}$ values shown are for low power, room temperature operational values slightly lower.

(A) Fin Cooling Required: forced air or water desirable (reduced height waveguide).

(B) Water cooling and boron nitride thermal conducting slabs required; reduced height waveguide desirable.

6 PROGRAM FOR NEXT INTERVAL

The experimental and theoretical investigations will continue along the present lines. In L band gadolinium-aluminum substituted YIG materials will be tested at low power levels to determine the operating characteristics and limitations to be expected at low frequencies. Both above and below resonance performance will be determined.

The X band and C band testing will continue at low and high power levels in order to further check the validity of the theoretical model, and to extend the materials evaluations. Section 4.3 and Tables I and II list the materials selected for these studies and include 14 aluminum and rare earth substituted YIG materials and 13 spinel ferrites.

004002

APPENDIX A

APPENDIX A

The following derivation of the mathematical expression for the rf magnetic field intensity applies strictly to a dielectric-slab loaded rectangular waveguide propagating the TE_{10} mode. Figure A1 shows a cross-sectional view of the configuration.

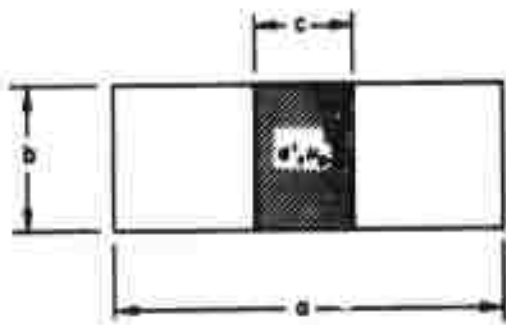
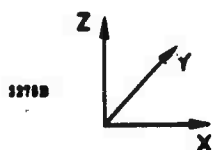


Figure A1. Cross-Sectional View of the Dielectrically-Loaded Rectangular Waveguide



Equation (18) of Vartanian et al^{*} is solved to read:

$$E_0^2 = \frac{4 Z_w (1 + r)}{a b R} P_T \quad (1)$$

where $Z_w = \eta \frac{k}{\beta}$ = the wave impedance

$$\eta = 377 \text{ ohms}$$

$$k = 2\pi/\lambda_0$$

$$\beta = 2\pi/\lambda_g$$

$$r = \frac{C/a}{1 - C/a}$$

$$R = r \left(1 + \frac{\sin 2q}{2q} \right) + \left(\frac{\cos q}{\sin p} \right)^2 \left(1 - \frac{\sin 2p}{2p} \right)$$

$$q = C/2a (\epsilon' k_a^2 - \beta_a^2)^{1/2}$$

$$p = 1/2 (1 - C/a) (k_a^2 - \beta_a^2)^{1/2}$$

P_T = the threshold power level

E_0 = the maximum electric field intensity which occurs at the center of the guide

*P. H. Vartanian et al, Propagation in Dielectric Slab Loaded Rectangular Waveguide, "IRE Trans. of the PGMTT, April 1958.

The transverse component of rf magnetic field intensity is

$$h_x = \frac{-\beta}{\omega \mu_0} E_z \quad (2)$$

where, at the center of the waveguide, $E_z = E_0$. Combining these two equations gives

$$h_{ox} = \frac{\beta}{\omega \mu_0} \left(\frac{4\eta ka/\beta a (-+r) P_T}{a b R} \right)^{1/2}$$

and since $\omega \mu_0 = \eta k$ $\left(\eta = \sqrt{\frac{\mu_0}{\epsilon_0}} \text{ and } k = \omega \sqrt{\mu_0 \epsilon_0} \right),$

then
$$h_{ox} = \left(\frac{4\beta a (1+r) P_T}{\eta k a R a b} \right)^{1/2}$$

or
$$h_{ox} \left(\frac{ab}{P_T} \right)^{1/2} = \left(\frac{.0106\beta a (1+r)}{R k a} \right)^{1/2} \text{ in MKS units}$$

or
$$h_{ox} \left(\frac{ab}{P_T} \right)^{1/2} = \left(\frac{806\beta a (1+r)}{R k a} \right)^{1/2} \quad (3)$$

where h_{ox} is in oersteds, P_T in kilowatts and a, b in inches.

Figure A2 shows how $h_{ox} \left(\frac{ab}{P_T} \right)^{1/2}$ varies with frequency ka and dielectric slab width C/a .

The transverse component of rf magnetic field is maximum at the center of the waveguide ($X = a/2$) and decreases sinusoidally to the outer dielectric wall. Thus

$$h'_x = h_{ox} \cos (\epsilon' k^2 a^2 - \beta^2 a^2)^{1/2} X/a$$

and at the outer dielectric wall ($X = C/2$)

$$h_x = h_{ox} \cos (\epsilon' k^2 a^2 - \beta^2 a^2)^{1/2} C/2a \quad (4)$$

In most digital phase shifter structures the outer toroid wall is a region in which $h_y \approx j h_x$; that is, the rf magnetic field is circularly polarized there and has the magnitude h_x .

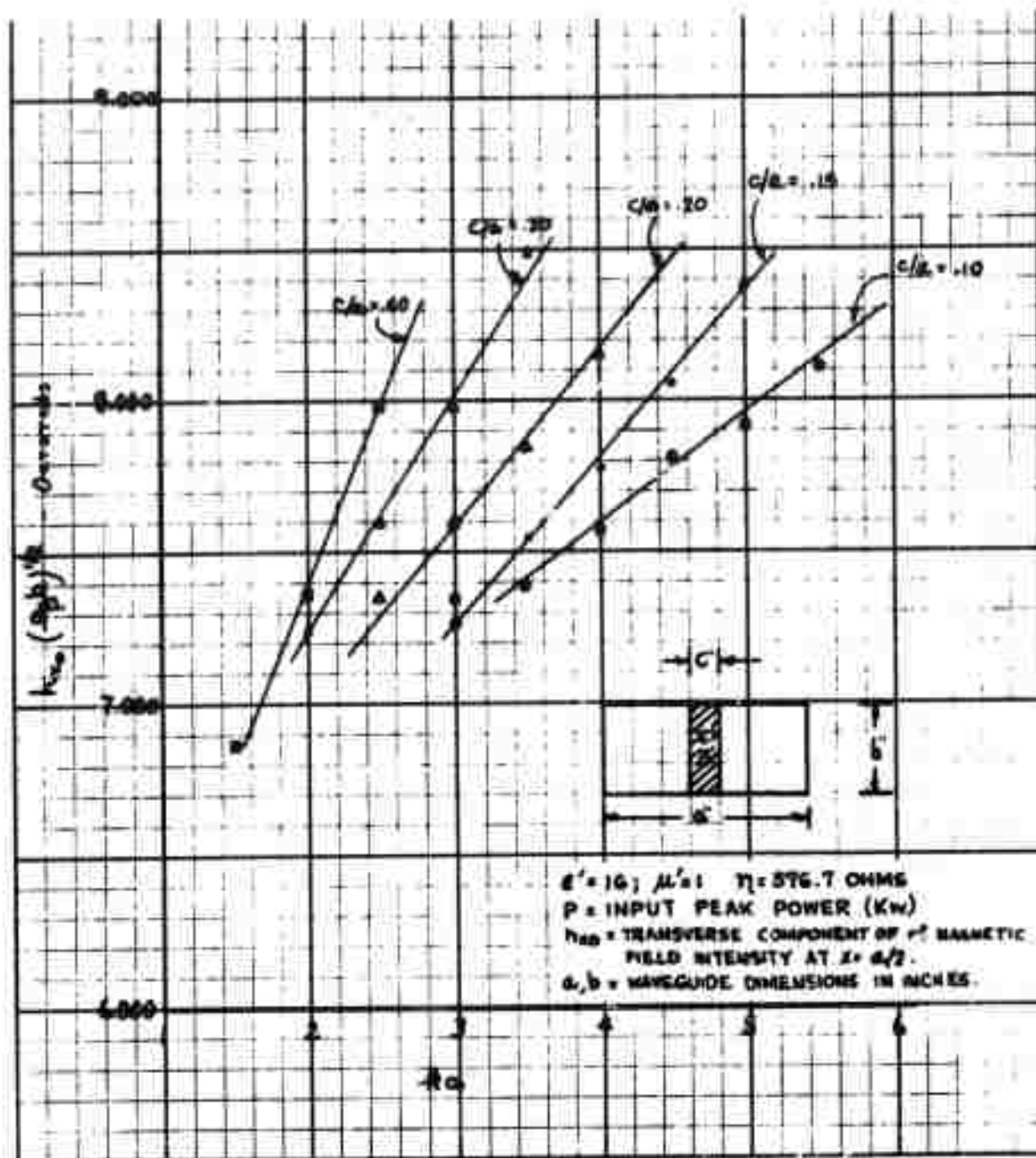


Figure A2. Transverse Component of rf Magnetic Field at $x = a/2$ Frequency and Slab Width for the TE_{10} mode in Rectangular Waveguide

DISTRIBUTION LIST

Six (6) copies

Director
ARPA
The Pentagon
Washington, D. C. 20301

One (1) copy

RTD (RTTTG)
Bolling AFB, D. C. 20332

Two (2) copies

Battelle Memorial Institute
ATTN: Security Officer
505 King Avenue
Columbus, Ohio 43201

Twenty (20) copies

DDC (TISIA-2)
Cameron Station
Alexandria, Virginia 22314

Four (4) copies

RADC (EMATE/Mr. P. A. Romanelli)
Griffiss AFB, New York 13440

Two (2) copies

Advisory Group on Electron Devices
ATTN: Mr. I. Press
346 Broadway
New York, New York 10013

One (1) copy

Westinghouse Electric Corporation
ATTN: Dr. L. R. Wicker
Electronic Division
P. O. Box 1897
Baltimore, Maryland 21203

One (1) copy

The Bendix Corporation
Bendix Radio Division
ATTN: Mr. G. Engelbert
Department No. 481
Towson, Maryland 21204

One (1) copy

Hughes Aircraft Company
ATTN: Mr. Robert A. Moore
Building 600
P. O. Box 3310
Fullerton, California 92634

004002

Distribution List (Continued)

One (1) copy Radio Corporation of America
ATTN: H. Collar
Missile and Surface Radar Division
Moorestown, New Jersey 08057

One (1) copy Advanced Technology Corporation
ATTN: Mr. M. Cohen
1830 York Road
Timonium, Maryland 21093

One (1) copy Raytheon Company
Research Division Library
ATTN: M. G. Bennett
28 Seyon Street
Waltham, Massachusetts 02154

One (1) copy Scientific Atlanta, Inc.
ATTN: Dr. J. E. Pippin
Box 13654
Atlanta, Georgia 30324

One (1) copy Director
U.S. Army Electronics Laboratories
ATTN: AMSEL-RD-PEM/Mr. Lipetz
Fort Monmouth, N. J. 07703

One (1) copy Chief, Bureau of Ships
Department of the Navy
ATTN: E. A. Mroz/68182
Washington, D. C. 20360

One (1) copy Lincoln Laboratories
ATTN: D. H. Temme, C271
Box 73
Lexington, Massachusetts 02173

One (1) copy AFML (MATE)
Wright-Patterson AFB, Ohio 45433

One (1) copy FRP-General Electric Company
ATTN: Mr. T. Connelly
Syracuse, New York 13201

004002